Ludwig-Maximilians-Universität München

Anisotropy of Magnetic Remanence Development of an Automated System and Application to Natural Sediments

Dissertation
zur Erlangung des Doktorgrades
der Fakultät für Geowissenschaften der
Ludwig-Maximilians-Universität München

vorgelegt von
Michael Richard Wack

am
28. 02. 2012

1. Gutachter: Prof. Dr. Stuart Gilder

2. Gutachter: Prof. Dr. Vincent Courtillot

Tag der mündlichen Prüfung: 13. 07. 2012

Contents

List of Figures

List of Tables

Acknowledgments

I would like to thank:

- My advisor Stuart Gilder for all the good ideas, hints, explanations and hands-on help. I'm also grateful for his patience and that he let me do things my own way.

- Deutsche Forschungsgemeinschaft (DFG) for funding this thesis with grant Gi 712/1-1 and 436 KIR 113/2/0-1.

- The Department of Earth and Environmental Sciences for providing workplace and the necessary computing and workshop infrastructure. Special thanks goes to the computer administrator Jens Oeser, the head of the workshop Markus Sieber and all mechanists and electricians who helped to get the SushiBar working.

- Eduard Sobel, Euan Macaulay, Vasyl Hyshchyn, Ivan Andreev, Alexander Mikolaichuk, Tobias Wurft and the Central-Asian Institute of Applied Geosciences (CAIAG) for their great help in the field.

- Martin Leberer and Denise Schmidt for laboratory measurements.

- My office colleague Josef Weber and all others who helped to build the magnetically shielded room.

- Michael Winklhofer, Ramon Egli and Nikolai Petersen for their ever-ready advice.

- My wife Kerstin and my son Moritz, who was born in July 2011.

- My former roommate and friend Christoph Moder for a lot of discussions in my office.

- All the other PHD students, nice colleagues and guests at our institute.

- Last but not least, all my friends and my parents.

Introduction and Summary

Paleomagnetism is the scientific discipline that helped reveal one of the most fundamental discoveries about our planet: the movement of the continents in the past. The striking quality of many rocks to preserve the ancient direction of the earth magnetic field allows us to reconstruct their paleolatitude and rotation from the recorded field. In combination with additional geological or biological data, paleomagnetism allows us uniquely reconstruct positions and rotations of tectonic plates through time.

Globally recorded polarity changes demonstrate that the magnetic field of the earth inverted its polarity frequently at irregular intervals on geological time scales. Vice versa characteristic patterns of such changes in continuously deposited rocks can be used to date such formations which is known as magnetostratigraphy. Scarcer studied properties like directional dependence (anisotropy) or temporal acquisition respectively decay (viscosity) of magnetizations can either obscure the methods mentioned above or be used to improve our understanding about the recording process. Anisotropy of magnetic properties, also called magnetic fabric, can reflect sedimentary and tectonic regimes as well as paleocurrent and paleowind directions and is likely connected to the widely observed flattened inclinations in sediments.

For most branches of modern sciences like astronomy, particle physics, geodynamics or seismology, the introduction and increasing performance of computer systems brought big advantages in the number and precision of acquisition and processing of measured or modeled data. Unfortunately the field of paleomagnetism did not benefit much from this development since most calculations are comparatively simple and the main task remains the selection, collection, orientation and preparation of rock samples as well as their analysis in the lab. Most preparatory steps were

optimized during the last decades and involve some inevitable workload. However as far as lab procedures are concerned, improvements in both the operational software as well as the automation of complex measurements facilitates the processing of larger sample sets which is especially important in geosciences due to the natural scatter of properties within one geological unit.

The intention of this work is to explore special magnetic properties of rock specimens in a systematic way on large numbers of samples. In most rock magnetic studies, such properties are neglected due to the high experimental effort. Particularly the anisotropy of magnetic remanence acquisition is of interest, since it represents the rock magnetic fabric of the grains which carry the paleomagnetic signal.

Because innovative instrumentation was needed to obtain such measurements with the necessary precision and quantity, the first part of this document covers the specifically developed hard- and software (chapters 1-3) whereas the second part focuses on case studies on sedimentary sediments from Central Asia (chapters 4 and 5). The sensitivity to uncontrolled ambient magnetic fields is inherent to experiments based on the measurement of weak magnetic fields and artificial acquisition of magnetic remanence. Therefore a low residual magnetic field is crucial. A shielded room which achieves the necessary high shielding factor to reduce the ambient field to about 1% of the earth magnetic field needs a careful design of its geometry as well as the selection of the right materials. Chapter 1 discusses the construction of a large 90 m^3 passively magnetically shielded room with a residual field of about 500 nT.

Subsequently a versatile and general purpose computer program for measurements of magnetic moments with spinner as well as cryogenic (SQUID) magnetometers called 'CryoMag' is described in chapter 2. On its own it provides a reliable basis for customizable manual measurements for any interested lab. Graphical representation of measured data and a comprehensive storage of raw values enables easy judgment of data quality and further analysis. For this work 'CryoMag' is relevant since it provides the foundation for the operation of the automatic measurement system introduced below.

To study the magnetic fabric of rocks, anisotropy of magnetic susceptibility (AMS) is widely used due to the simplicity of measurement compared to remanence based methods. Since AMS integrates over all grains, including ferro-, dia- and paramagnetic ones, it does not necessarily isolate the fabric of remanence carrying grains, which is crucial to understand remanence acquisition. Further AMS must be used with care since it is dependent on the domain state (i.e. maximum susceptibility is along the easy axis of magnetization for multi-domain particles with shape anisotropy whereas uniaxial single-domain particles show maximum susceptibility perpendicular to their easy axis). This leads to ambiguous results which are hard to interpret (*Potter and Stephenson*, 1988). Using a remanence based method as described below eliminates that problem.

In nature igneous rocks commonly acquire a thermal remanent magnetization (TRM) when cooling through their Curie temperature, whereas sedimentary rocks acquire a detrital remanent magnetization (DRM) by alignment of the individually deposited grains within the earth magnetic field. Chemical remanent magnetizations (CRM) are observed when magnetic minerals grow above a critical size (i.e. transition from superparamagnetic to single domain state).

The measurement of anisotropy of magnetic remanence requires to impart a remanence in different, well distributed directions and subsequently the measurement of the resulting magnetic moment. To produce an artificial remanence in the lab, a fast, reproducible and non altering method must be used. Common laboratory methods include heating and cooling a sample inside a magnetic field, which results in a TRM but often alternates the magnetic grains which make it unsuitable for successive measurements. Another procedure exposes a sample to a strong magnetic DC field which results in a so called isothermal remanent magnetization (IRM), which is commonly not linearly dependent on the applied field and therefore not the best choice for anisotropy measurements. Creating artificial DRMs and CRMs is possible but dependent on many factors, laborious and time consuming. Finally exposing a sample to a decaying alternating magnetic field with a small direct bias results in an anhysteretic remanent magnetization (ARM) (figure 0.1). Typical values for the involved magnetic fields are 100 mT peak for the AC field and 0.1 mT for the DC bias field. It was shown by comparison of AF demagnetization
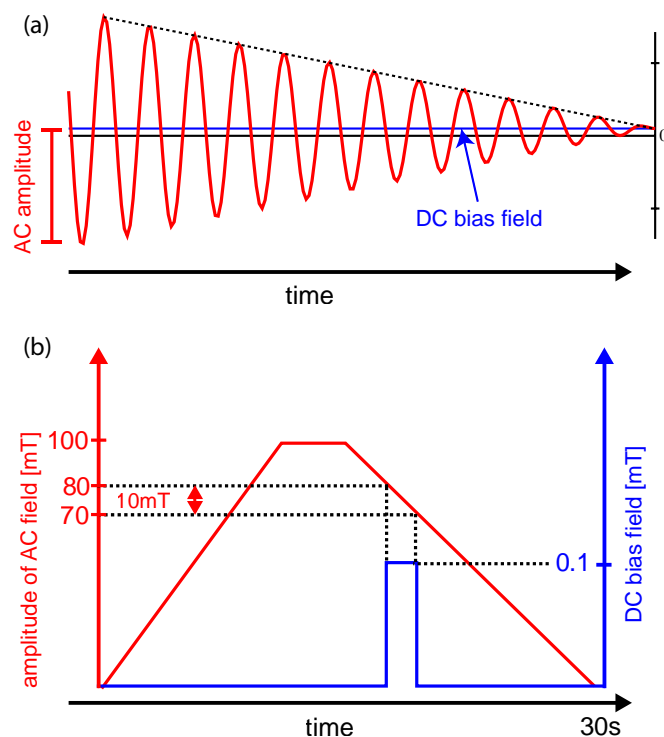
Figure 0.1.: (partial) ARM acquisition. (a) AC magnetic field linearly decaying with time to zero. Biased by smaller DC field. (b) full cycle for partial ARM acquisition. Numerical values are exemplary. AC field amplitude is ramped up to 100 mT, hold for a few seconds and ramped down to zero. When the AC amplitude decayed to 80 mT the DC bias field with a strength of 0.1 mT is turned on until the AC field amplitude undercuts 70 mT. This results in a magnetization of the grain fraction affected by fields between 70 and 80 mT. All other grain fractions affected by fields up to the maximum field amplitude are demagnetized.

curves that ARM affects a similar grain fraction as the natural detrital remanent magnetization (DRM) of sediments (*Levi and Merrill*, 1976). Although ARM does not occur in nature, it is the best lab based analogon to a DRM. For small values of the bias field (<1 mT) ARM acquisition is commonly proportional to it. Therefore it is well suited to study the anisotropy of sediments. Further the use of partial ARMs (figure 0.1) allows to selectively focus on certain coercivity ranges which were shown to correlate well with different grain sizes (*Jackson*, 1991).

The resulting anisotropy is found by applying a least squares approach to determine a symmetric, second order tensor that fits the measured directional magnetizations best. Three eigenvectors and eigenvalues are determined by diagonalizing the tensor. The directions of the eigenvectors define the orientations and the eigenvalues the length of the principal axes of the anisotropy ellipsoid. Ratios of the eigenvalues
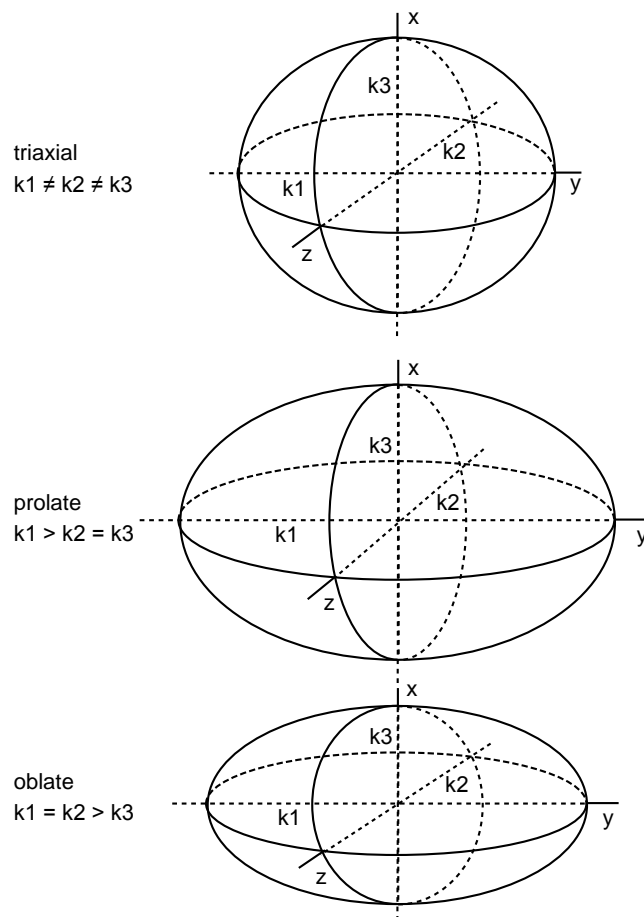
Figure 0.2.: Different shapes of anisotropy ellipsoids. Lengths of principal axes represent eigenvalues deduced from anisotropy tensors. k1 is maximum, k2 intermediate and k3 minimum axis.

are used to quantify the degree of anisotropy and the shape (*Jelinek*, 1981). Characteristic shapes can be spherical, triaxial, prolate or oblate (figure 0.2). Magnetic fabrics are sensitive to very small amounts of strain. Pure depositional-compactional fabrics are expected to be oblate with a vertical minimum axes. With increasing compressional strain the minimum axis gets orientated parallel to the compressional axis. Depending on the degree of deformation the shape can be prolate or oblate (*Winkler et al.*, 1997).

The systematic determination of the anisotropy of ARM, which requires remanence acquisition and subsequent measurement of the resulting magnetic moment in

12 different and precisely defined directions, on hundreds of specimens required the development of an automated system. This instrument called 'SushiBar' is based on a commercially available SQUID magnetometer and a custom made ARM coil system and handles 99 specimens without user interaction. Additionally it automates the measurement of magnetic viscosities, partial ARM spectra as well as standard paleomagnetic demagnetization curves. Chapter 3 describes the setup, calibration and test measurements of the 'SushiBar'.

Finally chapter 4 and 5 demonstrate the application of the 'SushiBar' in two case studies of Cenozoic fluvio-lacustrine sedimentary samples from Central Asia. This region is shaped by the intercontinental India-Asia collision and enables the study of recent and strong tectonic deformations, mountain building and associated sedimentation processes. The Xishuigou magnetostratigraphic section located near Subei (Gansu Province, western China) cuts through 2 km thick sediments, deposited ≈26 to ≈19 Ma ago. Due to a previous study, lots of properties and gradual changes of various parameters throughout the section are well known and can be used to interpret and verify the results obtained by the 'SushiBar'. That study focuses on anisotropy of ARM in different coercivity windows and its relation to AMS, viscosity of ARMs depending on the chosen coercivity window and ARM spectra as a grain size distribution indicator.

The second study area is located further west in the south of the Issyk-Kul basin in Kyrgyzstan. Two parallel magnetostratigraphic sections and six separated sites in the sediments deposited on the northern flank of the Tianshan provide insight into the evolution and sedimentation of a young and still active orogen. The Tianshan is a 2500 km long, east-west striking and up to 7000 m high mountain chain which was reactivated in the Cenozoic by the India-Asia collision. Magnetization carrying minerals are identified by rock magnetic measurements. Stepwise demagnetization of the natural remanent magnetization isolates characteristic paleomagnetic directions. Correlations between the two sections is possible by analyzing the polarity patterns. The anisotropy of ARM is used to study the tectonic fabric of the area.

The appendix includes examples of relevant file formats and listings of program code for the calculation of anisotropy parameters from directional measurements.

1. Construction of a Magnetically Shielded Room

1.1. Magnetic Shielding

Magnetic (and electric) shielding is nowadays widely used in industry to avoid interference of sensitive electronic devices (*Rikitake*, 1987; *Koroglu et al.*, 2009; *Keshtkar et al.*, 2011). In this scenario it is commonly sufficient to reduce electrical fields and temporal gradients of magnetic fields to moderate levels, so that parasitic voltages and currents in the vulnerable electric circuits are negligible. Static fields like the earth magnetic field are not considered at all. The requirements for rock and paleomagnetic experiments are much higher because the magnetic field itself is the property of interest. SQUID (superconducting quantum interference device) magnetometers, commonly used to study sedimentary rock specimens, measure fields eight magnitudes below the magnetic field of the earth. Furthermore the rock specimens itself are sensitive to magnetic fields and can acquire spurious induced or remanent magnetizations. Therefore it is crucial to suppress ambient magnetic fields not only within the measurement volume.

Magnetic shielding can be done actively and passively. Helmholtz coil systems are used to actively compensate any external field. By adjusting the currents through three orthogonal coil systems, a magnetic field opposing the external field can be generated. If a fast enough feedback system based on a magnetic field sensor is used, also temporal variations of the field can be balanced (e.g., *Hilgenfeld et al.*, 2003). Due to the inhomogeneity of the generated magnetic field, a reasonable compensation is limited to a small volume compared to the

size of the coil system (*Collinson*, 1983). Passive shielding of larger volumes is possible by the use of material with a high magnetic permeability which serves as a low resistive path for the surrounding magnetic field or by material with a remanent magnetization causing a magnetic field that counteracts the external field. A very common material is electrical steel (also called transformer steel) (3% Si, 97% Fe), which is normally used as the core of transformers to optimize the magnetic coupling. Its remanent magnetization can contribute significantly to the shielding effect. Therefore special care has to be taken to align its remanence properly. To obtain a remanent magnetization that counteracts the external field, all sheets have to be magnetized along the ambient field direction. This results in a magnetic field outside the sheet opposite in direction to the magnetization (*Scott and Frohlich*, 1985). Mu-metal (80% Ni, 14% Fe, 5% Mo, 1% other) is especially produced for magnetic shielding purposes and features higher permeability and lower remanent magnetization than transformer steel. Therefore it provides better shielding against time varying fields and does not depend on the alignment of its remanent magnetization. The high permeability especially of mu-metal depends on the crystalline structure of the material. Therefore it is heat treated after manufacturing. Any stress from cutting or drilling which can alter the internal structure should be reduced to a minimum, which complicates the mechanical setup of a shielding. Other designs based on magnetic repulsion (*Sasada and Nakashima*, 2008) and magnetic shaking of the shielding material to increase its permeability (*Sasada et al.*, 1990; *Okazaki and Ueno*, 1992; *Sasada et al.*, 1996, 2000) were proposed but are not easy to adopt for a large scale room as described below and were therefore not considered.

To optimize the design of our room, I performed finite element simulations of field distributions with the FEMM program written by D. C. Meeker (http://www.femm.info). One limitation of the program is, that the definition of geometry and calculations are restricted to a two dimensional plane and assumed to continue unlimitedly in the third dimension. For our problem this does not pose a strong restriction since the metal sheets, commonly used for magnetic shielding are much longer ($\approx$2 m) than thick ($\approx$1 mm); although it is not possible to simulate the effect of any three-dimensional structure like corners. Figure 1.1
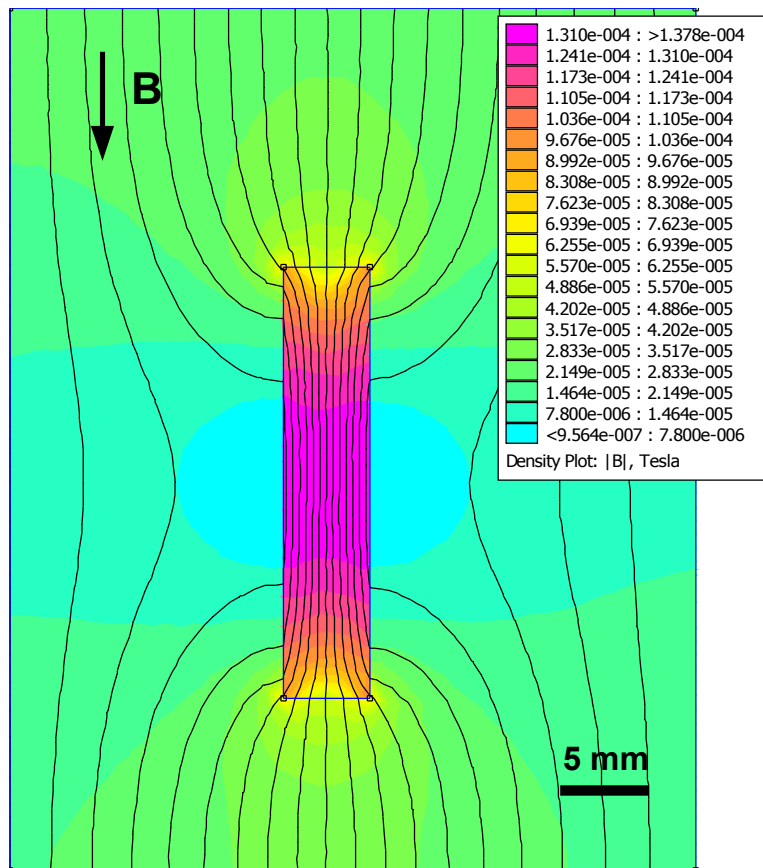
Figure 1.1.: Finite element simulation demonstrating the principal effect of mu-metal shielding. Field lines are focused inside the piece of mu-metal. Note the high magnetic field strength inside the mu-metal and the reduced field besides.

shows such a numerical simulation of a piece of mu-metal within a homogeneous earth like magnetic field. The magnetic field lines are focused inside the material which results in a reduced field intensity (i.e. shielding) on both sides. Efficient magnetic shielding can be obtained by enclosing a volume with a layer of high permeable material. Numerical simulations show a reduction of an earth like field by approximately 90% (shielding factor of 10) with a single 1 mm thick sheet of mu-metal enclosing a volume with a cross section of $5 \times 3 \text{ m}^2$ (figure 1.2). Generally multiple thin layers of material provide better shielding than a single thick layer (*Collinson*, 1983; *Scott and Frohlich*, 1985).
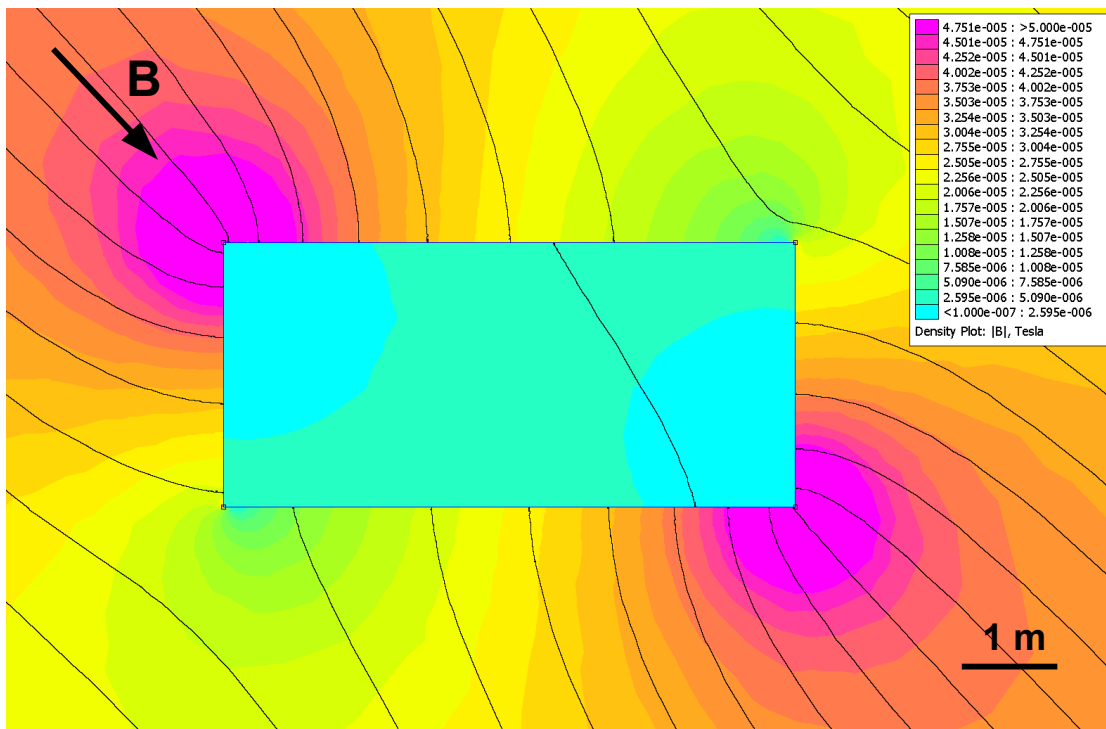
Figure 1.2.: Finite element simulation of a 6 m wide and 3 m high volume, magnetically shielded with a layer of 1 mm thick mu-metal in an earth like field. Vertical cross section.

Since a real room cannot be built out of one piece of metal and needs access openings, we paid special attention to joints between individual metal sheets and the alignment of the openings. The leakage of magnetic fields inside the shielded volume can be greatly reduced by covering joints with a strip of the same material (numerical simulation shown in figure 1.3). To avoid high magnetic fields at the openings, those should be preferentially aligned with the external field direction (i.e. east and west wall) (*Scott and Frohlich*, 1985).

1.2. Design of a 90 m³ Shielded Room

The layout of our shielded room had to follow space and material constraints. The available room (C027, Theresienstr. 41, Munich) is $13.2 \times 7.1 \times 3.35$ m³ in size but traversed by two pillars. To avoid the leakage of magnetic fields along
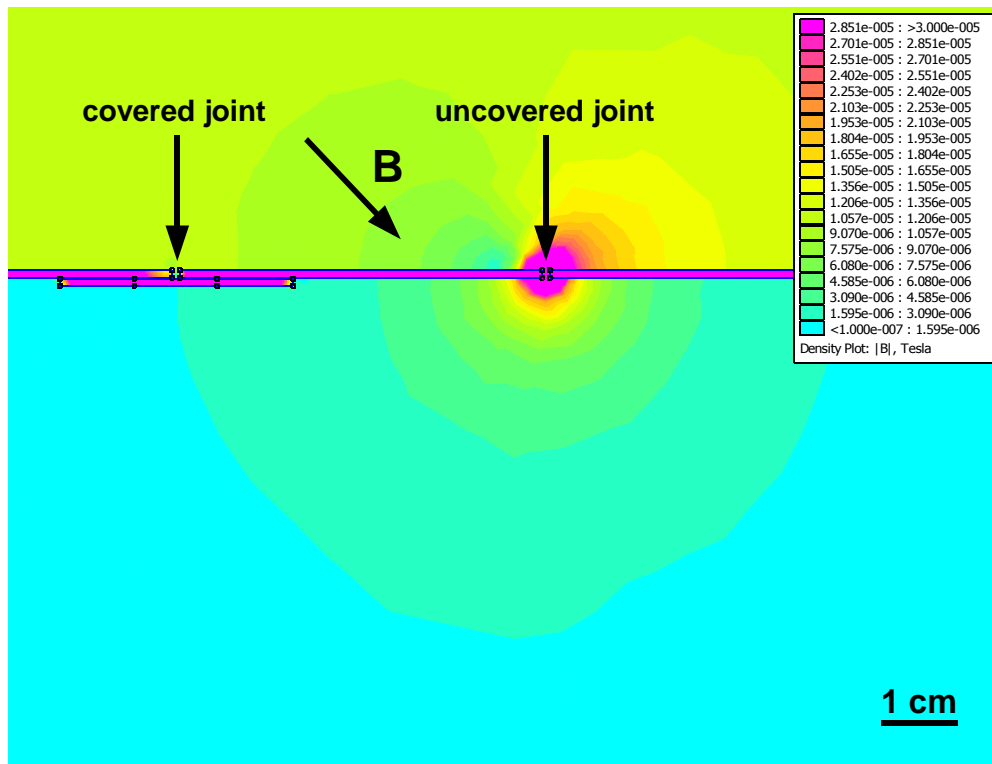
Figure 1.3.: Numerical simulation of covered (left) and uncovered (middle) joints. 1 mm gap within a 1 mm thick layer of mu-metal exposed to an earth like field. The left joint is covered with a 3 cm width strip of mu-metal in a distance of 1/10 mm to the shielding layer.

the pillars respectively the elaborate shielding of those, we built an extra inner room based on a wooden beam structure between the pillars with a sufficient size of $6 \times 5 \times 3.25$ m^3. This allowed us to design the shielding in a series of three shells (figure 1.4). For the outermost shell of (shield 1) we used available sheets of 0.65 mm thick transformer steel which are directly fixed on the wall, floor and ceiling of the original room. The floor and ceiling have two overlapping layers. The walls are made out of a single layer with strips that cover the joints of the sheets. Shield 2 forms the outside of the inner room. It consists of two overlapping layers of 0.65 mm thick transformer steel. We magnetized each sheet of transformer steel in the direction of the ambient field that it will eventually lay. For that purpose we constructed a portable system where a sheet is fixed, and then a coil with a 80 mT peak alternating field is passed twice (once each direction) around the entire sheet.
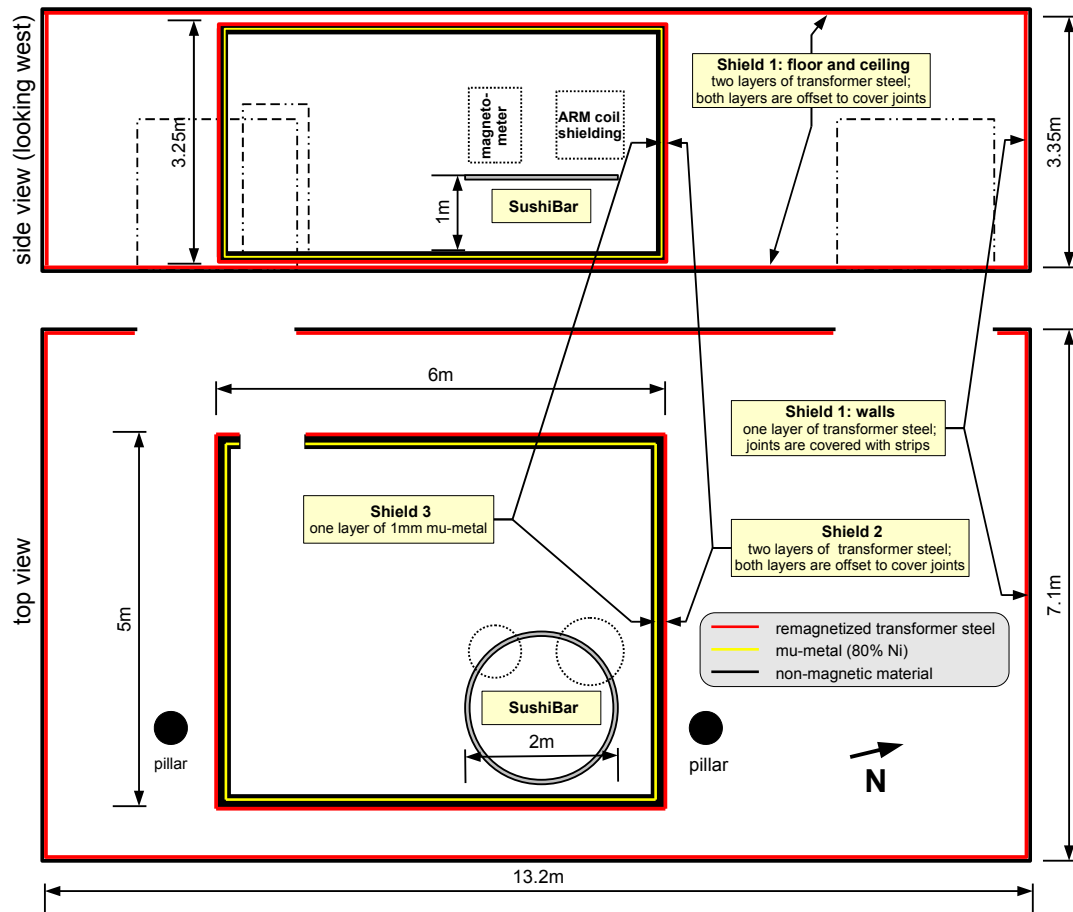
Figure 1.4.: Layout of the magnetically shielded room. Dimensions and arrangement of different shielding layers as well as location and dimension of the automated measurement system 'SushiBar' are shown. Pillars are made of concrete and part of the structure of the building.

Figure 1.5.: Final stage of construction of the inner shielded room. View towards the N-E corner. Mu-metal is in place but not yet covered with plasterboard.

This system can be oriented vertically and horizontally which allows to place a sheet in the position that it will be finally mounted to the wall, floor or ceiling. The innermost shield 3 is built out of a single layer of 1 mm thick mu-metal sheets and covered by plasterboards that form the inside walls of the inner room and protect the mu-metal mechanically (figure 1.5).

To control the effectiveness of the individual shields, we measured the magnetic field throughout the volume in a 1×1 m^2 grid at levels 0.3, 1.0, 2.0 and 2.7 m above the floor in the beginning and after each construction step with a vectorial fluxgate magnetometer. Each data point is averaged over several readings, which were taken every second. Detailed maps of the field intensity and directions in horizontal sections are shown in figures 1.6-1.8. Figure 1.6 shows the original state of the field with a strength of about 40000 nT which is fortunately 20% below the expected earth magnetic field which is probably caused by the construction steel of the building. Adding shield 1 reduced the field intensity by almost half but added a strong gradient in N-S direction (horizontal axis) close to the floor (figure 1.7). This can be either explained by changes in remanent magnetization or as an effect of induced magnetization as seen for mu-metal and described below.

Setting up the inner room reduced the field strength in the center to values around 500 nT (figure 1.8). Increasing field values towards the upper northern and southern lower edge are expected from numerical simulations (figure 1.2). As predicted by the simple numerical model in figure 1.1, also the field strength in the outer room decreased significantly (figure 1.8). Influences of the openings (entrance and opposing cable duct) of the inner room aligned close to the N-S direction are minor. Therefore we waived the installation of a shielded door, since opening and closing it could cause disturbing changes of the magnetic field inside the shielded volume. In total we reduced the static external field to about one percent of its strength which corresponds to a shielding factor of approximately $40000/500 = 80$ and fulfills the requirements of our experiments. Exemplary measurement of time varying fields (sampled every second for about 15 minutes) shows a decrease of the standard deviation of the total field from $\approx$190 nT for the unshielded room to $\approx$80 nT between shield 1 and 2, and to $\approx$50 nT inside shield 3 (data not shown).
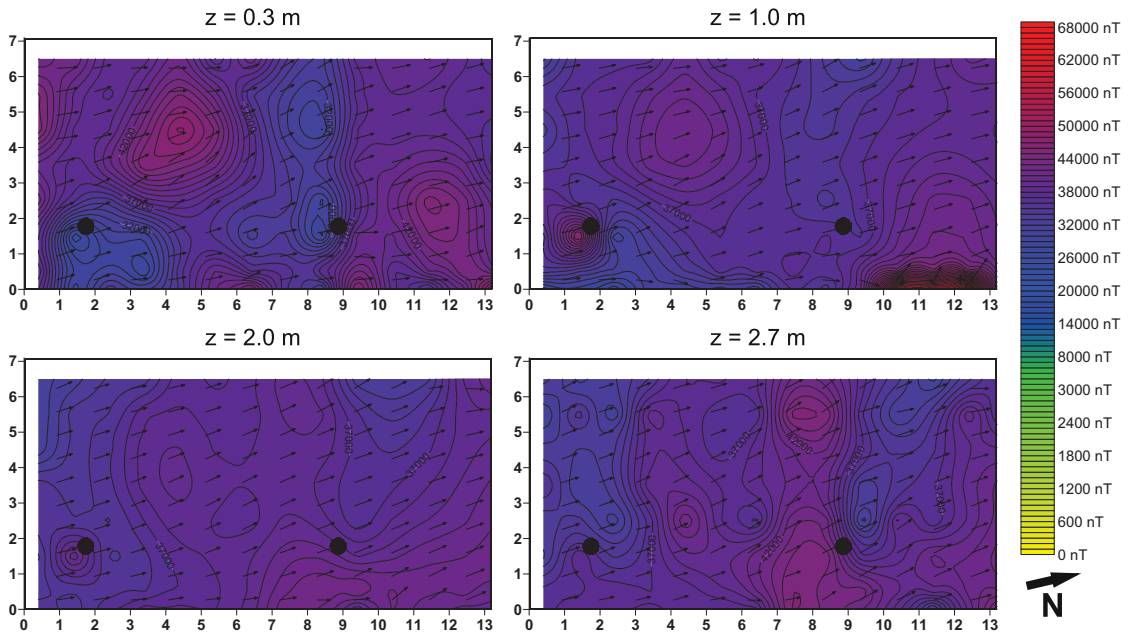
Figure 1.6.: Magnetic field maps at different horizontal sections as labeled without any shielding. Scales are in meters.
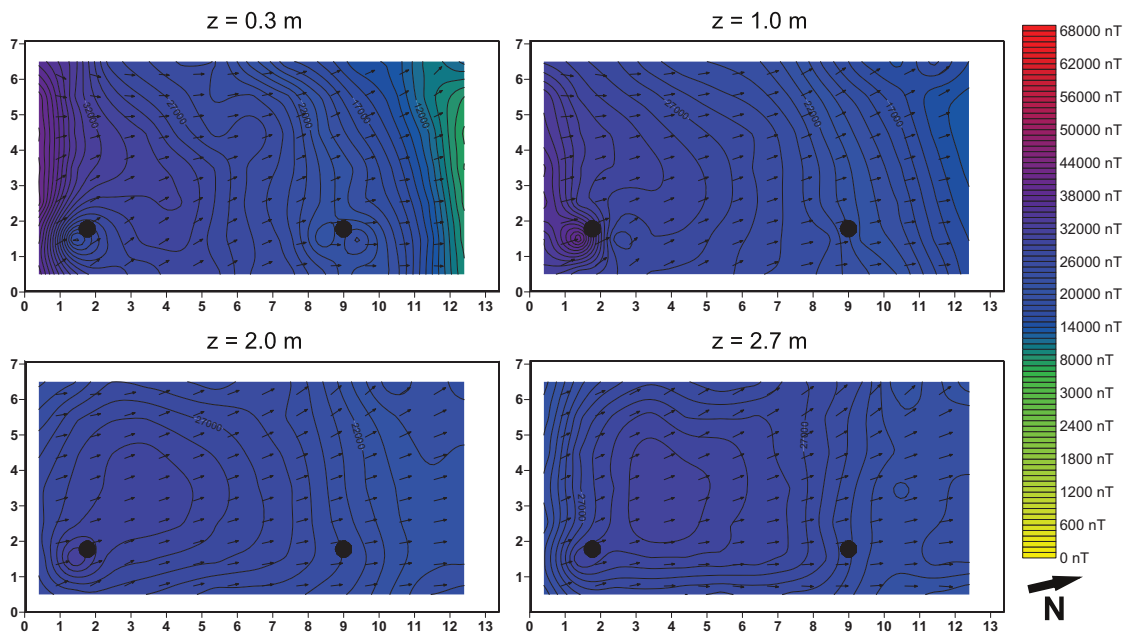
Figure 1.7.: Magnetic field maps at different horizontal sections as labeled with shield 1 in place but before constructing the inner room. Scales are in meters.
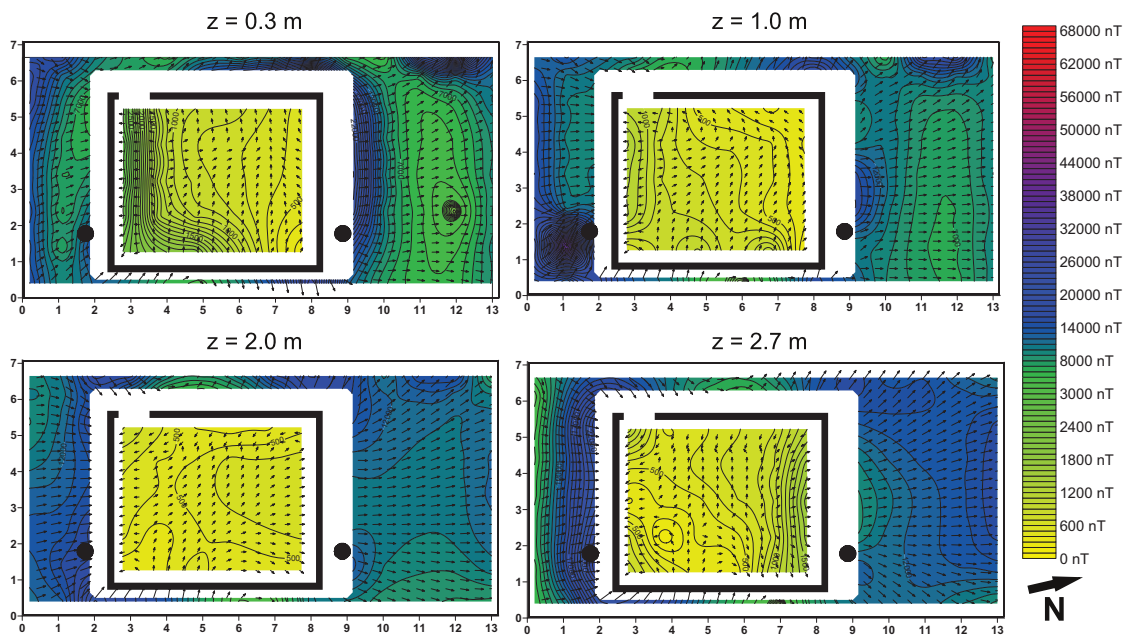
Figure 1.8.: Magnetic field maps at different horizontal sections as labeled with all shielding layers in place. Scales are in meters.

2. The CryoMag Program[1]

A new software package, called *CryoMag*, facilitates the measurement of magnetic moments using both 3-component (i.e. Superconducting QUantum Interference Device) and 2-component (i.e. spinner) magnetometers. The measurement process is optimized for, but not limited to, stepwise demagnetization experiments commonly used in paleomagnetism. A graphical representation of the data is always visible to the user in the form of orthogonal, stereonet and decay diagrams, which can be represented in in-situ, geographic or tilt corrected coordinates and can be saved as graphics files. Instrument specific settings, as well as arbitrary measurement positions, can be easily customized in a single configuration file. A comprehensive record of detailed measurement and statistical data is stored in XML (eXtensible Markup Language) based data files (*.cmag.xml). The final results of the measurements can be exported to several common file formats for further processing. The software is written in *Python*, an open source, cross-platform programming language and can therefore be used on popular operating systems like Windows, Linux and MacOS X. The complete source code is available on request from the author. The CryoMag open-source allows anyone to adapt the software to their specific equipment, file format and experimental requirements.

2.1. Introduction

Consecutive measurement of magnetic moments of oriented rock specimens is the fundamental method of typical paleomagnetic studies (e.g., *Butler*, 1992; *McElhinny*

---

and McFadden, 2000). Such data allow one to study the paleo-movement of the continents, the long-term behavior of the geomagnetic field, magnetostratigraphy, paleointensity, paleocurrent, etc.

Due to the large amount of data, it is crucial to carry out the measurements as efficiently as possible. Besides having adequate instrumentation, the operating software can have considerable bearing on the quality of the measurements. Although no software program can improve the fundamental measurements, it can aid the operator to choose the next (de)magnetization step and to recognize potential inconsistencies by providing statistical parameters and visualization of the data during the measurement process. The possibility to review raw data quickly and efficiently allows one to recognize potential error sources and to correct for them, and assists the interpretation process.

At present, there are two ways paleomagnetists operate their magnetometers: either they obtain a software package from the company that sold the magnetometer, or they write the software themselves. Commercial software is mostly limited to the Windows operating system and to a single, specific instrument. No customization can occur, as source codes remain proprietary. Molspin Ltd[2] and AGICO Inc.[3] offer software packages free of charge (spin4d and REMA5/REMA6, respectively) to operate their contemporary spinner magnetometers. 2G Enterprises[4] sells different software packages, starting at a price of $2500, to operate their SQUID magnetometers. For older versions of instruments (e.g., AGICO, JR-4 spinner magnetometer) no modern, adaptable software package exist, unless one obtains a copy from a generous colleague. There are free software packages specific to custom-built, automated setups for magnetometers (*Giddings et al.*, 1997; *Frederichs et al.*, 2000; *Kirschvink et al.*, 2008; *Morris et al.*, 2009) and u channel measurements (e.g., *Xuan and Channell*, 2009), but there is neither a ready-to-use downloadable package nor a publication that provides the source code for the several-hundred paleomagnetic laboratories worldwide. CryoMag was written to fill these voids.

---

[2]Molspin Ltd Website, http://www.molspin.com/
[3]AGICO Inc. Website, http://www.agico.com/
[4]2G Enterprises Website, http://www.2genterprises.com/

CryoMag is a new, user-friendly software package with a graphical interface, based on the cross-platform wxWidgets library (*Smart et al.*, 2010), to carry out remanent magnetization measurements on SQUID or spinner magnetometers. It provides an intuitive handling and presents all relevant data at a glance, thus allowing the user to focus on the measurement itself and not on the operation of the software. *CryoMag* is written in *Python* (*van Rossum and Drake*, 2009) an open source, cross-platform programming language. *CryoMag* runs on most computer systems, operates different types of magnetometers with a consistent user interface, and generates multiple file formats and data graphics, which eases everyday workflow and enables efficient use of existing hardware. Below is a description of *CryoMag* for SQUID systems.

2.2. Measurement Process and User Interface

After sample preparation, typical paleomagnetic demagnetization experiments begin with measuring the magnetization of the sample holder so that it can be subtracted from subsequent measurements of the specimens. Then the natural remanent magnetisation (NRM) is measured for all specimens. Subsequently the specimens are progressively demagnetized using alternating magnetic fields (AF) or thermal heating (TH), and after each treatment their magnetic moment is measured. The number and spacing of demagnetization levels is up to the operator. Specimens are measured several times in different orientations to improve the accuracy by averaging and to get an estimate of the scatter in terms of standard deviation of the total moment and the half angle of the 95% confidence cone (a95) of the magnetic vector direction.

The main functions of the program are organized in a panel that is displayed in the upper right half of the main window (figure 2.1 A). Different functions and the corresponding panels can be activated by the row of buttons located below the active panel (figure 2.1 B). The rest of the main window contains three diagrams (figure 2.1 C,D,E) which are discussed in section 2.2.5. In the following sections the various options and functions are described in the order of a typical workflow for
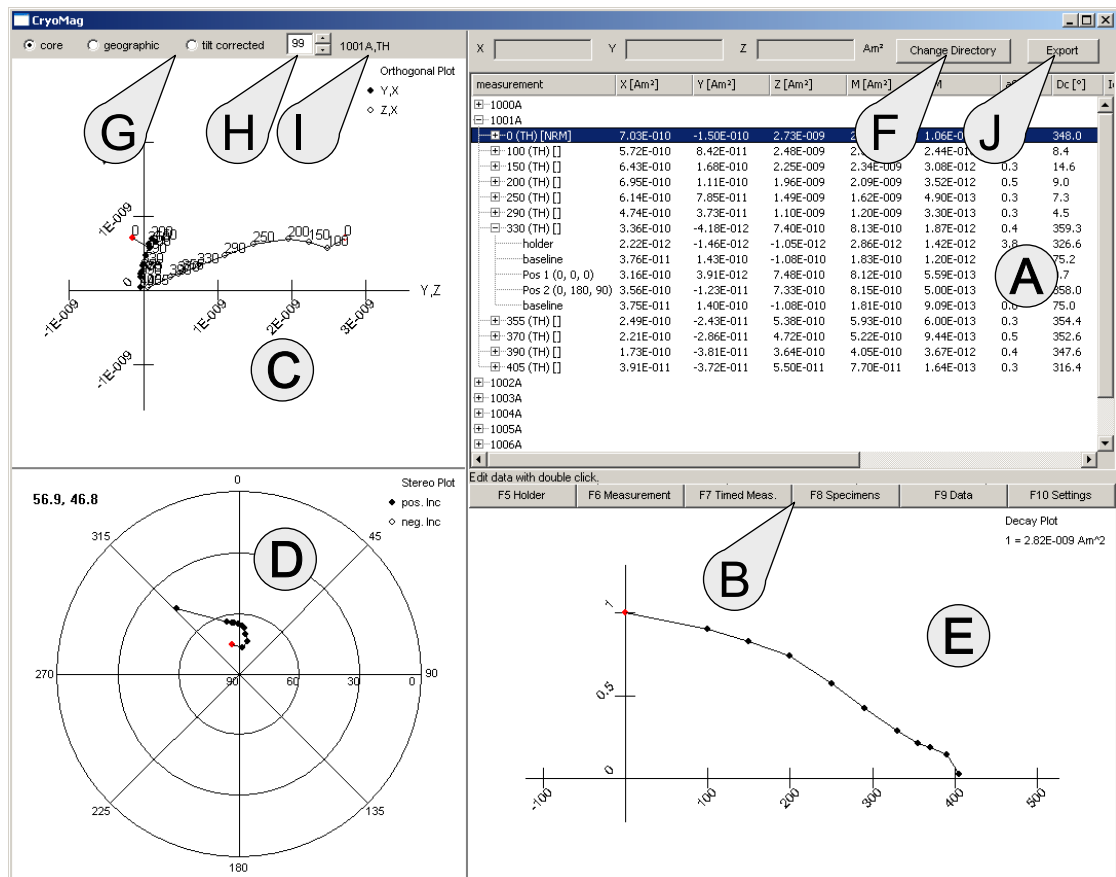
Figure 2.1.: Main window of CryoMag with activated data panel. A - active panel; B - button row to select main functions; C - orthogonal plot; D - stereo plot; E - decay plot; F - button to change data directory; G - coordinate system selector; H - max. number of steps plotted; I - name of plotted specimen; J - button to export data to various formats

3-component SQUID magnetometers, yet most functions and displays are similar for spinner magnetometers.

2.2.1. Settings

All settings are reset to reasonable default values at program startup and can be modified by the users for their needs (figure 2.2). Some fundamental settings that should not be changed during regular use can only be modified by editing a configuration file called *CryoMagSettings.py*. These include the definition of the

Figure 2.2.: Settings panel. Measurement positions and baseline configuration.

different sets of measurement positions, the calibration factors of the sensors, the type of instrumentation and the number of averaged readings per measurement. To avoid unwanted changes to critical parameters the configuration file can be write protected via the operating system.

Holder Positions

Holder measurements can be carried out in two ways. The default is to measure the holder in four positions, each time turned by 90 degrees about the (vertical) z-axis of the magnetometer (counterclockwise seen from above). The other option is to measure the holder four times in the same position.

Specimen Positions

Different measurement schemes, consisting of several predefined measurement positions, can be selected. Measurement positions are defined by three Euler angles.
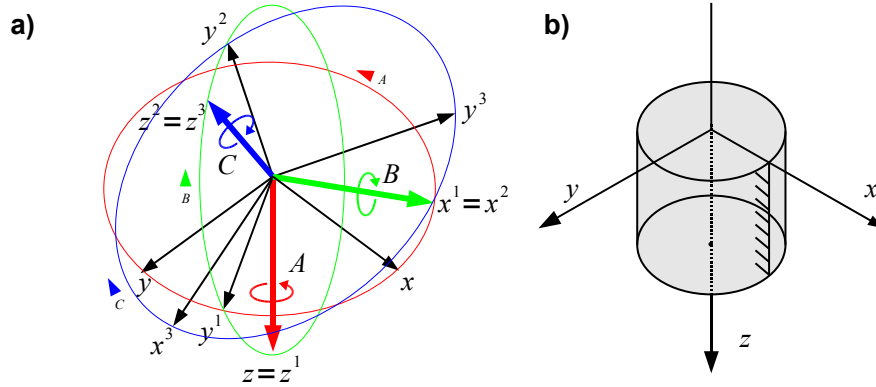
Figure 2.3.: a) Orientation of a specimen can be represented by three Euler angles A, B, C describing three subsequent rotations around z, x^1, z^2. x, y, z are initial axes, $i^n (i = x, y, z)$ denotes i-axis after n-th rotation. Therefore $n = 3$ indicates final axes. Elliptical shapes are perspective circles perpendicular to each corresponding rotational axis (drawn bold). Rotations are always clockwise when looking toward the origin. Figure redrawn from *Czichos* (1996); b) Coordinate system of a specimen with an unique mark on its shell along its z-axis. Y-axis is chosen so that it is in-situ horizontal and x-axis points upward.

The rotation is given by three angles A, B, C, where the first rotation is by an angle A about the specimen's z-axis (z in figure 2.3), the second is by an angle B about the specimen's (rotated) x-axis (x^1), and the third is by an angle C about the specimen's (rotated) z-axis (z^2) (*Czichos*, 1996). Internally, the rotations are performed using the following rotary matrices.

$$
\check{M} = \begin{pmatrix} c_A & -s_A & 0 \\ s_A & c_A & 0 \\ 0 & 0 & 1 \end{pmatrix} \cdot \begin{pmatrix} 1 & 0 & 0 \\ 0 & c_B & -s_B \\ 0 & s_B & c_B \end{pmatrix} \cdot \begin{pmatrix} c_C & -s_C & 0 \\ s_C & c_C & 0 \\ 0 & 0 & 1 \end{pmatrix} =
$$

$$
= \begin{pmatrix} c_A c_C - c_B s_A s_C & -c_B c_C s_A - c_A s_C & s_A s_B \\ c_C s_A + c_A c_B s_C & c_A c_B c_C - s_A s_C & -c_A s_B \\ s_B s_C & c_C s_B & c_B \end{pmatrix}
$$

with $\qquad c_X = \cos X; \; s_X = \sin X$

The standard position (all angles equal zero) means that the axes of the specimen are aligned with those of the magnetometer which should be chosen according to the arrangement of the SQUID sensors and the user's conventions.

Baseline

Since SQUID sensors can only measure relative changes of magnetic fields, a zero-point has to be defined. This is done by reading the sensor's baseline without any specimen present. Subsequent measurements of specimens are always corrected for this baseline value. To overcome potential instrumental drift, it is advisable to measure baselines as often as possible. Cryomag provides the possibility to measure baselines before and after the measurement of all positions of one specimen or before each individual position. The user can specify a warning threshold in the lower part of the settings panel. If the difference between two subsequent baselines during the measurement of a specimen is greater than the chosen warning threshold (figure 2.2, bottom), a message will be displayed.

2.2.2. Measurement

Measurement of the holder or specimen can be started by selecting 'Holder' or 'Measurement' from the button row. The measurement itself works in a very similiar way for holders and specimens. In the case of a specimen, before each step, a specimen name, a step value and type and optionally a comment must be supplied in the corresponding edit fields (figure 2.4). Pressing Enter on any field accepts the default or modified value and moves the cursor to the next field. Pressing Enter in the comment field activates the first measurement as specified earlier by the user in the settings panel. A short status message and the properties of the current specimen are shown in the upper part of the measurement panel. Each measurement can be executed by pressing Enter. In this case, the x-, y-, z-component of the magnetic moment is read several times (by default three times; defined in the configuration file, see section 2.2.1) from the magnetometer and averaged. Then the values of the most recent baseline and of the holder are subtracted and the

Figure 2.4.: Measurement panel. Step data was entered and first baseline was measured. Pressing Enter will start specimen measurement in position 1. Numbers in brackets indicate specimen orientation.

resulting vector is written to the screen after accounting for the Euler angles which define the orientation of the specimen (see section 2.2.1). The results are filled in the appropriate columns in the measurement list (*i.e.* x, y and z-component of magnetic moment, total moment, standard deviation of the total moment, half angle of 95% confidence cone *a*95 (*Butler*, 1992), inclination and declination in core coordinates). The standard deviation and *a*95 are based on the variation of the repeat readings of the magnetometer (the default is 3, but the user can change this in the settings panel). All completed measurements can be repeated by pressing the corresponding number key on the keyboard.

Pressing Enter after the last measurement activates the calculation of the results. The vectors of the individual measurements are averaged. Now the standard deviation and *a*95 is calculated on the basis of the number of data accumulated directly from the individual measurement positions. The results of the current step are presented in a dialog together with the values of all previous steps of the specimen. This provides an easy way to check the data for consistency by looking at the evolution of the values and statistical parameters. The 'Save results' button of the dialog stores the calculated results as well as all data from each individual position measurement in the specimen's data file, 'Cancel' hides the dialog and allows to repeat individual measurements as described above. To restart a measurement step from the beginning a new one has to be started by selecting 'Holder' or 'Measurement'. Measured but unsaved data is discarded in this case.

	specimen	coreaz [°]	coredip [°]	bedaz [°]	beddip [°]	volume [cm³]	weight [g]
1	1000A	130	32	290	12	11	32
2	1001A	132	45	290	12	11	43
3	1002A	122	80	290	12	11	34
4	1003A	118	66	290	12	11	36
5	1004A	97	4	290	12	11	38
6	1005A	133	47	290	12	11	33
7	1006A	176	85	290	12	11	41
8	1007A	145	12	290	12	11	43

Figure 2.5.: Specimen panel. Field data and properties of specimens can be edited.

To study viscous magnetization, a timed measurement mode is available. In this case, measurements of the magnetic moment are carried out automatically at predefined time steps after measuring one baseline at the beginning. Time steps in seconds can be defined according to the equation $t = \{n \cdot i^x \ \forall \ n \in \mathbb{N}\}$. The range of i as well as the variables n and x can be selected by the user. Choosing $x > 1$ allows increasing time intervals to support exponentially decaying magnetic moments. It is assumed that the specimen's axes coincide with those of the instrument which corresponds to a value of zero for the three Euler angles introduced above. The magnetization of a previously measured sample holder is subtracted.

2.2.3. Specimens - Field Data

Selecting 'Specimens' from the button row activates a panel that shows a list of all specimens in the current data directory (figure 2.5). It is possible to enter or change the field data (*i.e.* core orientation, bedding) and properties (mass, volume) of each specimen. The core azimuth describes the geographic direction of the drill hole (0° = north, 90° = east, ...), core dip defines the angle between the core surface (x-y plane) and the horizontal (0° = core z-axis downwards, 90° = core z-axis horizontal). Bedding azimuth describes the dip direction. Bedding dip is defined as the angle to the horizontal. All changes are directly saved to the individual data files (see section 2.3) and used for coordinate and unit conversions.

2.2.4. Measurement Data

All data from the files in the current data directory are presented in a hierarchical structure (figure 2.1 A). For each measurement, data for all positions, baselines and subtracted holder data is recorded. This can help to identify inconsistencies and potential error sources in the recorded data. When selecting steps (e.g., temperature, AF field, etc.) in the directory, the corresponding points are highlighted in red on the plots. Hitting the DEL key allows to delete data of one individual step. This is permanent but has to be confirmed by a warning given in an extra dialog box. Double clicking with the mouse on an entry allows to edit its properties. In this way the names of specimens as well as the properties of their steps (step, type and comment) can be changed. Other data manipulations (such as the deletion of specimens or the movement to an other directory of specimens) cannot be performed inside *CryoMag* and should be done with means of the file system. When doing so, one has to reload the data into *CryoMag* by means of the "Change Directory" button (figure 2.1 F).

2.2.5. Data Visualization

A graphical representation of the measurement results is always available. Each data point corresponds to one step and is simultaneously displayed in an orthogonal projection, a stereonet, and a normalized decay plot. The coordinate system of the plots can be switched between core, geographic and bedding corrected coordinates by selecting the corresponding button above the orthogonal plot (figure 2.1 G). Individual points can be selected by a mouse click. The corresponding points in all plots are then marked red. The same is true if an individual step is selected in the data panel. This helps the operator to keep track of the data and its evolution with progressing demagnetizing steps. The orthogonal plot, also known as a Zijderveld diagram (*Zijderveld*, 1967), shows the 3D data on vertical and horizontal planes as well as directional information in one common coordinate system (figure 2.1 C). Opening a context menu by right clicking on the mouse on the plot allows one to change the projection planes.

The decay plot shows the magnetic moment measured in each individual step divided by the maximum magnetic moment (intensity) as a function of temperature or peak alternating field (figure 2.1 E).

The context menu of each plot allows one to save the plot as an EPS (Encapsulated PostScript) file for treatment in external applications. To magnify weak magnetizations normally observed in later demagnetization steps, the number of plotted data points can be temporarily reduced. These data are not permanently deleted and can be recalled by increasing the number of plotted data points. This rescales all plots to the new data range. The number of data points can be selected beside the projection selection (figure 2.1 H). The default is 99, meaning that up to 99 data points will be shown in each plot (counting backwards from the last step). Adjacent to that one the name of the currently observed specimen and the type of the first step (e.g., AF or TH) is shown (figure 2.1 I).

2.3. Data Management and Format

2.3.1. XML Based Data Files

The data of each specimen is collected in a separate file called *'specimen-name'.cmag.xml* in the current working directory. The working directory can be changed within the program by pressing the button 'Change Directory'. The data of the holder measurements are stored in the user's home directory (on Linux: */home/username*) as *'holder.cmag.xml'* in the same format as the data of the specimens. Amongst other things, this allows one to monitor the magnetization of the holder over time. The file format is XML (eXtensible Markup Language) (e.g., *Harold and Means*, 2001) based, which allows reading and editing with any XML or plain text editor. The hierarchical structure of XML enables storage of non tabular data without redundancy. An example of a file can be found in Appendix B.1. A XSL (eXtensible Stylesheet Language) transformation (*cryomag.xsl*) is provided to allow the data files to be viewed in any modern web browser (figure 2.6). To do so the XSL file must reside in the same directory as the data files. The creation of custom XSL files enables the user to adapt the output to his needs. Measurement data including the individual specimen positions, baselines, times and statistical parameters are stored and can be accessed through the data panel.

Figure 2.6.: Example data file opened in standard web browser. Browser renders XML data to a user-friendly output by use of an XSL transformation.

2.3.2. Export Formats

For using the data in other applications an export function is provided. Clicking on 'Export' (figure 2.1 J) allows the user to pick a file format and a name or directory. All data from the current data directory is exported to the file(s). Exporting a subset is possible by either editing the resulting file by hand or copying the desired specimen data files to a temporary directory and selecting this as the data directory in *CryoMag* (see above). Different possible output formats are described in the next sections.

Palmag

Palmag is a software program (written by Florian Maier and Valerian Bachtadse) which allows to carry out measurements with the 2G SQUID magnetometer as well as to analyze the data. Measurements exported to its file format (.dat) are converted to magnetizations in [mA/m] using the volume specified in the specimens panel and can be loaded with *Palmag* for further analysis.

Paleomac

Paleomac[5] is a paleomagnetic analysis program run on Macintosh computers (*Cogné*, 2003). Demagnetization data can be imported as text based .pmd files which can be generated directly by *CryoMag*.

Standard MagIC Text File

The Magnetics Information Consortium (MagIC)[6] provides a global online database for all kinds of paleomagnetic and rock magnetic data. By means of MagIC Console Software package, which is programmed in Microsoft Excel and can be used on both PC's and Macintosh computers, it is possible to prepare and complement the measurement data of CryoMag for import into the database.

CIT Format (PaleoMag)

PaleoMag [7] (*Jones*, 2002) uses an ASCII file format[8] which has been in use in the paleomagnetics laboratory at Caltech. It consists of one .SAM file that describes the sampling locality and contains a list of specimen files. Each of these includes core and bedding orientation as well as data for all measured steps of a single specimen.

---

[5]http://www.ipgp.jussieu.fr/~cogne/pub/paleomac/PMhome.html
[6]http://earthref.org/MAGIC/index.html
[7]http://cires.colorado.edu/people/jones.craig/CHJ_PMag_overview.html
[8]http://cires.colorado.edu/people/jones.craig/PMag_Formats.html

IAPD Format

(Super) IAPD[9] (INTERACTIVE ANALYSIS OF PALAEOMAGNETIC DATA) is a program written for PC clones by Torsvik and others. The file format is ASCII with fixed length fields similar to Palmag.

ASCII Result File

All steps of all specimens are exported to a single text file. Each line represents a single measurement step and incorporates the following items separated by tabs: specimen name, core azimuth, core dip, bedding azimuth, bedding dip, volume, weight, step, x-, y- and z-component of magnetic moment in $[Am^2]$, total magnetic moment in $[Am^2]$, declination and inclination in core, geographic and bedding corrected coordinates. Optionally it's possible to amend the measurements of all individual positions to each step. This format can be easily imported in popular spreadsheet applications and converted as needed.

Specimen List

This option exports a list of specimens and their input parameters like weight, volume and the field data to an ASCII file. Each line represents a specimen and incorporates the following items separated by tabs: specimen name, core azimuth, core dip, bedding azimuth, bedding dip, volume, weight.

2.4. Case study

To verify the correct functioning of the software a case study was carried out on six Neogene continental sediments from the Tarim basin, China (*Gilder et al.*, 2001). Here we studied an artificial anhysteretic remanent magnetization imparted along the z-axis of the specimens using a 100 mT peak AC field with a biasing DC field

---

[9]http://www.geodynamics.no/software.htm

of 0.05 mT. The magnetic moment of the specimens was measured at distinct time steps to reveal the expected logarithmic decay of the magnetic moment with time (figure 2.7). The direction of the magnetic moment of all specimens was close to the expected direction along the z-axis (I => 83°) and stable over time (a95 <= 0.2°). Table 2.1 lists the specimens, their acquired magnetic moments beginning one minute after applying the ARM and the parameters of the best-fit lines according to the equation $M = 1 - A * \ln(t)$. Most magnetizations decrease by more than 3 percent during the first hour. These values demonstrate that the timing of such measurements can have a significant influence on the results.
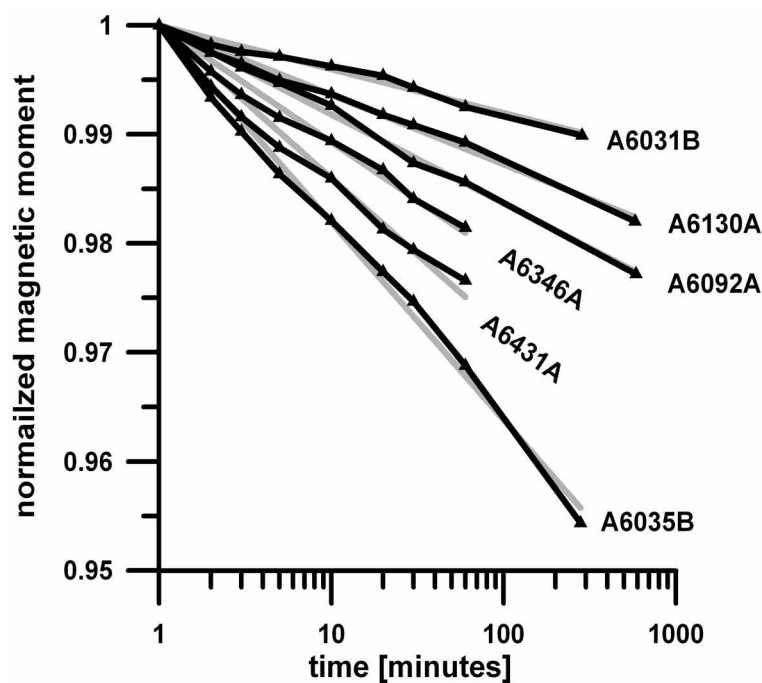
Figure 2.7.: Viscous decay of an ARM of six selected samples.

2.5. Conclusions

The *CryoMag* software provides an optimized workflow for routine paleomagnetic measurements and aids the operator to quickly assess the relevant data in form of statistical parameters and diagrams. The storage of raw data of individual

specimen	M [10^{-7} Am^2]	R^2	A [10^{-3}]
A6031B	4.54	0.98	1.75
A6035B	2.56	0.99	7.85
A6092A	2.85	1.00	3.55
A6130A	3.16	0.99	2.77
A6346A	1.88	0.98	4.65
A6431A	1.07	0.98	6.09

Table 2.1.: List of specimens. M = total magnetic moment one minute after applying an ARM; R^2 = correlation coefficient, and A = slope of best-fit line.

measurement positions and the magnetic moment of the holder facilitates the analysis of potential inconsistencies in the measurements at a later date. The export to common file formats allows the use of existing analysis programs. Test measurements demonstrate good functioning of the presented software. *CryoMag* has been in regular use since June 2008 in the geophysical magnetic laboratories of the Ludwig Maximilians University, Munich. It is used to operate two cryogenic SQUID magnetometers manufactured by 2G Enterprises (type 755 and 760) and a JR-4 spinner magnetometer built by AGICO Inc.

3. The SushiBar: An Automated System for Paleomagnetic Investigations [1]

We present a new, automated system based on a three-axis superconducting magnetometer and a custom-made coil designed to experiment on cylindrical specimens used in typical paleomagnetic investigations. The system, which resembles a sushi bar, facilitates stepwise alternating field demagnetization of up to 99 samples per loaded track. It also enables researchers to explore magnetic properties using an anhysteretic remanent magnetization (ARM) in any coercivity window up to peak alternating fields of 95 mT with direct current bias fields up to 0.17 mT. For example, partial ARM (pARM) spectra characterize magnetic grain size distributions in rocks, yet rarely are pARM spectra measured because the complete curve for one sample takes at least two hours to acquire manually. The SushiBar achieves 99 such curves in slightly less than 100 hours. Using the SushiBar, we measured the pARM sprectra, as well as the viscosity and anisotropy of ARM in three discrete switching field windows, of continental sediments from the Xishuigou section (western China). The average grain size remains constant along the 2200 m-thick section, yet magnetic viscosity varies systematically from bottom to top of the section; samples with high magnetic viscosities also have higher proportions of non-viscous material on average. Principal anisotropy axis directions from the lowest switching fields correlate well with principal axis directions from anisotropy of magnetic susceptibility. Principal axis directions defined at higher switching

---

[1]Published as part of: Wack, M.R. and Gilder, S.A., The SushiBar: An automated system for paleomagnetic investigations, Geochemistry Geophysics Geosystems, 2012, in press.

fields systematically deviate from those at lower switching fields, perhaps defining the fabric of the remanence carrying grains.

3.1. Introduction

Modern paleomagnetic investigations are typically based on stepwise demagnetization of the remanent magnetization of hundreds to thousands of oriented samples. To minimize uncertainty and systematic error, each sample is measured (usually manually) in multiple orientations with respect to each sensor of the magnetometer. Often 12 to 20 demagnetization steps are required to precisely define the magnetization components in rocks; thus, the data acquisition process can last several months. This time investment does not include peripheral analyses to understand the carrier(s) of the magnetic remanence or to identify potential sources that may have deviated the magnetic vector in the rock away from the true paleofield direction (e.g., inclination shallowing). The immense number of data points, and hence the required workload, hampers the systematic study of complex properties like the anisotropy of magnetic remanence. Increasing the complexity and number of measurement schemes increases the risk of error, making the need to develop automated schemes even greater.

As reviewed by *Morris et al.* (2009), automation of rock magnetic measurements emerged in the late 1960s. Here we briefly recall the automated systems based on superconducting rock magnetometers developed in the 1970s (*Goree and Fuller*, 1976), which provide the highest sensitivity in magnetic moment (noise levels around 10^{-11} to 10^{-12} Am^2). Table 3.1 gives an overview.

The Cardiff automated system uses a single SQUID sensor with a pickup coil inclined 45° in a gradiometer configuration (*Shaw et al.*, 1984). This enables orthogonal measurements of the magnetic moment by rotating the sample around its z-axis. Two orthogonal alternating field (AF) coils and a furnace are mounted in-line. Both are enclosed by orthogonal field coils facilitating automatic anhysteretic remanent magnetization (ARM) and thermal remanent magnetization (TRM) experiments. A single 9 mm diameter core is manually attached to a sample handler that is

Table 3.1.: Properties of SQUID-based, automated measurement systems.

Instrument (see text)	Redundant sample positions	No of discrete samples	Automatic heating	Parallel operation	Holder moment
Cardiff (*Shaw et al.*, 1984)	1	1	yes	no	$5 \cdot 10^{-12}$ Am^2
2G Enterprises Inc.	1	8	no	no	$< 10^{-9}$ Am^2
Canberra (*Giddings et al.*, 1997)	6	1	no	no	$4 \cdot 10^{-10}$ Am^2
Bremen	2	96	no	no	see 2G system
Caltech (*Kirschvink et al.*, 2008)	4	180	no	no	$1 \cdot 10^{-12}$ Am^2
Santa Cruz (*Morris et al.*, 2009)	6	1	no	no	$< 10^{-9}$ Am^2
Munich (this publication)	3	99	no	yes	$3 \cdot 10^{-10}$ Am^2

moved vertically using compressed air and rotated by a stepper motor. The total height of the system is 3.6 m, which is tall for most shielded rooms.

Besides the Cardiff system, others use three-axis, superconducting magnetometers that measure the full vector of the magnetic moment. To eliminate problems with gain of the electronics or non-perfect positioning of the sample with respect to the sensors, the ideal measurement protocol requires independent measurement of the sample's ±x, ±y and ±z axes on each of the three magnetometer sensors (*Collinson*, 1983). *Giddings et al.* (1997) fulfilled this stringent requirement by developing a system with a sample handler that flips a sample by ±90° around an axis orthogonal to the rotational axis of the sample holder. This, together with a transverse AF/ARM-coil placed in-line with the magnetometer, permits static AF demagnetization in three orthogonal directions as well as partial ARM treatments with a single coil followed by subsequent measurement of the magnetization on a single sample. The measurement protocol is optimized to neutralize potential gyro-remanent magnetization, which is common in greigite-bearing rocks (*Stephenson*, 1980; *Dankers and Zijderveld*, 1981; *Hu et al.*, 1998, 2002).

2G Enterprises offers the only commercially-available automated system. It has a 5.8 m long, horizontal track that passes through the bore of the magnetometer. Users place discrete samples into sample holders or a single u-channel (from marine drill-strings) onto the track. The length of the track and the spacing needed to avoid interference dictates the number of permissible discrete samples (commonly eight). Three coils placed in-line with the magnetometer facilitate automatic AF demagnetization; a system to measure bulk susceptibility is sometimes placed

in-line. Three complete passes are needed to demagnetize a sample, one for each axis; the samples are measured in a fourth pass. The system can be equipped with ARM and pulse magnetizers. Disadvantages with the system are: (1) sample magnetizations are measured in only one position unless the user manually changes the orientation of the sample. (2) The track and its holder remain permanently within the bore of the magnetometer. (3) The length of the system requires an equally large shielded room (although some laboratories have no shielded room). (4) The AF demagnetization routine is accomplished by ramping up one coil to the desired peak field and held there until all the samples pass through it. Decay of the alternating field in time (dH_{af}/dt) depends on the spatial gradient dH_{af}/dx and the translation speed dx/dt. (5) Potential discrepancies between the three AF coils can lead to inhomogeneous demagnetization (e.g., the coils have peak fields that deviate from the commanded field in different proportions with respect to each other; S. Gilder, unpublished data).

Tilo von Dobenek and Thomas Frederichs (University of Bremen, unpublished) enhanced the 2G system with a pneumatically-driven robotic arm that automatically transfers up to 96, 8 cm^3 cubic samples from a nearby tray onto the 2G track and then back again into the tray. By placing an individual cube on a rotary plate, the cubes can be rotated 180° about a vertical axis, therefore allowing users to measure the samples in two orientations with inverted x and y axes. The paleomagnetism laboratory at the University of Utrecht has adopted the Bremen system (e.g., *Gong et al.*, 2008).

Kirschvink et al. (2008) developed a novel system at the California Institute of Technology (Caltech) where up to 180 standard inch specimens (2.5 cm diameter × 2.2 cm height) are transported laterally on a snake-like chain over a magnetometer. A quartz tube positioned above the sample tray couples with the top surface of the cylindrical samples via an air vacuum. The sample is lifted up, the tray moves to an open spot in the track, and then the sample is lowered into the magnetometer through the open slot. The sample is rotated about its z-axis for multiple measurements. Users can manually flip the samples about their x-axes and repeat the cycle if they desire to measure the sample's -z-axis on the z-axis of the magnetometer. Two orthogonal coils lay in-line, above the

magnetometer for automatic AF demagnetization or acquisition of an isothermal remanent magnetization (IRM). An additional coil measures susceptibility while another imparts bias fields for ARM experiments. An outstanding feature of this system is the lack of sample containers. The only magnetic contamination during measurement comes from the quartz glass tube (essentially non-magnetic), thus allowing one to measure very weakly magnetized samples (up to the baseline noise of the magnetometer). Seven laboratories worldwide now use the Caltech system and several more are in preparation (Joe Kirschvink, personal communication, 2011), which means an improvement to the system by one member of the consortium can, in principle, be adopted by the rest. Moreover, the surface area required by the system is minimal – on the order of 2 m^2. Disadvantages with the Caltech system are: (1) because the complete system is configured on a vertical line, one needs a shielded room with a height of more than 3 m to have enough distance between the AF / IRM coil and the samples on the track. This often requires a hole to be cut in the roof of the shielded room. (2) Adding further components is problematic due to space restrictions. (3) After users place the samples on the track, there is no independent verification that the sample does not become misoriented when the chain moves during operation. To our knowledge, no back-to-back repeat measurements have been reported to demonstrate measurement reproducibility. (4) Two independent coils are required for AF demagnetization.

Morris et al. (2009) (University of California at Santa Cruz) introduced a horizontal automated system that uses a sample holder similar to that designed for the AGICO JR-5A spinner magnetometer. The holder allows cylindrical specimens to be rotated about their body diagonals, meaning that only one coil is needed for AF demagnetization or, importantly, to measure ARM anisotropy, albeit only on one sample at a time – users must change the samples manually.

Below we describe a new automated system for paleomagnetic research that is advantageous in terms of volume of samples, speed of operation and versatility in number of techniques. This system has been in continuous operation since March 2011 at Ludwig Maximilians University, Munich. We affectionately call it the SushiBar due to its resemblance with the way sushi is served on revolving tracks at some restaurants. A complete description of how the SushiBar works is given,

together with calibration and test measurements. We then present data acquired by the SushiBar from 96 samples collected at the Xishuigou section (Subei, Gansu Province, western China)(chapter 4).

3.2. Setup

3.2.1. System Overview

The backbone of the system is a horizontal, two-meter diameter circular track that contains 100 regularly spaced holes (figure 3.1). Within each hole lies an insert designed to support cylindrical cores (up to 2.5 cm in diameter) and their holders (called cups). The inserts can be replaced to fit different sample cup geometries if required in the future. Passively-rotating, plastic+rubber wheels fit into a groove machined into the sides of the track. The wheels keep the track centered and suspended. Individual stepper motors drive four of the wheels to rotate the track. Two independent light barriers, triggered by holes drilled vertically through the track, ensure position control. One provides an absolute reference for the entire track, the second, for each sample. This allows the system to precisely control the location of each specimen relative to the instruments and their sample handlers. Additionally, the number of motor steps relative to the turning angle of the track is recorded to monitor potential misalignment. In case of an ambiguous position in terms of number of motor steps used, the track is commanded back to the absolute reference position and then turned back to the demanded position.

Situated below the track are sample handlers that lift the cups containing the specimens off the track, into the instruments, and then repose them after (figure 3.1). A three-axis, 2G Enterprises superconducting rock magnetometer and a custom-built ARM coil sit above the track. Separation of the workstations (magnetometer and coil), each with an individual sample handler, allows the SushiBar to perform multiple operations simultaneously and independently (e.g., AF demagnetization on one sample and magnetic measurement on another). Especially for stepwise measurements like AF demagnetization, this reduces the total time needed by a
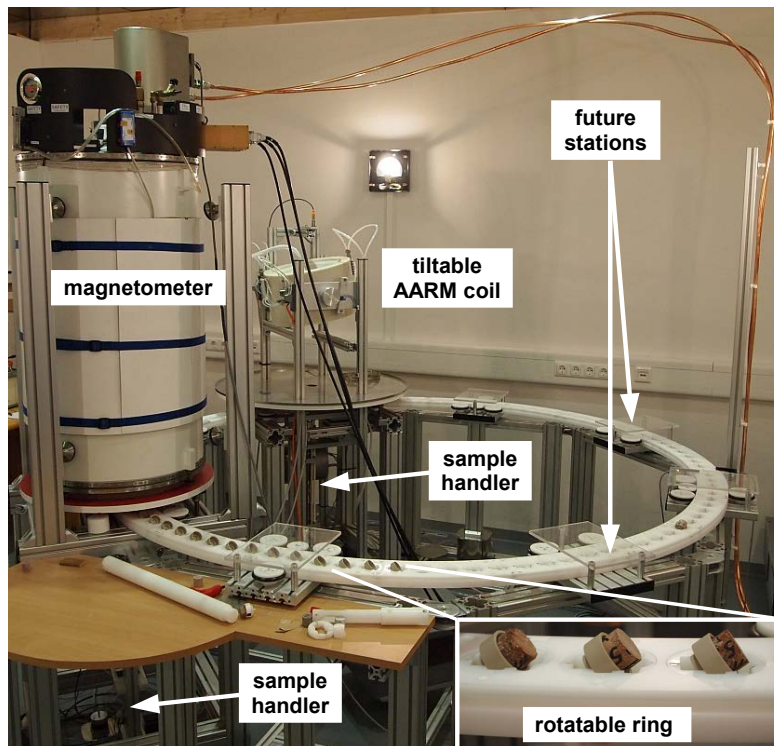
Figure 3.1.: Overview of the SushiBar. The system is equipped with a 2G Enterprises Inc., three-axis, superconducting rock magnetometer and a custom-made ARM coil (see figure 3.6). Some empty sample cups (inset lower right, cups with samples) lie on the 2 m-diameter track that is supported and rotated by wheels on the sides of the track. Mu-metal shielding of the AARM coil is removed for illustration. In the future, additional workstations for acquisition of isothermal remanent magnetization and magnetic susceptibility measurements can be added.

factor of the number of instruments used, since they operate in parallel most of the time. One full turn of the track to demagnetize (one step) and measure 99 specimens takes about 4 hours (2.4 minutes per specimen).

3.2.2. Measurement Environment

We first built a magnetically shielded room that would fulfill the following requirements: (1) the SushiBar was designed for a track of two meters in diameter, plus an additional meter was needed for the workstations (figure 3.1). Hence, the surface of the room had to be a minimum of 4 m x 4 m (16 m^2) when also accommodating

people. (2) The magnetometer (2G Enterprises, 755 SRM, 1.4 meters in total height) would stand one meter above the floor. At least 0.4 m above the magnetometer had to be free for yearly liquid helium refilling. Thus, the inside of the room had to be ca. 3 meters tall. (With the new generation of liquid helium-free magnetometers, the height of the room can be reduced by a meter.) (3) To avoid potential viscous remagnetization of the samples, we wanted the ambient magnetic environment to have a residual field of less than 1000 nT. In the end, the interior dimensions of the magnetically shielded room were 5 m x 6 m x 3 m = 90 m^3. The room is shielded using two shells of two overlapping layers of remagnetized transformer steel followed by one layer of 1 mm-thick mu-metal (see chapter 1). The samples on the track experience a maximum magnetic field of 1100 nT, with an average of 500 nT. This includes stray fields coming from the SushiBar itself, as only weakly-magnetic materials like aluminum, stainless steel, brass and plastic were used in construction. Electronic devices that do not directly operate the SushiBar (amplifiers, computers, etc.) are located outside the mu-metal shielding. Mu-metal encloses all components producing potentially significant stray fields like the actuation motors and the AF-ARM coil.

3.2.3. Sample Handling

Samples are manually inserted into a plastic (PEEK – polyether ether ketone, traded as ZEDEX-324 by Wolf Kunstoff-Gleitlager GmbH, Germany) cup whose inner wall is covered by the stiff side of Velcro. ZEDEX-324 was used because of its low magnetization and high degree of hardness, which makes it easier to machine reproducibly than softer plastics. This simple cup design accommodates irregularly shaped samples, including those with fractures, vesicles, etc. Samples are oriented so that their reference mark is aligned with the reference mark on the sample cup (figure 3.2a). A thin strip of reflective material (retro-reflector) lies on the outside of the sample cup. These enable position control via a reflected light switch from lasers fixed above the instruments. Up to 99 sample cups are laid in the inserts on the track such that the sample's z-axis (axis of symmetry) is aligned tangentially to the track and inclined by 35.3° (body diagonal) from the horizontal (figure 3.2b).
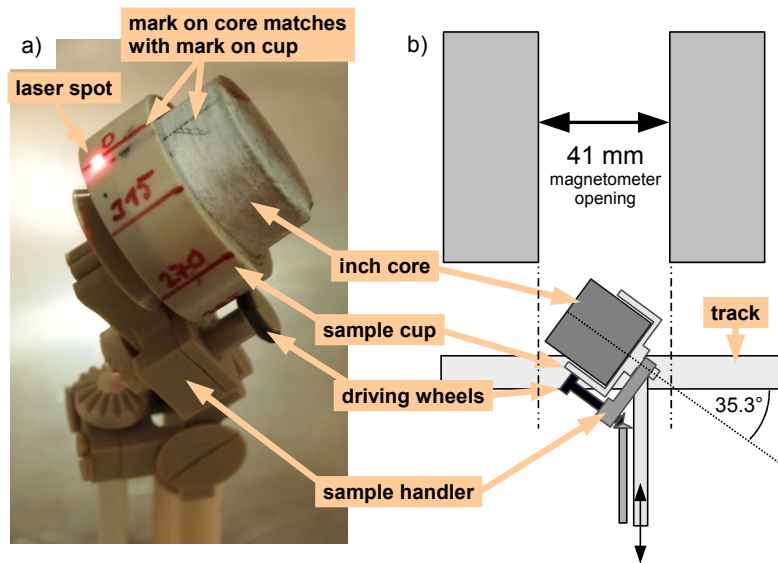
Figure 3.2.: a) Photo of the sample handler, sample cup and inch core specimen. Laser light is hitting the reflective material at the zero (orientation) mark. b) Schematic cross section of sample handler at the entrance to the opening of the magnetometer.

One insert on the track is left empty so the magnetization of the sample handler can be measured and subtracted away. Two small wheels on the sample handler support the sample cup and spin it about its z-axis (figure 3.2); the bottom of the cups have a nipple that passively slides in and out of a grooved guide on the sample handler to facilitate positioning and rotation.

The rotation angle is controlled by the number of motor steps relative to the number of steps needed for one full revolution of the sample cup. Reflected laser light verifies the starting and final orientation of the cup each full round (normally 3 x 120°) of measurements. Figure 3.3 demonstrates the precision of the cup's orientation by comparing the number of motor steps per sample revolution between two independent runs for 50 samples. The data indicate a deviation of less than 2° for all samples and less than 1° for 90% of the samples. This geometry facilitates measurement and AF demagnetization in three orthogonal orientations relative to a fixed coordinate system (*Morris et al.*, 2009). In other words, rotating the cylinders in steps of 120° about their z-axes allows the three sample axes to be measured on each sensor of the magnetometer, and it permits full demagnetization
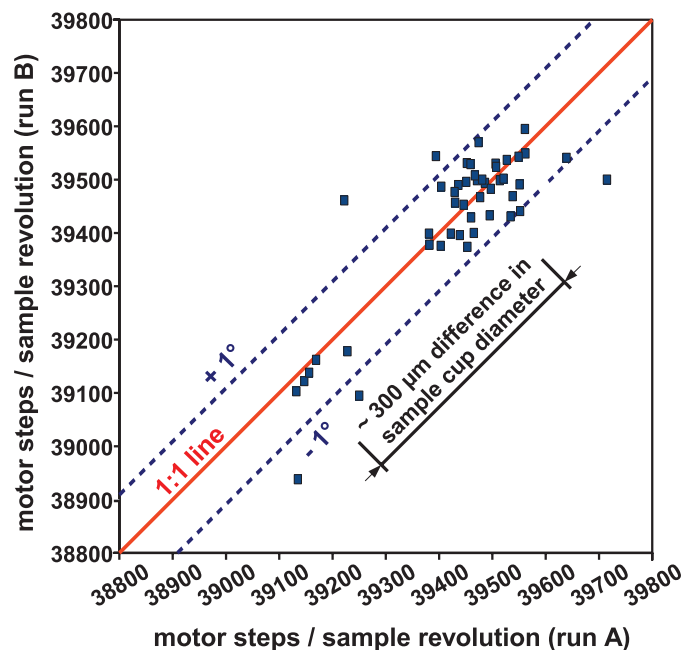
Figure 3.3.: Reproducibility of sample cup positioning. Positioning was determined by comparing the number of motor steps needed to rotate the same sample cup by 360° from two independent measurement runs for 50 specimens. Differences are less than 2° in all cases, 90% are below 1°. Number of required motor steps is largely a function of sample cup diameter.

of the three sample axes with a single coil. The sample handler could eventually be designed to rotate about its vertical axis to facilitate an automatic six-orientation measurement scheme that includes the negative directions of two axes.

The magnetic moments of the cup and the sample handler are greater than the baseline of the magnetometer so they must be subtracted to determine a sample's magnetization. Commercially available plastics commonly contain ferromagnetic substances (*Kobayashi et al.*, 1995). The ZEDEX-324 plastic yielded the lowest magnetic moments upon AF demagnetization and ARM acquisition within our test measurements. However, we found that the material is fairly inhomogeneous, so we made twice the number of cups (200) as was necessary then selected those with the lowest moments. The average magnetic moment of 99 cups AF demagnetized with a peak field of 90 mT is $1.4 \pm 1.1 \cdot 10^{-10}$ Am^2; ARM acquisition with a bias field of 0.1 mT and a 90 mT peak alternating field yields $2.9 \pm 1.2 \cdot 10^{-9}$ Am^2. The part of the sample handler that sits closest to the measurement region in the magnetometer

a)   directions in sample coordinates   b)   declination in sample coordinates
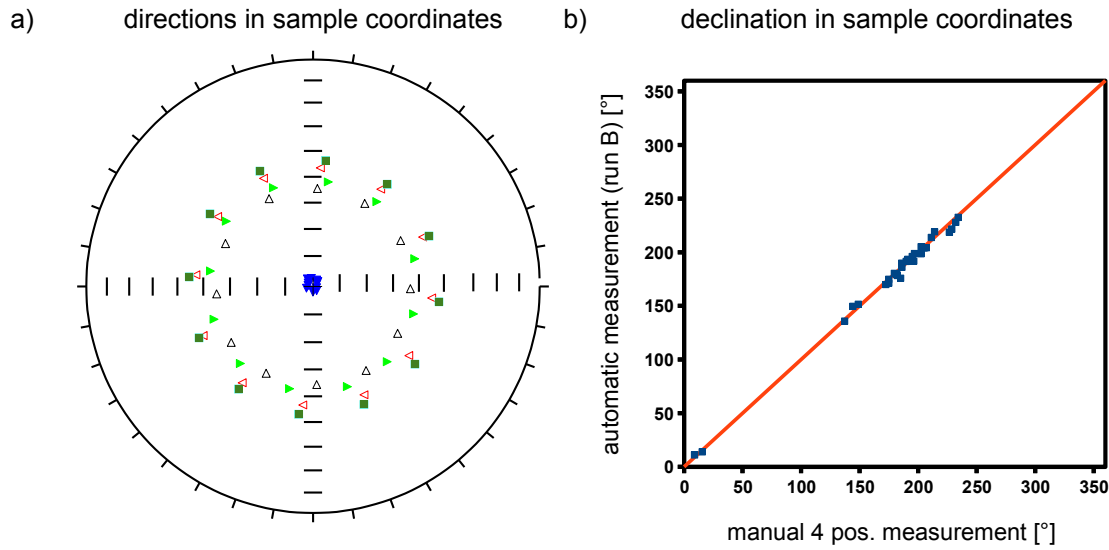
Figure 3.4.: Calibration measurements to determine measurement geometry. Results are used to transform instrument coordinates into sample coordinates. a) Averaged direction of 5 samples measured in 12 orientations. Directional mean defines the rotation axes ($I = 34.1°$, $D = 80.0°$ in instrument coordinates) of the sample handler. b) Comparison of 32 sample declinations measured manually and automatically to determine laser positioning.

is also made from ZEDEX-324 plastic (figure 3.2). The magnetic moment of the sample handler is around $3 \cdot 10^{-10}$ Am^2, with differences between subsequent measurements being on the order of the instrument noise level. The sample handler is measured before and after each measurement run. Its magnetization, together with the magnetization of the empty cup, is subtracted from measurements when samples are present; a specific cup must be assigned to each sample.

Accuracy of the directional measurements depends on knowing the sample's alignment with respect to the measurement system. Measuring several specimens in multiple orientations and averaging their directions defines the direction of the sample's spin axis relative to the measurement axis of the magnetometer (figure 3.4a). The laser probe was aligned by measuring samples with known declinations (figure 3.4b). A check of the quality and reproducibility of the data can be ascertained by comparing the magnetizations (moments of the x, y and z axes) of 50 sedimentary rock samples measured manually and then automatically on the SushiBar (figure 3.5a), and to compare the moments of the x, y and z axes between two
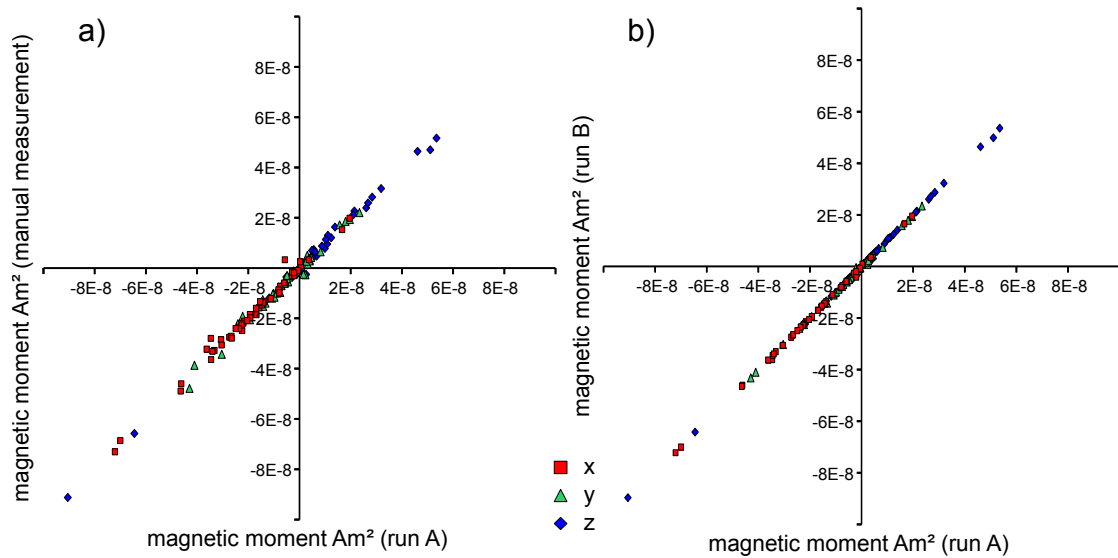
Figure 3.5.: Measurement reproducibility of 50 samples whose total magnetic moments range from $3 \cdot 10^{-9}$ to $1 \cdot 10^{-7}$ Am^2. a) Comparison of the three magnetic components measured manually versus measured automatically on the SushiBar. b) Comparison of the three magnetic components made by two repeat measurements made automatically on the SushiBar.

independent automatic measurements on the SushiBar (figure 3.5b). The former shows the compatibility and accuracy of a "known" magnetization relative to the SushiBar, while the latter shows how well the SushiBar provides reproducible data.

3.2.4. Coil for Alternating Field Demagnetization with a Direct Current Bias Field

The system was designed not only to demagnetize samples, but also to impart a direct current (DC) bias field for ARM studies. The alternating current (AC) windings of the coil, operated at their resonance frequency of 107 Hz, are connected in series with a capacitor and powered by a Crest (Meridian, USA) audio amplifier. The input signal of the amplifier is controlled by an ADWin Gold II (Jäger Computergesteuerte Messtechnik, Germany) real-time computer system with 16 bit in- and outputs which uses the current through the coil as a feedback to regulate the magnetic field intensity. Power supplies limit the maximum magnetic peak field

to 95 mT. The DC Helmholtz-like coil system is coaxial and rigidly attached to the AC coil system. It is powered by a bipolar supply controlled by the real-time system, which allows precisely timed switching of the DC field to impart an ARM in any desired switching field window. The maximum current of ± 2 A produces a magnetic field of ± 0.17 mT. The AC and DC fields were calibrated using a Lakeshore 455 Gauss meter and a Meda FVM-400 3-axis fluxgate magnetometer, respectively. The coil system is water-cooled and can be used continuously even at the highest fields. Finite element simulations done with the FEMM program (http://www.femm.info) predict a field homogeneity of 1.0% for the AC field and 0.4% for the DC field for a spherical volume, 32 mm in diameter. A cylindrical mu-metal shield reduces the residual DC field in the center of the coil to less than 35 nT; it is large enough (90 cm in diameter, 90 cm in height) to avoid the build up of eddy currents and concomitant field generation from alternating fields.

For routine AF demagnetization, a static coil would suffice given the sample handling design; however, to measure the anisotropy of remanence, an extra degree of freedom is needed to magnetize the samples along a range of body diagonals. The rotatable design proposed by *Box and Hunter* (1957) and adapted by *Hext* (1963) provides equally spaced directions on a unit sphere and ensures that the results are not biased by the orientation of the specimen relative to the experimental design. We follow the six-direction protocol of *Owens* (2000), which necessitates that the coil must rotate without interfering with the sample handler system. To satisfy these requirements, we built conical coils (36 cm outer diameter) with a triangular cross-section and arranged them in a Helmholtz-like configuration (figure 3.6). With this design, the coil system can tilt up to 90° around a horizontal axis perpendicular to the rotational axis of the sample cups by using a stepper motor and hardware switches at set positions. The middle position brings the coil axis to the vertical and allows three component AF demagnetization by turning the sample in 120° steps. The two other positions fix the coil axis either 90° or 45° relative to the rotation axis of the specimen (90° position shown in figure 3.6a).

In conjunction with switching the polarity of the DC bias field, as well as the rotational symmetry and the oblique rotation axis of the sample handler, an ARM can be imparted to the sample in any direction and in any switching field window
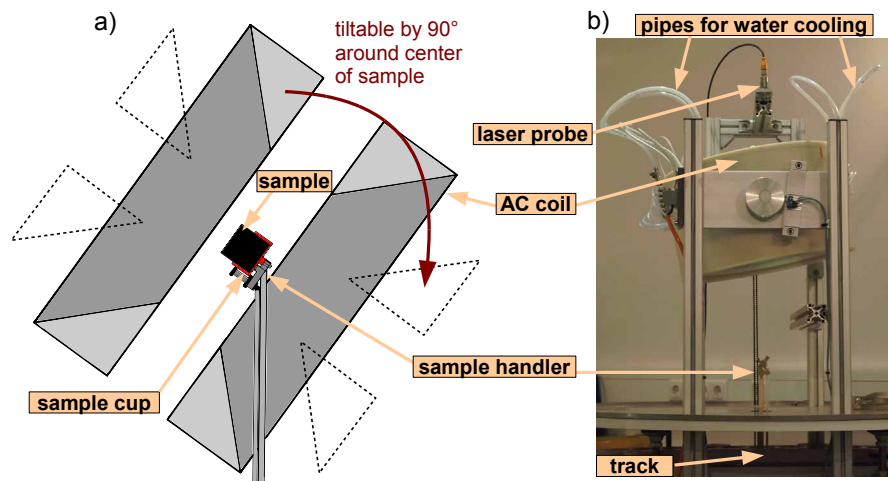
Figure 3.6.: a) Schematic cross-section of the ARM coil system and the sample handler loaded with a sample. Dotted triangles indicate coil position when tilted by 90°. b) Photo of ARM coil system without mu-metal shielding. The laser probe mounted on the top insures proper sample orientation; white-translucent tubes are for water-cooling.

up to 95 mT. To determine the ARM anisotropy tensor, we impart an ARM in 12 directions (six orientations with negative and positive DC field polarities) (figure 3.7). To identify the exact geometry needed to calculate the anisotropy tensors, we averaged the directions obtained from the differences of antipodal ARM directions (i.e., inversed polarity of DC field) for more than 100 samples. Using the differences eliminates the contribution of pre-existing remanent magnetic moments whose switching fields are higher than the highest peak field. Taking the *Fisher* (1953) mean for each of the six directions averages out directional deviations due to sample anisotropy, etc.

3.2.5. Computer Control and Data Processing

A personal computer with a Linux-based operating system runs the system via a custom-made graphical user interface; software is written in the Python programming language that communicates through standard hardware interfaces. The magnetometer connects to a RS-232 port, the motors are hooked in series to a RS-485 bus, and the real-time system controls the coil. Routines developed for
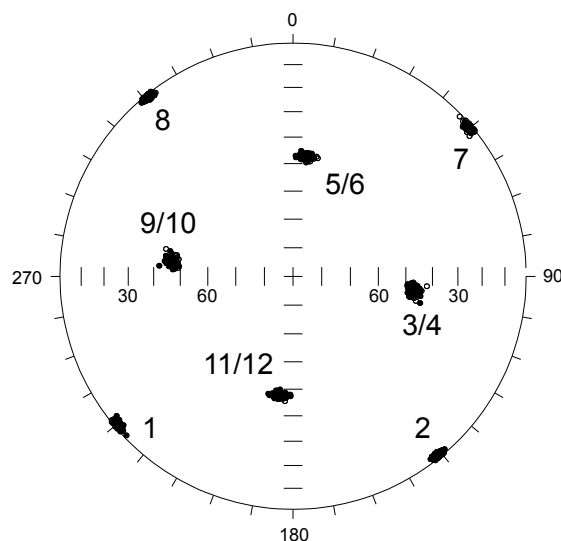
Figure 3.7.: Stereonet plot of 12 ARM directions (6 positions x 2 DC polarities) from 95 samples acquired in a AF window of 80-40 mT with a 0.1 mT bias field. Open circles are directions in the upper hemisphere, solid circles in the lower hemisphere. Numbers refer to the sequence in which the measurements were made.

the CryoMag program interface with the magnetometer (*Wack*, 2010). Firmware routines downloaded either to controllers integrated in the stepper motors or to the real-time system ensure precise coordination in the time domain. Control software allows users to select the measurement procedure (AF demagnetization, anisotropy of ARM, etc.) and related parameters (AF steps, ARM acquisition directions, etc.) for predefined specimens. Once a measurement sequence is running, an extensive event log is generated that can be viewed in real time either locally or remotely by a web browser and is e-mailed to the user upon completion. This helps identify potential problems, for example, if an operator forgot to put a sample cup on the track. In this case the system fails to find the reflective mark on the sample cup, outputs a warning message and repeats the process. If it fails again, an error message is written and the next specimen is processed. Additional checks of motor steps and operation time for certain operations ensure the detection of most problems.

Control software manages the system operation by issuing high-level commands to the different hardware modules, which in turn oversee low-level tasks such as turning the track to a specified specimen or overseeing the AF waveform of the

coil. To optimize the operation time, the program execution splits into a hierarchy of threads if needed. Figure 3.8 shows a typical flowchart of operations during stepwise three- component AF demagnetization and three-orientation measurement of the magnetic moment for one rotation of the track. By separating into individually controlled functions, we can readily integrate future instruments and limit unnecessary programming.

Field orientation parameters and other specimen meta-data (sampling location, bedding, sampling sites, stratigraphic level, etc.) are stored together with the acquired data in a relational database based on the MySQL engine (http://www.mysql.com/) (e.g., *Widenius et al.*, 2002) that are accessed by the SQLAlchemy module (http://www.sqlalchemy.org/) (e.g., *Copeland*, 2008). The structure subdivides the data into projects following a logic of typical paleomagnetic sampling schemes based on sites with individual samples. For magnetic measurements, the computer stores raw values of the three magnetic moments (one for each axis of the magnetometer) as well as the time, the sample alignment, and the baseline reading (empty magnetometer) before and after. The storage of all raw values to the database prevents information loss so users can examine and reprocess the data at a future time.

Each vector is derived from the average of three discrete sample measurements after accounting for the baseline reading and the contributions from the cup and sample handler. Averaging is performed by a custom-made data management software based on the Python language. Due to the multi-user, client-server architecture of the database system, this program can be run in parallel to the measurement process by several users simultaneously. Specific groups of measurements can be selected by defining any combination of sample, site, measurement type or measurement run. Conversion to geographic and bedding-corrected coordinates using field data is also implemented as well as the possibility to export data to various file formats for further analysis.
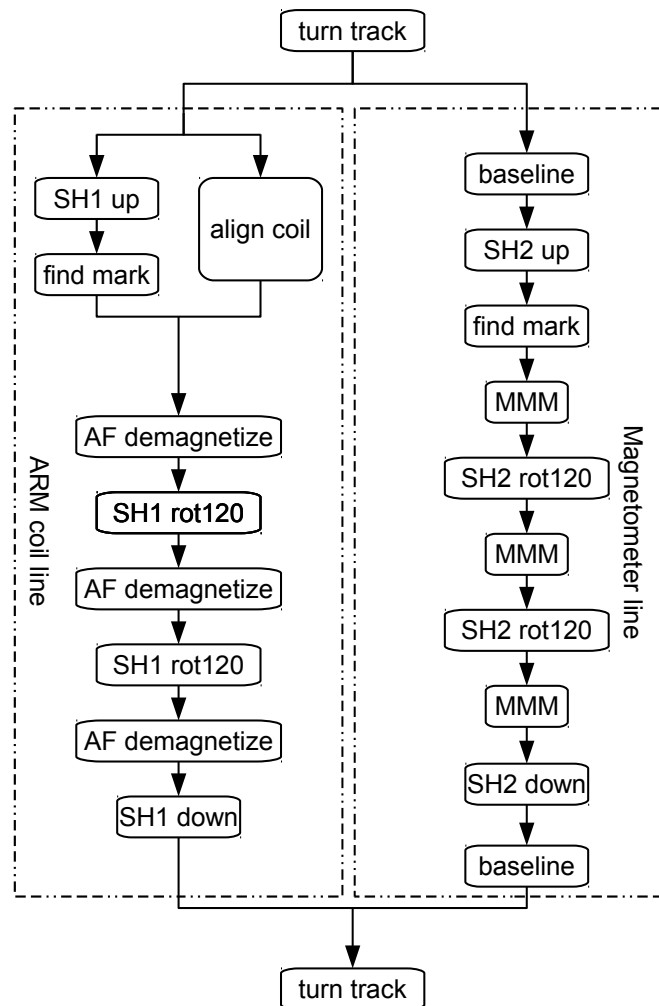
Figure 3.8.: Flowchart illustrating parallel operation of the hardware modules during stepwise AF demagnetization. SH1: sample handler for coil system, SH2: sample handler for magnetometer, baseline: measurement with magnetometer empty, MMM: measure magnetic moment, rot120: rotate sample 120° with the sample handler.

3.3. Conclusions

The SushiBar facilitates a wide range of automated paleo- and rock magnetic experiments on 99 samples at a time. Loading and unloading samples is fast ($\approx$15 minutes) and simple. Sample alignment in three orthogonal positions is precise to $\approx$1°, as ensured by laser probe switches and accurate stepper motors. A custom-made, tiltable coil system allows users to study the acquisition of an anhysteretic remanent magnetization (ARM) in any switching field range up to 95 mT peak AC fields and 0.17 mT peak DC fields in any direction. Hence, users can explore a wide range of parameters that includes the anisotropy of ARM.

Since routine operation began in March 2011, the SushiBar has made $> 100,000$ automatic sample manipulations and readings from the magnetometer, saving > 1000 hours of human working time. Future plans are to reduce the influence of parasitic magnetizations from the sample cups and the sample handler, and to extend the system with workstations designed for experiments based on susceptibility, isothermal remanent magnetization and high field ($\approx$500 mT peak AC field and 30 mT peak DC field) AF/ARM.

4. Case Study 1: Xishuigou Section[1]

To demonstrate the capabilities of our system as well as to examine the quality and limitations of the results, we studied samples from the Xishuigou magnetostratigraphic section (Subei, Gansu Province, China) previously reported in *Gilder et al.* (2001). Samples from this section, which is composed of Oligo-Miocene continental sediments, were specifically chosen because a number of rock magnetic parameters, including anisotropy of magnetic susceptibility, ARM moments, etc., vary fairly systematically from bottom to top of the section. The relative proportion of magnetite to hematite increases toward the top, which makes this section an interesting test case. Below we describe the measurement procedures carried out with the SushiBar and discuss the results.

4.1. AF Demagnetization of an ARM

AF demagnetization randomizes the magnetic moments of grains whose switching fields are equal to or less than the applied peak field. An anhysteretic remanent magnetization (ARM) is acquired when exposing a sample to a decaying alternating field (typically with peak fields about 100 mT) superimposed by a weak DC bias field (typically about 0.1 mT) (*Jaep*, 1969; *Egli and Lowrie*, 2002). The magnetic moments of grains whose switching fields are equal to or less than the applied peak field will be preferentially oriented in the direction of the bias field.

To demonstrate the linearity of the AF demagnetization trajectories with the SushiBar, we imparted ARMs (DC bias field 0.1 mT, AC peak field 90 mT) along

---

[1]Published as part of: Wack, M.R. and Gilder, S.A., The SushiBar: An automated system for paleomagnetic investigations, Geochemistry Geophysics Geosystems, in press.

a direction corresponding to $D \approx 0°$, $I \approx -45°$ in sample coordinates, and then stepwise AF demagnetized the ARMs in 5 mT steps in three orthogonal directions. Figure 4.1 shows the demagnetization data in an orthogonal component plot (*Zijderveld*, 1967). One observes linear and parallel demagnetization paths towards endpoints close to the origin as expected from a single magnetization component. Offsets from the origin are due to hard magnetic components (presumably from hematite) that were neither reoriented nor removed by peak fields of 90 mT. The *Fisher* (1953) average of the best fit line segments (*Kirschvink*, 1980) not forced to the origin lies at $D = 0.4°$, $I = -43.6°$, with a half-angle of the cone of confidence that the true mean direction lies within 95% confidence (α_{95}) of 1.2° (figure 4.1).
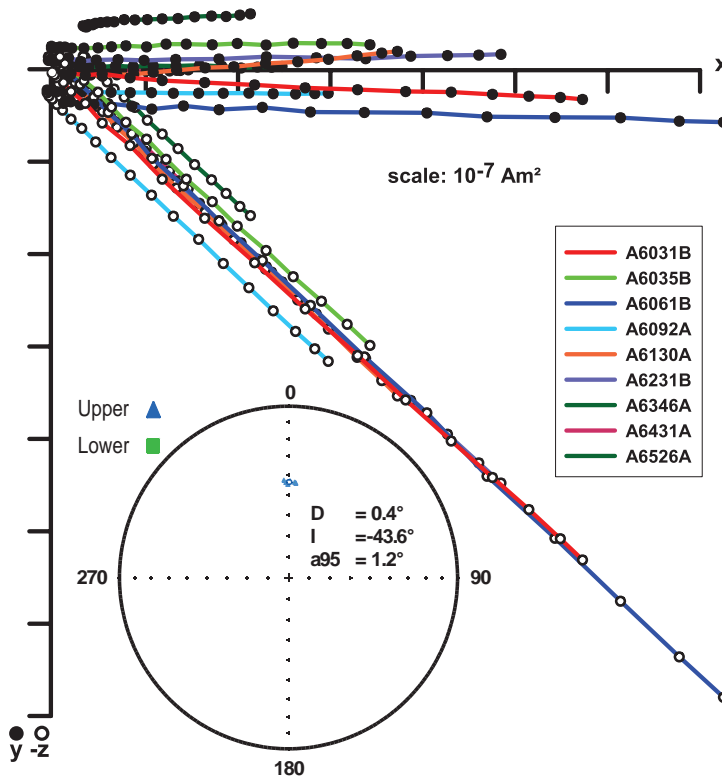
Figure 4.1.: Three component, AF demagnetization (5 mT steps) of an ARM (0.1 mT DC, 90 mT AC) imparted along direction $D \approx 0°$, $I \approx -45°$ for nine sedimentary rock samples in core coordinates. Offsets are caused by hard components of magnetization which were not reoriented by the ARM procedure. Best fit lines not forced to the origin for all samples and their Fisher mean are shown on the stereonet. Slight offset from expected is accounted for in subsequent ARM experiments.

The mismatch between observed and expected directions stems from the coil alignment, which is accounted for in subsequent directional ARM experiments.

4.2. Partial ARM (pARM) Spectra

A partial ARM (pARM) is generated by switching on the DC bias field within a specific range of the decaying AC field, which preferentially aligns magnetic grains whose switching fields lie within the discrete range (*Jackson et al.*, 1988; *Nakamura*, 2001). Coercivity of remanence (B_{cr}) is controlled by the switching field distribution following a power law function of grain size (d) according to $B_{cr} = d^{-m}$. The power index m is only constant for certain ranges of grain sizes and dependent on domain-wall area and dislocation ordering (*Day et al.*, 1977). Hence, ARM spectra, also known as switching field distributions, can be used to estimate grain size distributions in rocks. In addition, applying an ARM in a specific switching field range allows one to study the anisotropy or viscosity of specific grain sizes (*Jackson et al.*, 1988).

We measured the ARM spectra for nine samples in two ways. First (figure 4.2a), we followed a commonly used approach by taking the first derivative of the AF demagnetization of the ARM shown in figure 4.1. Second (figure 4.2b), we measured the pARM acquisition directly in 5 mT coercivity ranges. The profiles are similar, yet the maximum intensities of the pARM method lie at systematically lower switching fields than those obtained with the derivative method. This results from the fact that demagnetizing in three orthogonal directions is more effective in removing the ARM then when imparting it in only one direction with the same AC field amplitude (*Nørgaard Madsen*, 2004).

To quantify the field lag, we calculated the sum of the squared differences of both methods depending on the scaling factor for the AC peak field of the derivative method (figure 4.2c). The conformity between the two methods maximizes with scaling factors from 1.15 to 1.50 for the individual curves and an average of 1.4 for all curves (minima positions in figure 4.2c). We do not observe heightened scatter
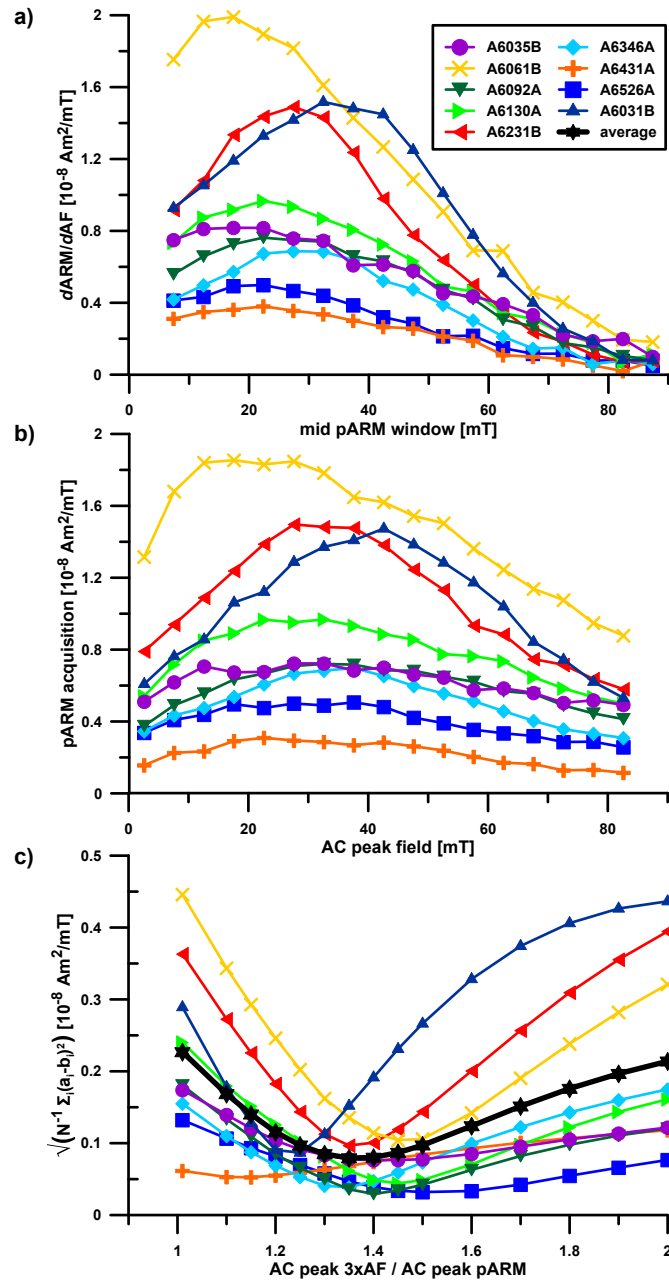
Figure 4.2.: ARM spectra of nine selected samples from Xishuigou section.
a) First deriviative of three component AF demagnetization in 5 mT steps.
b) pARM acquisition in shifted 5 mT AF windows. c) Sum of the squared differences between a) and b) depending on the ratio of AC field scaling. ARM and pARMs were produced with a DC bias field of 0.1 mT.

for the derivative method as in *Jackson et al.* (1988), which we attribute to the high precision of the SushiBar.

From a suite of experiments (IRM and ARM acquisition, stepwise demagnetization, etc.) on the Xishuigou samples, *Gilder et al.* (2001) concluded that magnetite and hematite carry the magnetic remanence, with the proportion of magnetite increasing up section. From a plot of the ARM moment (100 mT peak AF, 0.1 mT bias DC field) divided by the bulk susceptibility (X) versus X_{ARM} (*King et al.*, 1982, 1983), they found that the average grain size remains constant throughout the section, yet the amount of magnetic material increases up section. To further test this, we measured the pARM spectra in 5 mT windows for 96 samples from the Xishuigou section (figure 4.3). ARM acquisition at AF fields below 85 mT will be
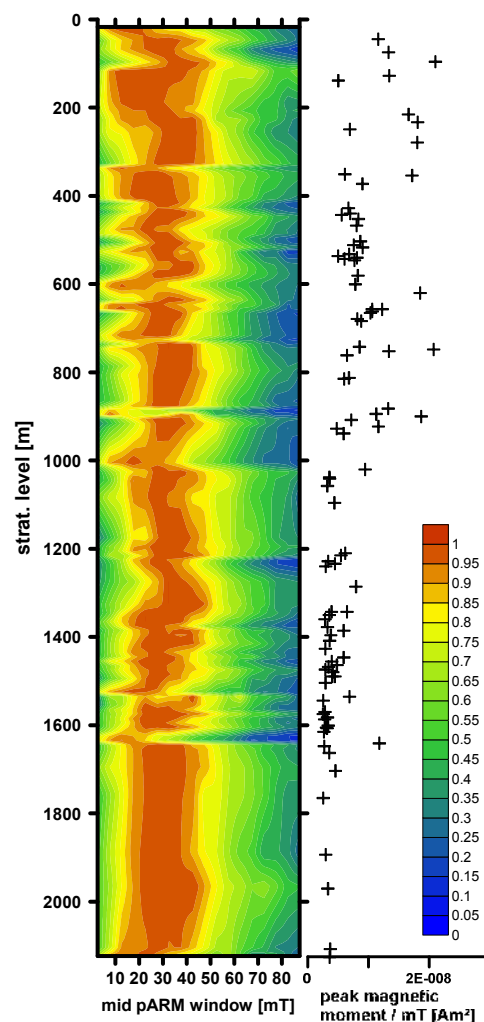
Figure 4.3.: Contoured pARM spectra of 95 samples from the Xishuigou section as a function of depth. Each spectrum is normalized to its peak value (shown on right). pARM acquisition was measured in discrete windows of 5 mT width. Three component AF (90 mT) demagnetized magnetic moment was vectorially subtracted for each sample.

predominantly controlled by magnetite (*McCabe et al.*, 1985). Normalized pARM spectra show a fairly consistent behavior of all samples with a peak position around 30 mT, which corresponds to a grain size of 2-3 μm for magnetite (*Jackson et al.*, 1988) that falls into the pseudo single domain range (*Day et al.*, 1977; *Moskowitz*, 1980). Peak pARM moments used for normalization of the spectra increase towards the top of the section, consistent with ARM intensities in *Gilder et al.* (2001) (figure 4.3).

To verify the additivity of the pARMs (*Patton and Fitch*, 1962), figure 4.4 compares the sum of 18 individual pARMs (5 mT windows) against the total ARM acquired in the range from 90 to 0 mT for each of the 96 samples. The measurements for most samples agree to within 20%. *Yu et al.* (2002) checked the additivity of five pARM intervals in the range from 100 to 0 mT for synthetic and natural samples using a similar procedure. They obtained an agreement of 3%, however this low amount of scatter can be attributed to their strict sample selection criteria (96% rejected) and to the lower number (5 versus 18) of individual coercivity windows, since systematic errors will add proportionally to the number of measurements. On average, the summed magnetic moments are slightly lower than the moment of the total ARM. We attribute this to a progressive demagnetization of grains outside the pARM window with each pARM procedure.
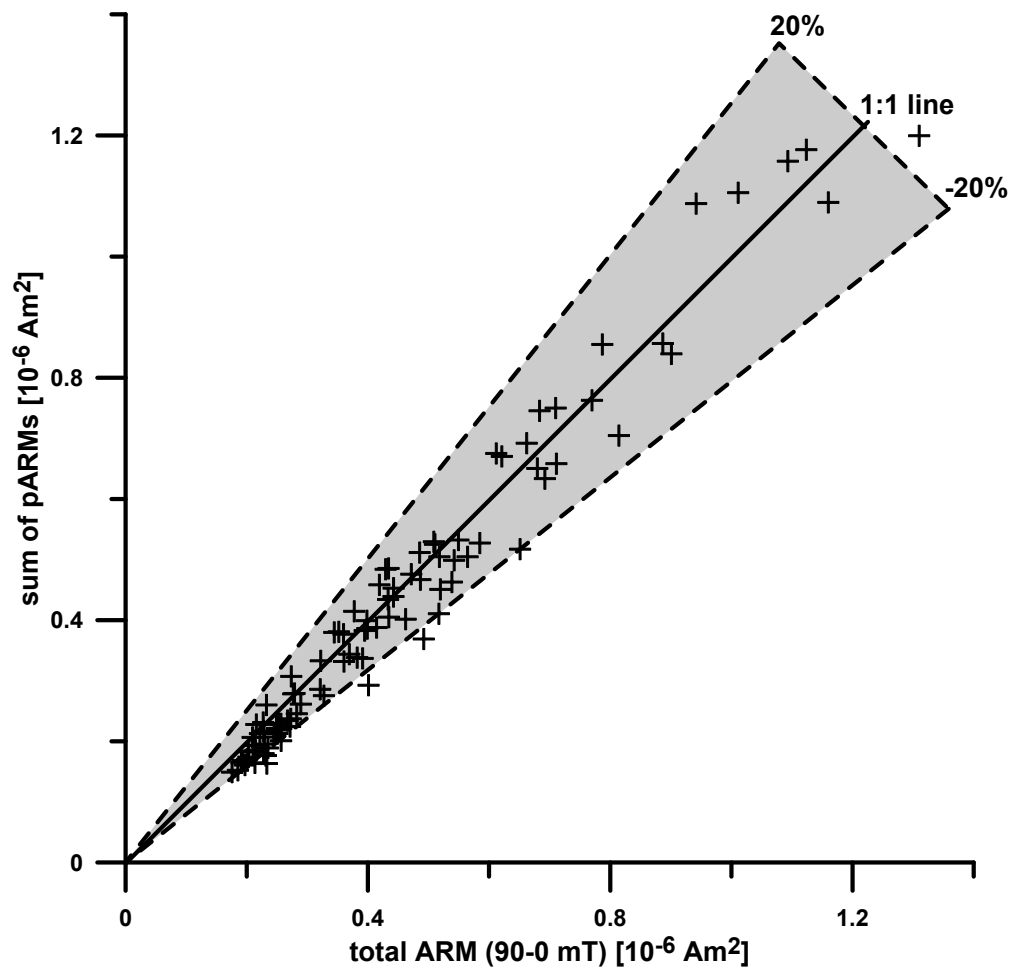
Figure 4.4.: Sum of pARM acquisition in 5 mT windows plotted against total ARM (90-0 mT) for 95 samples. DC bias field 0.1 mT.

4.3. Viscous Decay of ARM

Magnetic viscosity describes the temporal and directional response of a magnetization to an external magnetic field. The effect can be seen on long time scales as a present day field overprint in paleomagnetic data (*Biquand*, 1979), but it can also be observed over laboratory time scales. Viscous decay of an artificial remanence (e.g., an ARM) can impact the results if the relative timing between acquisition and measurement is not considered. This is a significant advantage of the SushiBar, which precisely controls this difference.

Thermal fluctuations are likely the primary source of magnetic viscosity in rocks (*Moskowitz*, 1985), although vacancy diffusion (*Kelso and Banerjee*, 1994), eddy currents (*Street and Woolley*, 1949) and trans-domain effects (*Moon and Merrill*, 1986) may also contribute. These effects cause either a switching of easy axes in single domain grains or domain wall jumping in multidomain particles. Magnetic viscosity can be controlled by the ordering of atoms within each grain and by the distribution of ferromagnetic grains within the rock matrix (*Afremov et al.*, 2009). Experimental observations show that in many cases, the change in magnetization can be described as a logarithmic decay (*Street and Woolley*, 1949; *Biquand*, 1979; *Kelso and Banerjee*, 1994; *Muxworthy and Williams*, 2006). This disagrees with an exponential decay predicted by *Néel* (1955) theory, which can be explained by overlapping signals from a range of grain sizes and shapes in a rock (*Gaunt*, 1986; *Dunlop and Argyle*, 1997) and by magnetic interaction (*Stacey*, 1963).

To investigate the viscous decay of ARM, we defined an absolute viscosity coefficient (S_A) as the decay of the acquired magnetic moment as $M(t) = M_i - S_A \cdot \ln(t)$, where t is in minutes and M_i is the initial magnetic moment. To avoid a contribution to S_A by unaffected hard components, we vectorially subtracted the magnetic moment measured after a three-axis AF demagnetization from the ARM moment. After doing so, S_A can be calculated from the slope (negative value) using a least-squares approach. For better comparison, figure 4.5 shows a normalized (to inital pARM moment) magnetic moment versus $\ln(t)$ plot of nine samples from the Xishuigou section, where a normalized viscosity (S_N) value $[M_{norm}(t) = 1 - S_N \cdot \ln(t)]$ of 0.01 describes a decay of $0.01 \cdot \ln(10) = 2.3\%$ within

the first 10 minutes. The precise starting time is poorly defined because the time difference between ramp down of the AC field and the acquisition of the ARM may differ for each switching field window. We thus ignore the first data point at $t = 2$ minutes and begin fitting at $t = 4$ minutes. The nine samples in figure 4.5 exhibit logarithmic decay, which indicates a single S value can be fit to the data. On longer timescales (several hours and more), non-logarithmic decay or changes in the viscosity coefficient have been observed (*Urrutia-Fucugauchi*, 1981; *Yu and Tauxe*, 2006). Figure 4.5 shows how differences in magnetic viscosity can introduce error in ARM measurements – especially for anisotropy of ARM where the ARM acquisition must be repeated several times and is sensitive to differences of only a few percent. Again we emphasize the utility of the SushiBar to carry out operations in a systematic way (precise and constant timing between acquisition and measurement), which are largely ignored when performing ARM experiments manually.
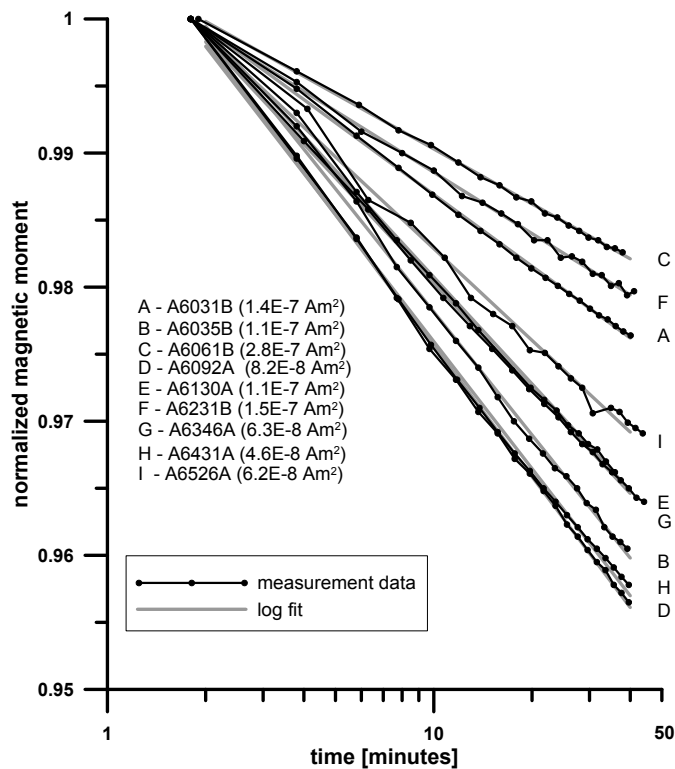
Figure 4.5.: Viscous decay of acquired pARM (AC window 20-0 mT. DC 0.1 mT) imparted at $t \approx 0$ minutes. Gray lines are fitted using least squares approach ignoring the first point at $t = 2$ minutes. Values in brackets are magnetic moments at $t = 2$ minutes used for normalization.

We studied the magnetic viscosity of 96 samples from the Xishuigou section by imparting an ARM (0.1 mT DC bias field) and then measuring the magnetic moment 20 times in two-minute intervals. We also investigated how magnetic viscosity varies as a function of the switching field distribution, so the procedure was performed automatically three separate times in switching field windows of 20-0 mT, 90-70 mT and 90-0 mT (figure 4.6). Absolute viscosity coefficients of the rocks are an order of magnitude greater than those of the plastic cups, so the contributions from the latter were ignored. Magnetizations acquired at lower switching fields (20-0 mT) have comparable absolute viscosities as those from 90 to 0 mT, while those measured within 90-70 mT switching fields have significantly lower values (figure 4.6a). It makes sense that the lowest coercivity fraction has the highest viscosity and that the highest viscosity fraction (20-0 mT) contributes the most to the total signal (90-0 mT). It is also logical that viscous decay correlates positively with amount of material (pARM moment); if samples contain equal proportions of viscous material, those with greater amounts of magnetic material will have higher absolute viscosity coefficients.

Figures 4.6b and 4.6c plot the pARM moments and absolute viscous decay coefficients of the three switching field fractions as a function of depth for the Xishuigou section. Not only do pARM moments and absolute viscous decay coefficients for 90-0 and 20-0 mT increase toward the top as expected, but unexpectedly, so too do those of the highest coercivity fraction (90-70 mT). The latter was independently confirmed in that magnetic moments remaining after 90 mT peak field AF demagnetization increase from the bottom toward the top of the section. This suggests that, while the magnetite to hematite ratio increases up section, the absolute amount of hematite also increases. Explaining the trend with a higher proportion of single domain magnetite goes against the pARM spectra, which argue for a constant magnetite grain size. Those same spectra cannot penetrate the switching windows needed to explore the hematite realm due to its much higher coercivity. Of interest is a plot of the normalized viscous decay coefficient (S_N) versus depth (figure 4.6d), where the trend goes in the opposite direction – an increase toward the bottom. This shows that not all grains within a given switching field window contribute equally to the magnetic viscosity, but rather that the
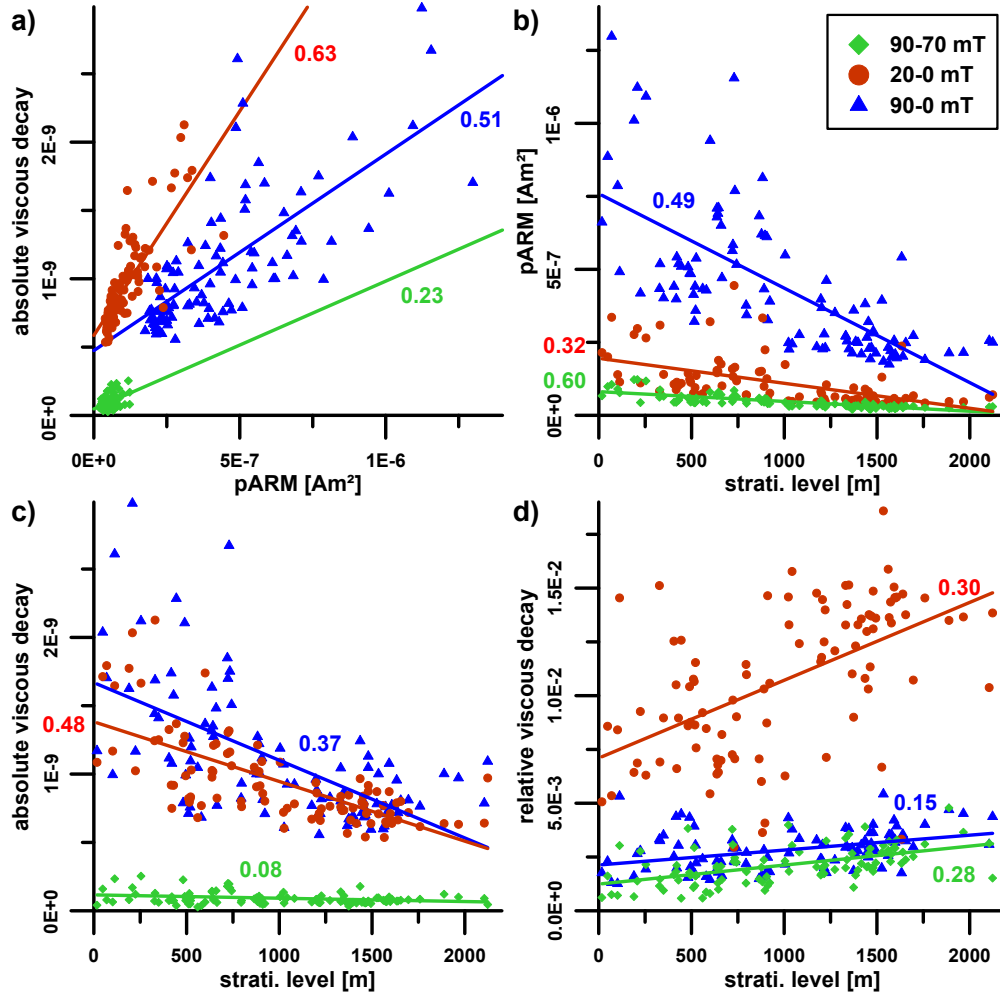
Figure 4.6.: Dependence of viscous decay on pARM window. pARMs imparted in a high switching field window $(90 - 70 \text{ mT})$ show lower viscosities than pARMs in lower switching field range $(20\text{-}0 \text{ mT})$. Colored numbers are correlation coefficients (R^2) of adjacent fits. a) Absolute viscosity coefficients S_A are plotted against the initial pARM moments. b) Initial pARM moments decrease from top to bottom of the section in all pARM windows. c) Absolute viscosity coefficients S_A decrease from top to bottom of the section in all pARM windows. d) Relative viscosity coefficients S_N increase from top to bottom for all pARM windows.

proportion of non-viscous material contributing to each pARM window is greater at the top of the section. Somehow it seems counterintuitive that the top of the section has the highest proportion of both viscous and non-viscous material, and highlights the fact that ARM magnetic viscosity coefficients need to be interpreted with caution (e.g., samples with high magnetic viscosities can have highly stable magnetic remanences).

4.4. Anisotropy of pARM

Anisotropy describes a directional dependence of a property. The anisotropy of mineral grains within rocks often reflect structural information created during their formation or subsequent deformation (i.e., paleo-flow directions, stress directions, etc.) (*Martin-Hernández et al.*, 2004). Magnetic anisotropy in rocks is controlled by the crystalline anisotropy (predominantly in hematite or paramagnetic minerals), by the grain shapes and by the arrangement of individual grains (*Tarling and Hrouda*, 1993). Magnetic methods provide one of the fastest and most accurate ways to quantify the anisotropy of a mineral fabric in a rock.

Anisotropy of magnetic susceptibility (AMS) is by far the most common technique to study rock fabrics – largely because sensitive kappabridge susceptibility meters are commercially available (AGICO Inc.). Measuring AMS fabrics on standard paleomagnetic cores takes ca. 20 minutes with older versions (KLY-2) of the AGICO kappabridge and ca. 6 minutes with the more modern versions. Both older and newer versions require constant operator attention (although much less with the newer version). All grains contribute to the bulk susceptibility of a rock, including para- and diamagnetic minerals, and especially magnetite, which has a thousand times higher susceptibility than most common minerals. Because paleomagnetic studies focus primarily on understanding the remanence carrying grains, and because the mass of magnetite in rocks is often dominated by multidomain magnetite, AMS fabrics are biased toward the non-remanence-bearing fraction.

A remanence-based method must be used to study the anisotropy of the remanence carrying grains. Of the available methods, the anisotropy of ARM (AARM) allows one to study the magnetic fabrics of the remanence carrying grains in any particular switching field window; e.g., to focus on the anisotropy of individual grain size fractions based on their magnetic coercivity. For a linear relationship between the applied field (B) and the resulting magnetic moment (M), the anisotropy can be described by a second-rank symmetric tensor $[k]$, where $M = [k] \cdot B$ (*Girdler*, 1961; *Hext*, 1963; *Coe*, 1966). To determine the tensor, we apply a six-orientation, dual-polarity protocol (directions #1 to #12) based on the measurement scheme of *Owens* (2000). Specimens are first demagnetized in three orthogonal directions with a peak AF field of 95 mT, and then a pARM is imparted in direction #12. The pARM in direction #12 is AF demagnetized, then a pARM is imparted in direction #1 and then the remanence is measured. Subsequently, specimens are AF demagnetized along the previous pARM direction and a new pARM is imparted along the next direction (#2 to #12) and then the remanence measured.

This protocol avoids bias from any single measurement direction – it yields 36 values (12 measurements times 3 components) that are converted to an anisotropy tensor $[k]$. The latter are determined by first taking half the difference of the measured vectors from antipodal ARM directions. This results in $6 \cdot 3 = 18$ components and averages out unaffected hard components. We then use a least squares approach based on the design matrix reflecting our measurement geometry to find the best fitting tensor of the data. The tensor is then diagonalized to obtain the eigenvalues and eigenvectors that describe the magnitude and direction of the principal axes of the anisotropy ellipsoid. The routine also calculates the standard deviation of the measurement data to the expected values.

Figure 4.7 demonstrates the reproducibility of the eigenvalues to within 3% (mostly $< 2\%$), independent of the degree of anisotropy, for 27 samples whose AARMs were measured twice. Moreover, the SushiBar's rigorous temporal control between ARM acquisition and measurement eliminates viscous effects to the AARM tensor. It is instructive to quantify the potential effect of magnetic viscosity on manual measurements. Typically observed relative viscosities in our study are $\approx 1\%$ in the 20-0 mT range. Varying the time between ARM acquisition and measurement
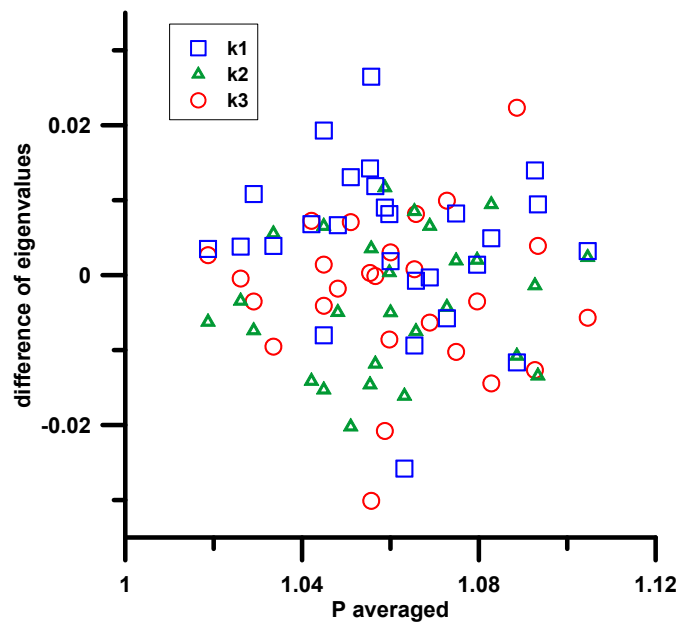
Figure 4.7.: Differences of eigenvalues for repeat AARM measurements on 27 sedimentary rock samples. 23 of 27 samples show differences of less than 2% irrespective of the anisotropy degree (P).

by 30 minutes for two steps would introduce a difference of $1\% \cdot \ln(30) = 3.4\%$ among the two measurements, which translates into a 'false' degree of anisotropy of 3.4%.

We now return to the samples from the Xishuigou section, where the AMS fabrics were found to vary with stratigraphic height (*Gilder et al.*, 2001). In stratigraphic coordinates, maximum principal axes ($k1$) lie in the horizontal plane, parallel to the fold axis direction. Minimum principal axes ($k3$) inclinations deviate from vertical at the top of the section toward the horizontal near the bottom of the section. Intermediate principal axes ($k2$) mimic the $k3$ directions in the opposite sense, going from horizontal inclinations at the top toward vertical at the bottom. Both the deviation in $k2$ and $k3$ directions follow a great circle path normal to the $k1$ directions. *Gilder et al.* (2001) interpreted the AMS directions to reflect a predominately sedimentary fabric at the top of the section that became progressively superimposed with a tectonic fabric. Of further interest is that the degree of anisotropy (P) remains constant throughout the section at 4%, while the shape of the anisotropy ellipsoid is variable but triaxial on average in the lower

three-fourths of the section, whereas distinctly oblate shapes dominate the upper fourth.

We measured the AARM of 95 samples from the Xishuigou section, the same ones previously measured for AMS, three times in three discrete switching fields: 20-0, 40-20 and 80-40 mT. The latter are distinguished below as AARM20-0, AARM40-20, and AARM80-40, respectively. No correction for the sample cups was necessary since the ARM moments acquired by the specimens are two orders of magnitude greater than for the cups. We plotted the eigenvalues from the ARM tensors for the three switching field ranges against the eigenvalues of the AMS tensors (figure 4.8).
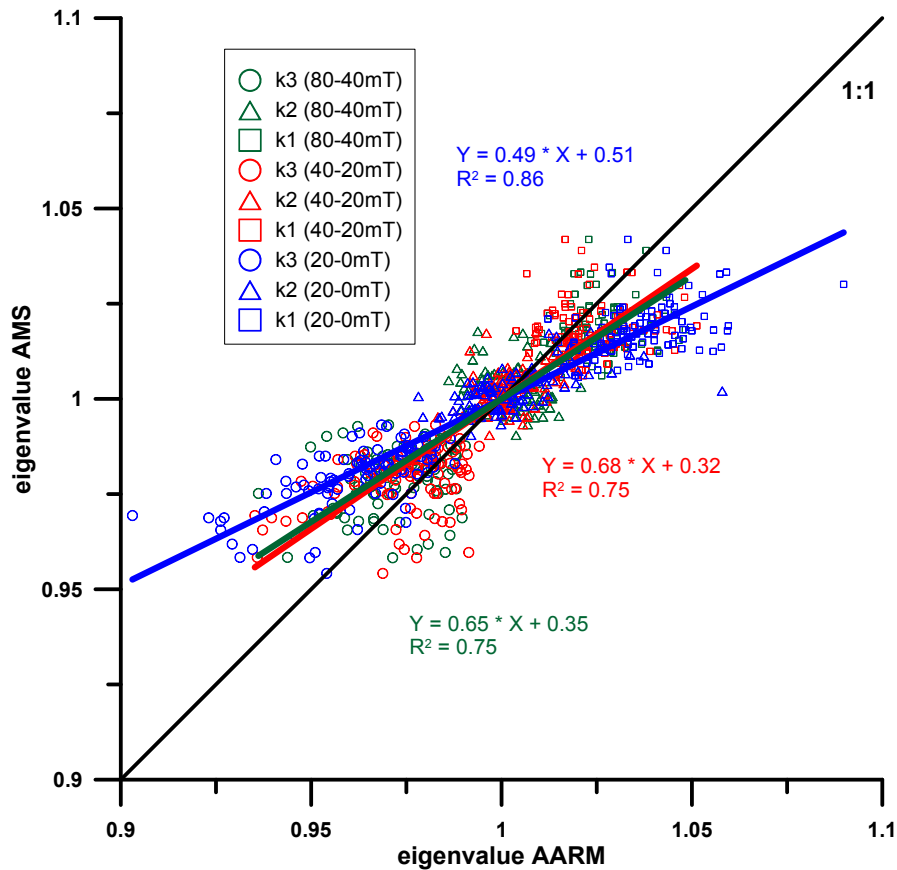
Figure 4.8.: Normalized eigenvalues of AMS plotted against normalized eigenvalues of AARM in three switching field ranges (80-40, 40-20, 20-0 mT). Slopes smaller than one indicate higher degrees of anisotropy for AARM compared to AMS values.

As expected theoretically (*Stephenson et al.*, 1986), we observe slopes smaller than unity, which indicates higher degrees of anisotropy for AARM than for AMS. This is because it is easier to induce a reversible magnetization along an unfavorable axis than to impart a remanent magnetization along the same axis (*Winkler and Sagnotti*, 1994).

We first compared the degree of anisotropy (P) and the shape parameter (T) among AMS and the three ARM switching field windows as a function of depth in the section (figure 4.9). Following *Jelinek* (1981), we normalized the $k1$, $k2$, and $k3$ eigenvalues so that they sum to three, and then express the degree of anisotropy as $P = k1/k3$ and the shape parameter as $T = (R-1)/(R+1)$ with $R = \ln(k2/k3)/\ln(k1/k2)$. Thus a P of 1.05 signifies 5% anisotropy and T ranges from -1 (prolate) to $+1$ (oblate) with 0 being neutral or triaxial. When divided into four stratigraphically equal parts, with 1/4 at the top and 4/4 at the bottom, one sees that P remains constant along the entire section, both with AMS and the
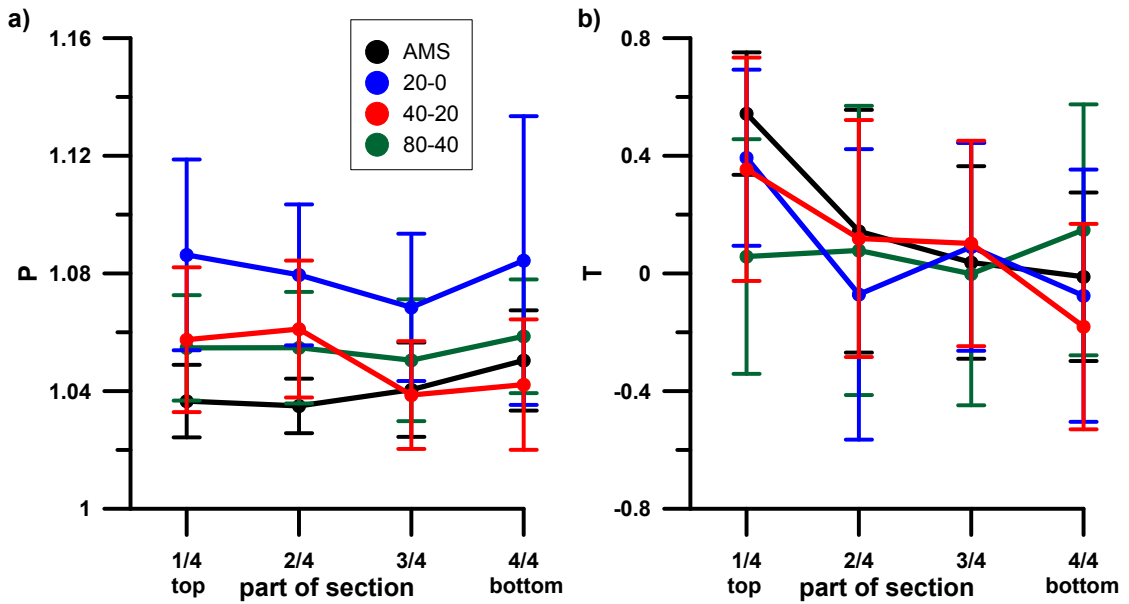
Figure 4.9.: Variation of the AMS and AARM anisotropy ellipsoids, the latter in three switching field windows (80-40, 40-20, 20-0 mT), as a function of stratigraphic height (averages shown for four approximately equally-thick parts of the Xishuigou section). Error bars indicate one standard deviation of the averaged data. a) Degree of anisotropy (P). b) Shape parameter (T). Prolate ellipsoids are characterized by negative values; oblate ellipsoids by positive values.

three different windows. *P* for AARM20-0 is twice that of AMS (8% versus 4%), while P for AARM40-20 and AARM80-40 are equivalent at 6%. For *T*, all AARM and AMS values are around 0 except for the top quarter of the section where AMS, AARM20-0 and AARM40-20 are oblate on average. An increasing proportion of a tectonic fabric on a sedimentary fabric can partially explain the trend from oblate to triaxial fabrics going down section (*Housen et al.*, 1993).

Figure 4.10 compares the principal anisotropy axis directions for AMS and three AARM windows in bedding-corrected coordinates as a function of depth. The mean values were calculated by averaging all normalized tensors in the same stereonet plot (*Jelinek*, 1978). Error estimates are shown in neighboring stereonets using a non-parametric bootstrap technique (*Constable and Tauxe*, 1990). AMS and AARM20-0 directions are quite similar, which should be expected as contributions to both AMS and AARM20-0 likely stem from similar multidomain magnetite fractions. This again highlights the functionality of the SushiBar. Interestingly, $k1$ and $k2$ directions are completely switched between AMS and AARM20-0 in the top quarter (1/4) of the section, and farther down, $k1$ and $k2$ directions for AARM20-0 distribute more along great circle swaths than for AMS, whose directional populations are more grouped. For AARM40-20, the $k1$ and $k2$ directions are switched relative to AMS for all four quarters of the section. The directions for AARM80-40 become much more scattered, but there is a tendency to invert the $k1$ and $k3$ directions, especially at the bottom half of the section. *Kodama and Dekkers* (2004) also observed switching of the $k1$ and $k2$ axes between AMS and AARM and attributed it to the contribution of the paramagnetic fraction to the AMS fabric.

Why the inversion occurs between $k1$ and $k2$, and then $k1$ and $k3$, principal axis directions is speculative; however, it partially owes its origin to hematite, and perhaps pseudo single domain magnetite, contributing a greater proportion to AARM than to AMS, especially at higher switching fields. AARM being more sensitive to the hematite fraction than AMS is logical considering magnetite's susceptibility is 1000 times greater than hematite whereas its saturation magnetization is 200-250 times greater, so when the two minerals are present, the relative contribution from hematite will be four to five times greater in remanence-based methods over susceptibility-based methods. Anisotropy experiments using strong
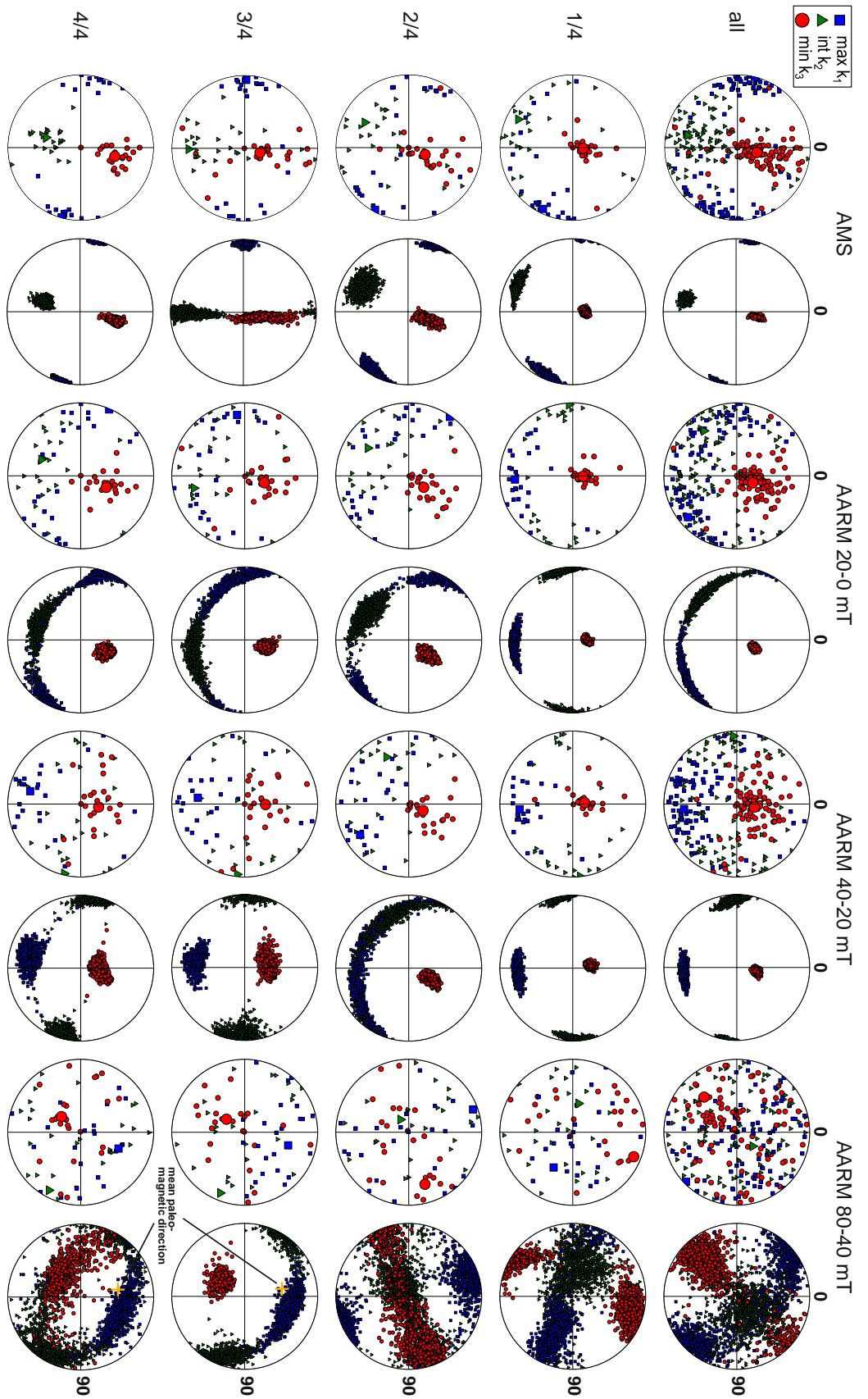
Figure 4.10.: Principal directions of AMS (data from Gilder et al., 2001) and AARM tensors (different pARM windows as labeled) of 95 samples from Xishuigou section in bedding corrected coordinates. Large symbols are averaged directions based on normalized mean tensors. All data are shown twice: original (left) and bootstrapped (right). North is up, east to the right.

magnetic fields could resolve this point. A tentative interpretation is that the AARM80-40 fabric begins to define the orientation of the remanence carrying grains, whose $k1$ axes should be aligned parallel to the paleo-field direction in sedimentary rocks (see figure 19 in *Jezek and Gilder* (2006)). Stepwise thermal demagnetization of the Xishuigou samples yielded an average tilt corrected direction of declination 350.2° and inclination of 43.8°, which lies within the swath of AARM80-40 $k1$ directions in the bottom half of the section where hematite/magnetite is more prevalent.

5. Case Study 2: Chon Kyzyl-Suu and Dzhety-Ogyuz sections[1]

We present paleomagnetic results from the northern flank of the Tianshan range, southeast of lake Issyk-Kul (Kyrgyzstan). 613 cores were collected in two parallel, Cenozoic sedimentary sections with a total thickness of 960 m (Chon Kyzyl-Suu) and 990 m (Dzhety-Ogyuz), as well as 48 cores at six sites at a nearby anticline. Stepwise thermal demagnetization isolates 289 samples with interpretable magnetization components that define 40 polarity chrons. A positive fold test on all sampled sites indicates that the high temperature magnetization component predates folding. Our preferred, albeit tentative, magnetostratigraphic correlation with the geomagnetic polarity time scale suggests absolute deposition ages range from 25.5 to 13.2 Ma, with a fairly constant sedimentation rate of 10 cm per ka. The ferromagnetic fabric, derived from the anisotropy of anhysteretic remanent magnetization (ARM) for both magnetostratigraphic sections, shows a well developed tectonic fabric with sub-horizontal maximum axis that parallel the strike directions, orthogonal to the local maximum strain direction. Based on comparison of sedimentation rates found at other magnetostratigraphic sections in the Tianshan realm, we infer that 13.2 Ma pre-dates the most active phase of uplift of the Kyrgyz Tianshan.

5.1. Introduction

The Tianshan is a nearly 2500 km long, east-west striking and lateral extending mountain range north of the Tarim basin and south of the Kazakhstan shield. It represents an old Paleozoic orogenic belt (*Mikolaichuk et al.*, 1997; *Burtman*, 2006) which was reactivated in the Cenozoic by the India-Asia continental collision which

---

[1]In preparation for publication: Wack, M.R., Gilder, S.A. et al., Cenozoic magnetostratigraphy and anisotropy of remanence from southern Issyk-Kul basin (Kyrgyzstan).

started about 50 Ma ago (*Molnar and Tapponnier*, 1975; *Patriat and Achache*, 1984). Most of the present topography with peaks up to 7000 m can be attributed to late Cenozoic tectonics (*Tapponnier and Molnar*, 1979; *Cobbold et al.*, 1993). The Tianshan is one of the most active intracontinental collision zones in the world and therefore provides an exceptional opportunity to study tectonic deformation, mountain building and associated sedimentation. Late Quaternary slip rates show that the deformation is continuously distributed across the central Tianshan (*Reigber et al.*, 2001; *Thompson et al.*, 2002), but an extrapolation of current shortening rates of ≈20 mm per year determined from GPS measurements (*Abdrakhmatov et al.*, 1996; *Zubovich et al.*, 2010) implies an unrealistic young onset of deformation about 10 Ma ago. Therefore an acceleration of deformation in the late Cenozoic is assumed (*Bullen et al.*, 2001; *Abdrakhmatov et al.*, 2001; *Sobel et al.*, 2006a; *Li et al.*, 2011). While the overall deformation pattern of reverse faults (*Abdrakhmatov et al.*, 2001) is widely accepted, the timing and style of local deformations is complex and not well understood. Many studies to constrain deformation patterns (*Thomas et al.*, 1993; *Avouac and Tapponnier*, 1993; *De Grave et al.*, 2007; *Buslov et al.*, 2003, 2007; *Sycheva et al.*, 2008) and uplift and erosion history (*Gilder et al.*, 2003; *Sobel et al.*, 2006b; *Huang et al.*, 2006; *Charreau et al.*, 2005, 2006, 2009a,b, 2011; *Sun et al.*, 2004, 2009; *Sun and Zhang*, 2009) have been done. To better understand Cenozoic tectonics we study fluvial-lacustrine sediments deposited in the south of the intermontane Issyk-Kul basin located in eastern Kyrgyzstan. Its strata is expected to be closely linked to the uplift of the source mountains (*Suppe et al.*, 1992; *Burbank et al.*, 1996). We performed rock magnetic experiments to constrain the magnetization carriers and to study sedimentary changes during deposition. We used characteristic paleomagnetic directions determined from high temperature stepwise demagnetization paths to study tectonic rotations and the anisotropy of anhysteretic remanence to constrain deformation and compaction of the sediments. We used additional sites at a near-by anticlinal structure to perform a fold test. We also analyzed the magnetostratigraphic records of two parallel sections to establish a correlation between them and to constrain sedimentation rates.

5.2. Sampling Locations and Methodology

We focus on two well exposed magnetostratigraphic sections in the northern Tianshan, south-east of Lake Issyk-Kul. The sections are located in two parallel valleys which cut approximately orthogonal through the roughly east-west striking sedimentary layers deposited in the Issyk-Kul basin. Section CK is located close to the village of Chon Kyzyl-Suu, section TJ near Dzhety-Ogyuz (figure 5.1). We sampled section TJ in 2009 and CK in 2010. At both sections, we observed similar sedimentary fabrics consisting of alternating layers of coarse, red sandstones and conglomerates of varying grain sizes (panoramic view of CK section in figure 5.1). We recognized a gradual decrease of red pigment towards the top of both sections. The same characteristics are described by *Cobbold et al.* (1996). We did not identify any major discontinuity or unconformity within the two sections, although some lateral valleys masked small parts of the stratigraphy. Our TJ section almost covers the entire Dzhety-Ogyuz formation as recorded by *Cobbold et al.* (1996). It is underlain by the Chonkurchak formation, which marks the basal portion of Tertiary sediments and is deposited on top of Jurrassic quartzites (*Cobbold et al.*, 1996). Strike directions and sedimentary fabric suggest a significant stratigraphic overlap of the two sections. The scarcity of fossils and the lack of volcanic horizons impose large age uncertainties and make magnetostratigraphy the best method to date and correlate both sections. Furthermore, a high-resolution record of sedimentation rates, which can be used to study the uplift and associated erosion history of the source mountain range, can be deduced from a successful magnetostratigraphic correlation. Regional geological maps show the top of the TJ section at Paleogene-Neogene boundary and CK extending further up into the Neogene (figure 5.1). Near the top of the Dzhety-Ogyuz formation remnants of a tortoise have been found and attributed to the Oligocene (*Sidorenko*, 1972). *Thomas et al.* (1993) sampled 12 sites at TJ (Dzhety-Ogyuz Formation) and derived paleomagnetic directions as well as the principal axis of anisotropy of magnetic susceptibility (AMS). To our knowledge there is no previous paleomagnetic study of the CK section.

We measured bedding orientation at all possible drilled bed. To average out measurement errors we use a linear interpolation of dip and dip direction along
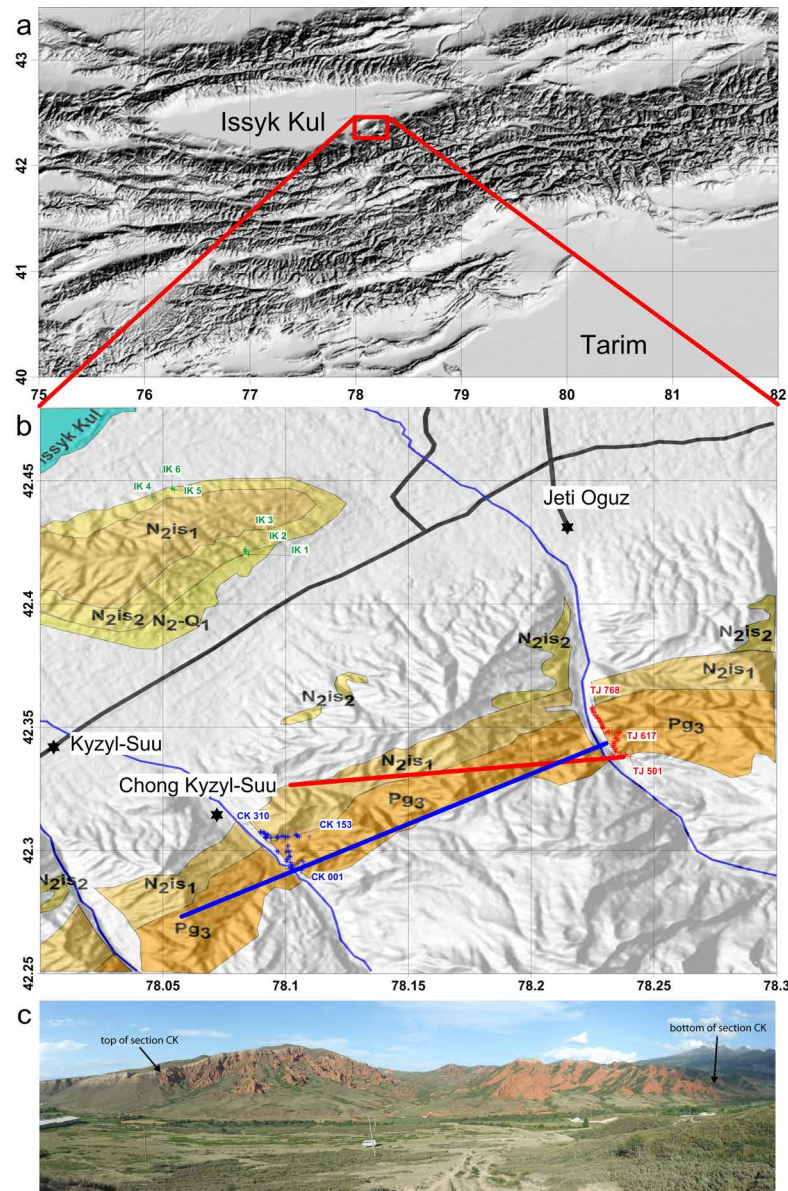
Figure 5.1.: (a) Topographic overview map of the Tianshan. (b) Cenozoic geologic map of sampling region south-east of lake Issyk Kul (Kyrgyzstan). TJ (red) and CK (blue) are continuous magnetostratigraphic sections. Position of every second core is shown. IK consists of 6 discrete sampling sites. Contours of geologic formations are transferred from regional geological map (sheet K-44-XIII). Pg3=Paleogene, N2=Neogene, Q1=Quaternary, is1(2)=lower (upper) Issyk-Kul formation. Thick red and blue straight lines represent averaged strike directions for CK and TJ section. (c) panoramic view of CK section (view direction towards east).

stratigraphic height for each section to convert from geographic to stratigraphic coordinates. Dip directions are rather constant (336° at the bottom to 341° at the top for CK and consistently 355° for TJ), dip angles change with stratigraphy in an opposing sense for both sections. CK steepens towards the top (27° at the bottom, 37° at the top), TJ flattens towards the top (41° at the bottom, 33° at the top). The latter is compatible with the observation of Cobbold et. al (1996). Stratigraphic depth was measured from the bottom of each section. When direct measurements were not feasible because the lateral distance between drilling sites was too large, we calculated the stratigraphic distance from bedding attitude and GPS locations. In CK (TJ) section we always drilled two cores from discrete, finest grained horizons with an average spacing of approximately six (seven) meters over a total thickness of 960 (990) meters.

To be able to perform a fold test, we sampled additionally three sites on each side of an anticlinal fold (IK1-6) ca. 14 km north of CK section and close to lake Issyk-Kul (figure 5.1). The sediments are lacustrine, fine grained, soft and light gray in color. At each site we obtained 8 cores spread over 3 to 9 meters of stratigraphic thickness. We measured dip angle and dip direction of the bedding at least three times at each site and use the averaged values. GPS coordinates, the number of cores obtained and average bedding orientations for all sites are listed in table 5.1.

Location	Latitude	Longitude	No of cores	average dip dir	average dip
IK1	42.42005	78.08577	8	141	36
IK2	42.42196	78.08338	8	174	62
IK3	42.42171	78.08358	8	131	35
IK4	42.44355	78.04549	8	330	47
IK5	42.44635	78.05453	8	354	53
IK6	42.44698	78.05385	8	335	54
CK001	42.29238	78.10874	332	338	32
CK310	42.30779	78.08986			
TJ501	42.33809	78.24040	281	355	37
TJ768	42.35828	78.22502			

Table 5.1.: List of sampling locations and their geographic coordinates (WGS84), number of obtained cores and averaged downward dip directions (360 = dipping downwards towards north) and dip angle (0 = horizontal, 90 = vertical)

We drilled inch cores (≈24 mm in diameter) using mostly handheld, water cooled, gas powered drilling machines. For soft sediments, especially at the IK sites, we drilled dry with a slowly rotating battery powered drill to avoid dissolution of the cores. All cores were oriented using magnetic and whenever possible sun compass measurements. We use the magnetic declination anomaly of 4.3° to correct strikes and core azimuths measured with the magnetic compass.

In the lab we cut the cores into 22 mm long specimens for further measurements. The deepest parts are referred as A-cores. If the length of the drill core permitted, we obtained a second equally sized specimen referred as B-core. We used every second A-core for thermal demagnetization studies and the B-cores for AF demagnetization and ARM acquisition experiments. Smaller samples for additional rock magnetic measurements were obtained from the remaining, deepest part of the drill core.

Thermal demagnetization was done with an ASC Scientific TD-48 oven (http://www.ascscientific.com) in approximately 20 steps up to temperatures of 685°C. We took care to place the samples at the same locations inside the oven and to alternate the orientation of the z-axis for each heating step to reduce the noise due to a systematic spatial temperature gradient and to reveal potential thermal remanent magnetization (TRM) acquisition. We used our recently developed automatic system, named the 'SushiBar' (*Wack and Gilder*, 2012) for measurements of magnetic moments, AF demagnetization up to 90 mT and ARM acquisition experiments for all inch cores. The 'SushiBar' facilitates automated processing of 99 inch cores. It is based on a commercial SQUID magnetometer and a custom made coil. The characteristic remanent magnetizations of the samples were determined with principal component analysis (*Kirschvink*, 1980) using the PMGSC 4.2 program written by Randolph J. Enkin. Inclination only statistics and pole calculations were done with the PaleoMac program (*Cogné*, 2003). We used a Variable Field Translation Balance (VFTB, Petersen Instruments, www.vftb.com) at our lab for additional rock magnetic experiments. To determine characteristic parameters from those measurements, we used the RockMagAnalyzer software (*Leonhardt*, 2006).

5.3. Results

5.3.1. Magnetic Mineralogy

To constrain the unblocking temperatures of the minerals present in the rock, we imparted an artificial TRM on six previously thermally demagnetized A-cores from TJ section by exposing the specimens to a controlled ambient magnetic field of 40 μT during cooling from 700°C to room temperature. The resulting magnetizations are $1.1 \pm 0.3 \cdot 10^{-6}$ Am^2. Subsequently, we exposed the specimens to the same 20 step thermal demagnetization procedure that was used to demagnetize the natural remanent magnetizations (NRM) of the specimens. Figure 5.2 clearly reveals two Curie temperatures. The magnetization drop at 680°C is very sharp and typical for hematite whereas the blocking spectra below 580°C is wider and typical for magnetite.
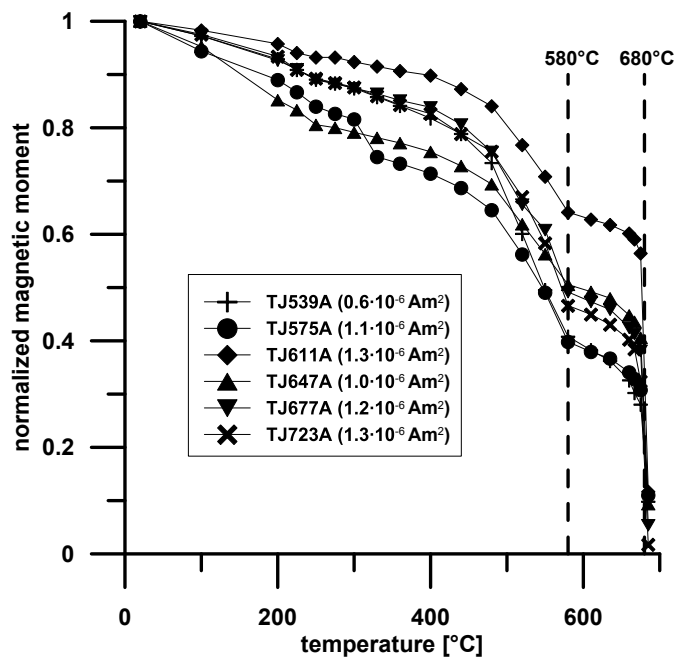
Figure 5.2.: Normalized magnetic moments of stepwise thermal demagnetization of artificial TRMs imparted to six samples from TJ section. Initial magnetic moments used for normalization are given in the legend.
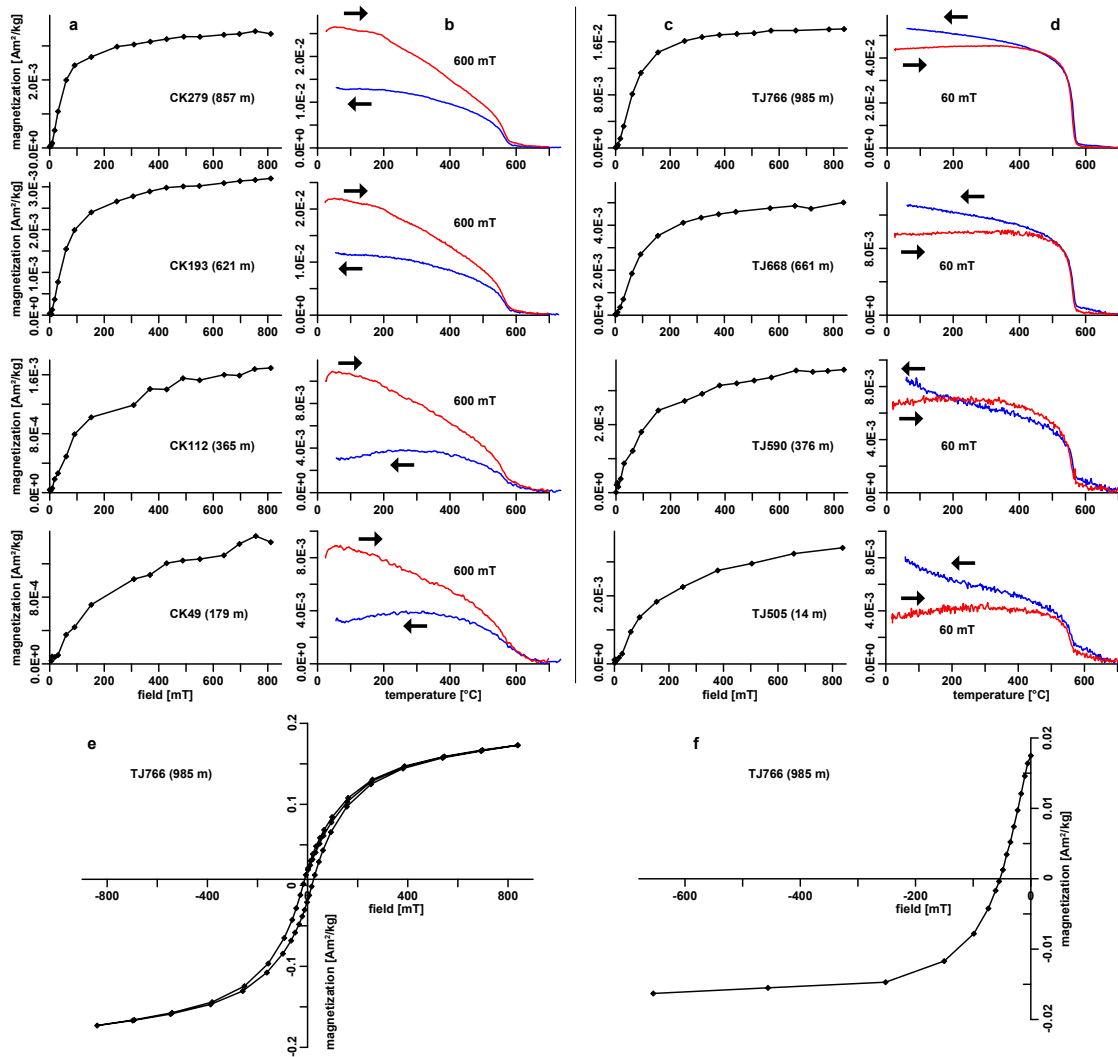
Figure 5.3.: Representative VFTB measurements of four samples from CK and TJ section. For each sample IRM acquisition (columns a and c) and thermomagnetic curve (columns b and d) are shown. Thermomagnetic curves are corrected for paramagnetic contributions and lag of the temperature sensor. Stratigrahic level is given in brackets following the sample name. e: hysteresis loop, f: backfield curve.

To characterize the carriers of the magnetic signal and to constrain changes of relevant parameters with stratigraphy, we measured thermomagnetic curves, hysteresis loops, isothermal remanent magnetization (IRM) acquisition and backfield curves on 21 specimens distributed along the TJ and CK section using the VFTB. IRM acquisition curves (figure 5.3a, c) rise quickly in fields below 150 mT, which indicates a low coercivity mineral, such as magnetite. Saturation is not reached

even at highest fields of 0.8 T. We attribute this to hematite, taking into account the well defined Curie temperature at 680°C and its known high coercivity. Samples towards the top of both sections show a stronger increase of IRM with applied field, which is explained by an upward increasing magnetite to hematite ratio. Thermomagnetic curves were measured within an applied field of 600 mT for CK samples and 60 mT for TJ samples. We attribute the systematic lower cooling curves for CK to the intense magnetic field that magnetizes a phase with high coercivities, which transforms to a less magnetic phase with increasing temperature. Thermomagnetic curves (figure 5.3b, d) show a sharp drop of magnetization around 580°C, characteristic for magnetite, and a minor component persisting to even higher temperatures (likely hematite). We used hysteresis loops (figure 5.3e) to determine coercivity B_c, saturation remanence M_{rs} (i.e. magnetization left after exposing the sample to maximum field) and backfield curves (figure 5.3f) to determine coercivity of remanence B_{cr}. B_c and B_{cr} are closely related as demonstrated by *Dankers and Zijderveld* (1981) and are tendentially decreasing towards the top of both sections (figure 5.4).
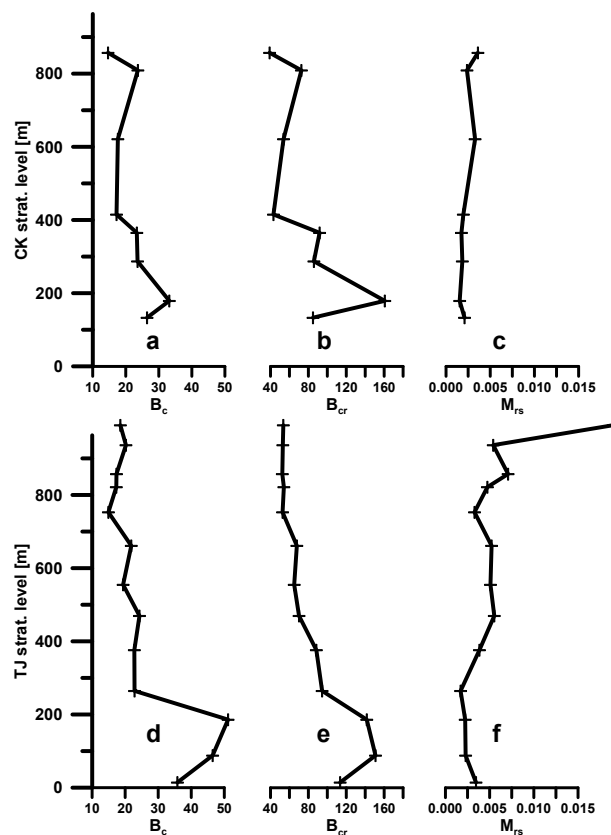
Figure 5.4.: Variation of coercive force (a,d), remenence coercivity (b, e) and saturation remanence (c, f) for B-cores from CK (a-c) and TJ (d-f) section with stratigraphy.

This can be caused by an increase of the magnetite to hematite ratio or an increase of grain sizes. M_{rs} increases towards the top, which indicates an increase of magnetite to hematite ratio and/or an increase of both fractions.

Susceptibility, ARM acquisition, NRM as well as the 3-axis 90 mT demagnetized moment obtained from 99 (65) B-cores of CK (TJ) sections all increase towards the top of the section (figure 5.5).
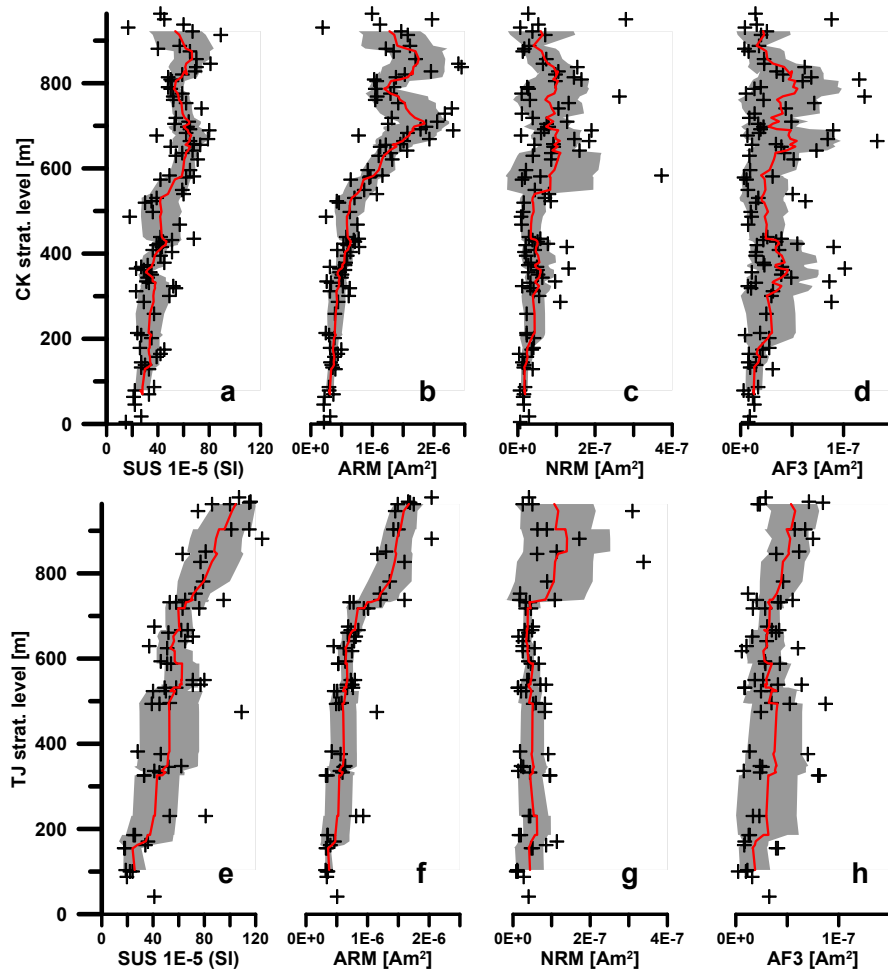
Figure 5.5.: Variation of bulk susceptibility (a, e), ARM acquisition (b, f), NRM (c, g) and 3 axis 90 mT AF demagnetized moment (d, h) for B-cores from CK (a-d, 99 cores) and TJ (e-h, 65 cores) section with stratigraphy. Data is clipped at maximum x value (in total 5 points omitted). Red lines are running averages with window width of 9 points. 1σ uncertainties in gray.

We interpret the increase of susceptibility and ARM acquisition as an upward increase of the total magnetite fraction. Whereas the increase of the demagnetized moments is indicative of an increase of high coercivity minerals like hematite, an increase of both magnetite and hematite content explains well the increasing NRM intensities and is compatible with the increase of M_{rs}. Counterintuitively, this implies that the abundance of red pigment changes inversely with the content of hematite. Potentially the red pigment is progressively developing with time or compaction (*Van Houten*, 1973).

A characteristic rise of ARM to values above 10^{-6} Am^2 can be seen at an approximate stratigraphic level of 600 m for TJ and 500 m for CK which could indicate a potential correlation of both sections.

Since the magnetic susceptibility of magnetite is about 1000 times greater than for hematite and ARM acquisition at low fields (< 90 mT) only affects a minor fraction of high coercivity minerals such as hematite, we assume that the King plot (figure 5.6) represents the properties of magnetite and not of hematite.
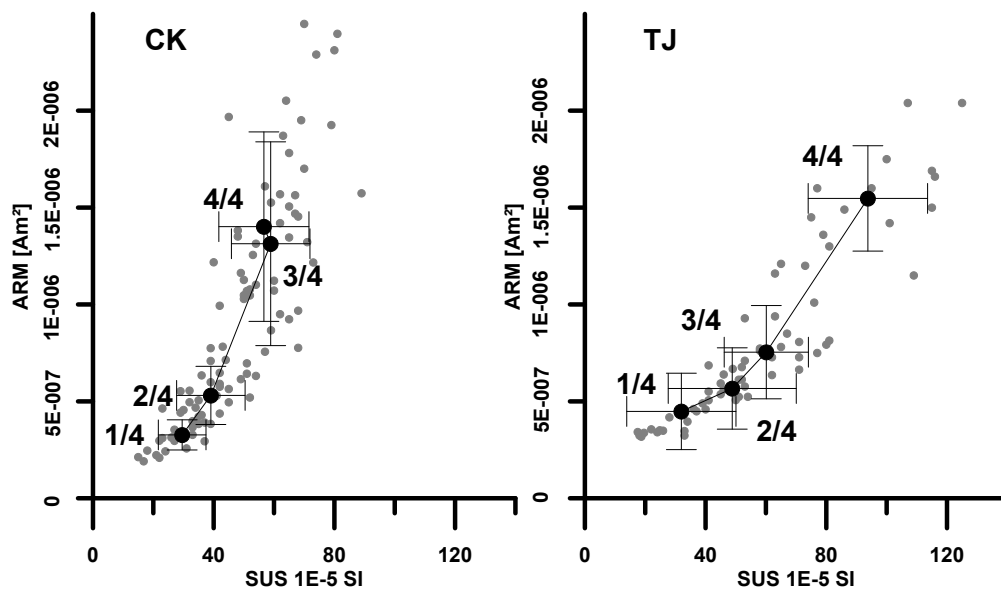
Figure 5.6.: ARM (90 mT peak AC, 0.1 mT DC) acquisition versus bulk susceptibility for CK and TJ section as labeled. Large points are averages for each fourth of the section. 1/4 is bottom, 4/4 is top.

For both sections, the ARM acquisition to susceptibility ratio (slope in figure 5.6) is mostly constant within error indicating constant magnetite grain sizes. The systematic variation away from the origin indicates a rise in magnetite abundance (*King et al.*, 1982, 1983). pARM spectra of CK (figure 5.7a) and TJ (figure 5.7b) section show constant peak positions around 20 mT which get sharper towards the top.

The increasing ratio of peak magnetic moment to the total ARM (90-0 mT) quantifies this trend (figure 5.7c, f). The peak position is typical for a grain size of 4 μm of magnetite (*Jackson*, 1991). The widening of the pARM spectra towards the bottom is expected from the previously established increase of magnetite to hematite ratio towards the top (i.e. low coercivity hematite widens the ARM spectra towards higher field values at the bottom of the sections).
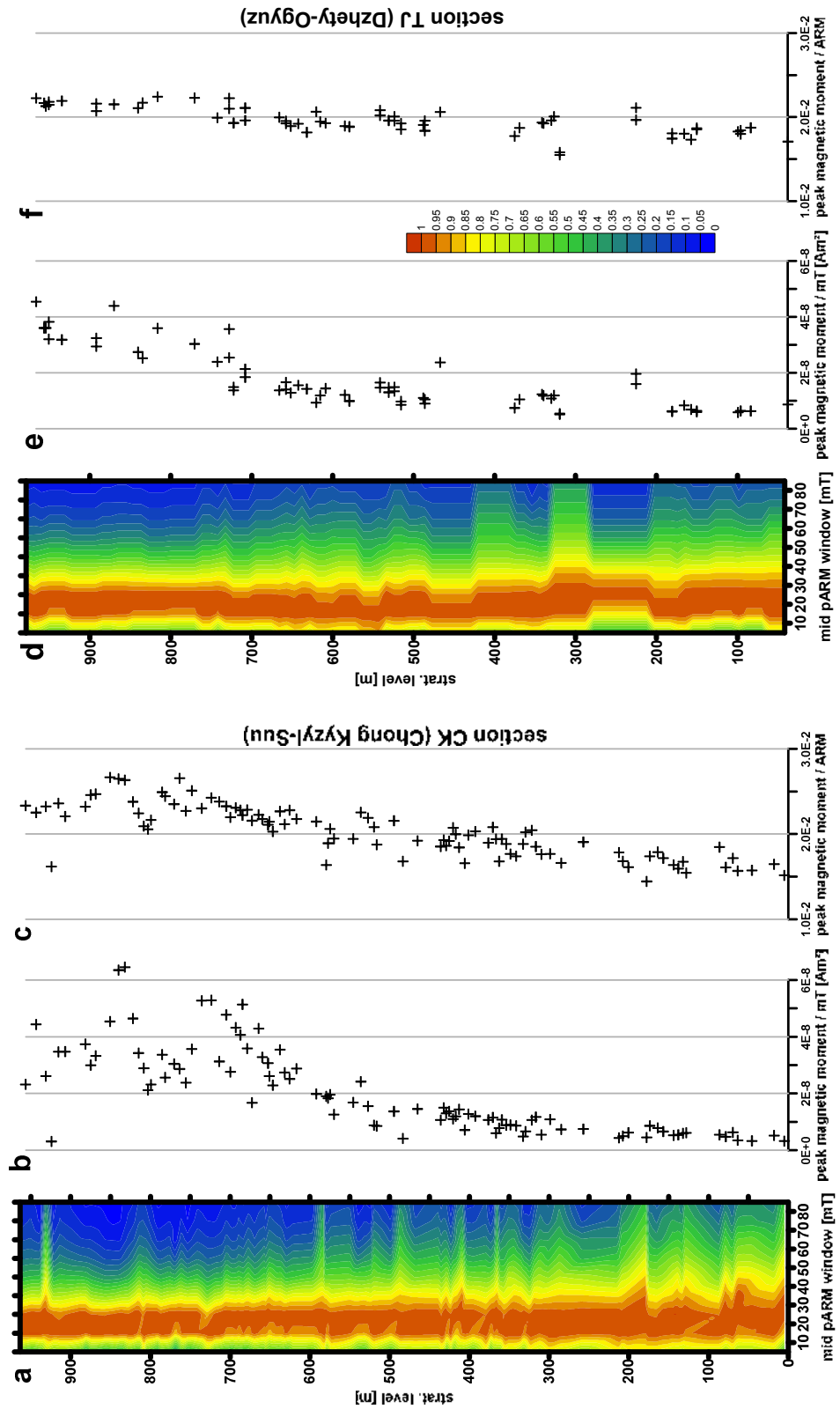
Figure 5.7.: pARM spectra as a function of depth for CK (a–c) and TJ (d–f) section. a, d: contoured pARM spectra. Each spectrum is normalized to its peak value (shown in b, e). Ratios of peak magnetic moment to total ARM increase towards the top in both sections (c, f).

5.3.2. Anisotropy of Anhysteretic Remanence

We measured ARM acquisition of 60 (98) B-cores from TJ (CK) section in 12
directions and converted those to anisotropy tensors which can be visualized by
the directions of their eigenvectors. We used a DC bias field of 0.1 mT and applied
it in a switching field window from 20 to 0 mT. Details about the measurement
procedure and protocol can be found in section 4.4. For both stratigraphic sec-
tions, we obtain a subhorizontal, and well defined maximum direction (k1) while
intermediate (k2) and maximum (k3) directions are streaked along a great circle
orthogonal to k1 (figure 5.8).   This is characteristic of a prolate fabric. Either
the intermediate and minimum eigenvalues are very similar and therefore the
rotation of the individual anisotropy ellipsoids around the maximum direction is
poorly defined or intermediate and minimum axis are distinct but physically not
well aligned for different samples. The declination of the maximum anisotropy
direction is similar for both sections (CK: 252.1°, TJ: 256.9°) and mimics the strike
directions. Both maximum anisotropy directions fall in between the averaged strike
directions of the two sections (figure 5.8, table 5.2). We propose that the former are

Site	Part	n	k1	k2	k3	Ds1	Is1	Ds2	Is2	Ds3	Is3
CK	all	98	1.036	0.983	0.981	252.1	5.5	162.0	1.7	55.1	84.2
	4/4	22	1.037	0.983	0.979	251.3	6.1	343.3	18.3	143.6	70.7
	3/4	29	1.035	0.986	0.979	250.8	4.0	160.5	4.8	20.4	83.8
	2/4	29	1.035	0.989	0.976	252.9	2.7	156.2	67.9	343.9	21.9
	1/4	18	1.045	0.984	0.971	265.3	17.9	5.9	29.7	148.5	54.3
TJ	all	60	1.032	0.988	0.979	256.9	14.1	27.8	69.0	163.0	15.2
	4/4	14	1.033	0.991	0.976	262.7	18.3	11.6	44.4	156.5	39.9
	3/4	23	1.049	0.987	0.964	260.8	14.7	93.3	75.0	351.7	3.1
	2/4	11	1.031	1.000	0.969	253.5	33.0	48.2	54.3	155.5	12.1
	1/4	12	1.020	1.005	0.975	270.1	18.0	16.6	41.3	162.3	43.2

Table 5.2.: Properties of averaged normalized tensors for CK and TJ section and
for each quarter of these. Number of specimens (n), eigenvalues (k), directions of
eigenvectors in stratigraphic coordinates (Ds, Is).

orthogonal to the maximum strain axis of the formation (*Graham*, 1966; *Borradaile
and Tarling*, 1981; *Hrouda*, 1982; *Winkler et al.*, 1997) which is demonstrated to
be nearly N-S in the area of Lake Issyk-Kul (*Sycheva et al.*, 2008). Deviation of
the strike directions from the k1 direction can be understood by the bow shaped
and indention like deformation (figure 5.1) that produces curvature in the fold
axes without vertical axis rotations. *Thomas et al.* (1993) obtained the virtually
identical direction for the maximum axis of AMS data from the Issyk-Kul basin
with a vertical minimum axis. They assumed that their AMS data reflects the
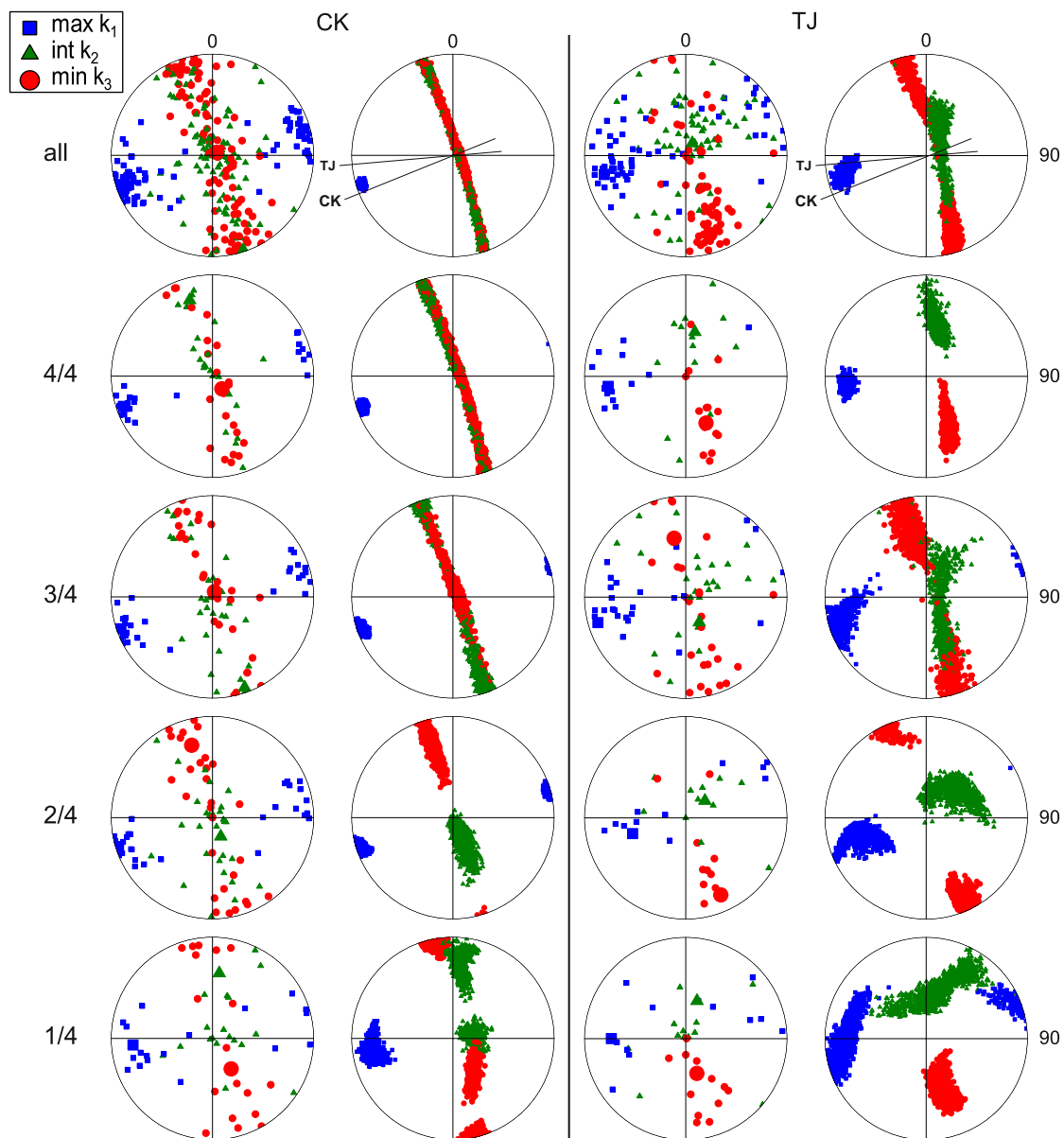
Figure 5.8.: Principal directions for AARM tensors for TJ and CK section in bedding corrected coordinates. Directions are plotted on lower hemisphere. First row shows data of entire sections and the strike lines of both sections. Subsequent rows show only data from each fourth of the sections. 1/4 is bottom, 4/4 is top of sections. Large symbols are averaged directions based on the mean of the normalized individual tensors. All data are shown twice: original (left) and bootstrapped (right). Geographic north is up, east to the right.

alignment of hematite particles. In contrast, we assume that our low coercivity anisotropy data is most sensitive to magnetite particles.

We quantify the magnetic fabric using the parameters of *Jelinek* (1981): the degree of anisotropy P, the shape parameter T (-1 prolate; 0 triaxial; +1 oblate), the lineation L and foliation F. The change of those parameters with stratigraphy (figure 5.9) reflects variations during sedimentation or later strain. The degree
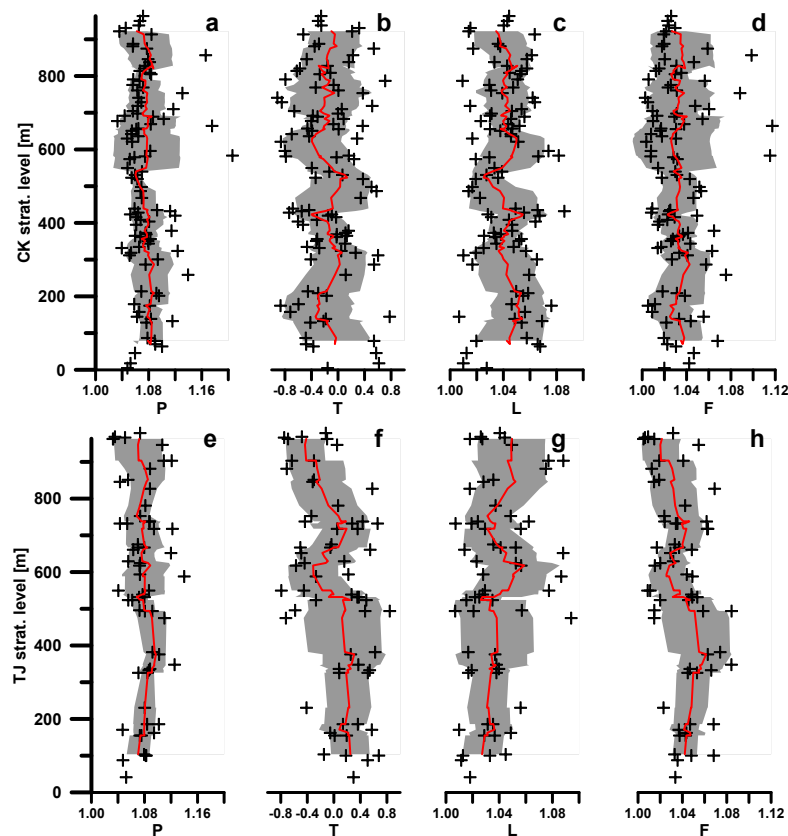
Figure 5.9.: Variation of degree of anisotropy (a, e), shape parameter (b, f), lineation (c, g), foliation (d, h) for CK (a-d) and TJ (e-h) section with stratigraphy. Red lines are running averages with window width of 9 points. 1σ uncertainties in gray.

of anisotropy (7.8±2.4% for TJ and 7.6±2.8% for CK) does not show a trend throughout either section. The TJ samples show shape parameters changing from oblate to prolate towards the top which is expected due to higher compaction at the bottom (figure 5.9f). This is consistent with the observed low lineations and

high foliations at the bottom of the section (figure 5.9g+h). We do not see an increase of P down-section, which would be expected for higher compaction. We estimate a lower amount of compaction for CK since no oblate fabrics are observed towards the bottom. The Flinn Diagram (*Flinn*, 1962) of both sections (figure 5.10) shows a strong scatter for individual samples. Averaged values for each quarter
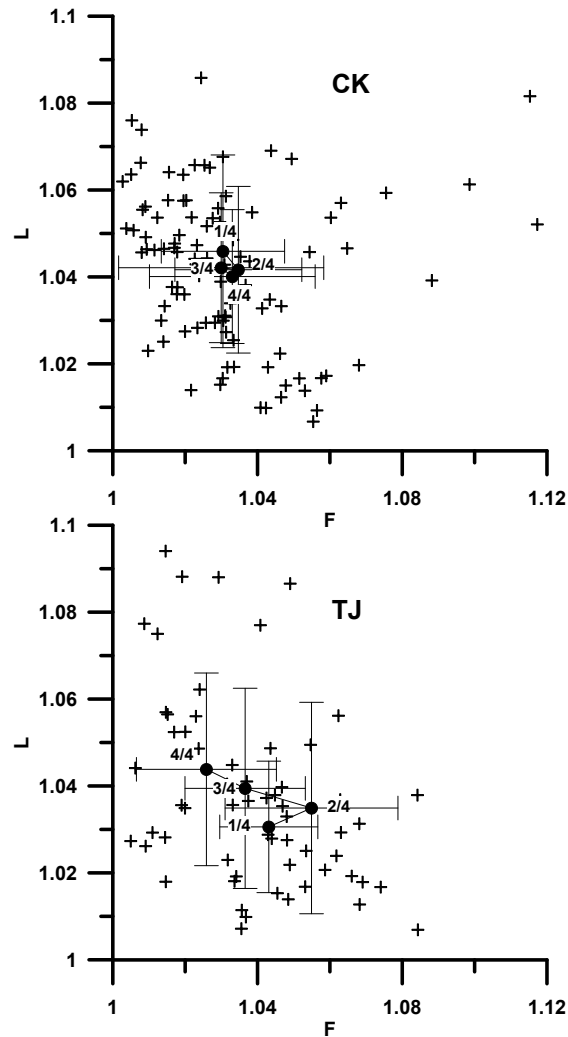
Figure 5.10.: Flinn diagrams of CK and TJ section. Vertical axis is lineation. Horizontal axis is foliation. Filled circles represent averages of each fourth of the section.

of the sections are closely clustered and solely prolate for CK section but vary systematically from oblate to prolate for TJ section towards the top as seen in the shape parameter. We interpret the latter as a progressively stronger tectonic fabric up-section.

5.3.3. Magnetic Remanence Directions

To constrain the characteristic paleomagnetic directions, we performed stepwise thermal demagnetization up to 685°C and alternating field demagnetization up to 90 mT on our samples. We used the deepest and therefore least weathered part (A-cores) of one core for each drilled bed for thermal demagnetization. B-cores, if available, were used for alternating field demagnetization. Due to the high coercivity of the samples, alternating field demagnetization removed in most cases only a minor fraction of the NRM and did therefore not yield interpretable *Zijderveld* (1967) plots.

Figure 5.11 shows representative thermal demagnetization data. NRM moments cover the range $5.2 \cdot 10^{-9}$ to $4.1 \cdot 10^{-7}$ ($2.7 \cdot 10^{-9}$ to $1.3 \cdot 10^{-6}$) Am^2 with an average of $5.1 \cdot 10^{-8}$ ($1.1 \cdot 10^{-7}$) Am^2 for CK (TJ). We show single component demagnetization paths of normal and inverse polarities (figure 5.11a-b), two component demagnetization (figure 5.11c), demagnetization along great circles (figure 5.11d) and noisy data that cannot be interpreted (figure 5.11e). In most cases two component demagnetization shows a present day overprint up to ≈ 300°C and a linear component towards the origin for higher temperatures. It's remarkable that the magnetite and hematite fractions yield the same direction (i.e. no curvature around 580°C), which suggests that both recorded the same paleofield. Due to the shallow bedding and scatter of directions it is difficult to identify overprints along the recent earth magnetic field (figure 5.11a+b) (IGRF D = 4.3° east; I = 62.2°; GAD D = 0°, I = 61.2°). Since all identified overprints were clearly removed around 300°C, we did not exclude any samples with high temperature components along the recent earth magnetic field. We obtain the characteristic remanent magnetization of each sample by principal component analysis (*Kirschvink*, 1980) of the demagnetization path at high temperature (> 350°C). 115 (98) characteristic directions for CK (TJ) are shown in figure 5.12. The bimodal mean declinations of 6.9±3.2° for CK and 6.1±3.6 for TJ (figure 5.13, table 5.3) are indistinguishable within a95 uncertainty estimates.

For the CK and TJ sections, the inverse polarity directions are steeper than the normal polarity ones, which we attribute to unremoved present day field overprints. Inclinations are shallower for TJ (40.7±3.5°) than for CK (46.2±3.3°) (inclination only statistics), which is likely caused by stronger compaction of the former section. This is supported by the oblate fabrics with subvertical minimum axis observed in
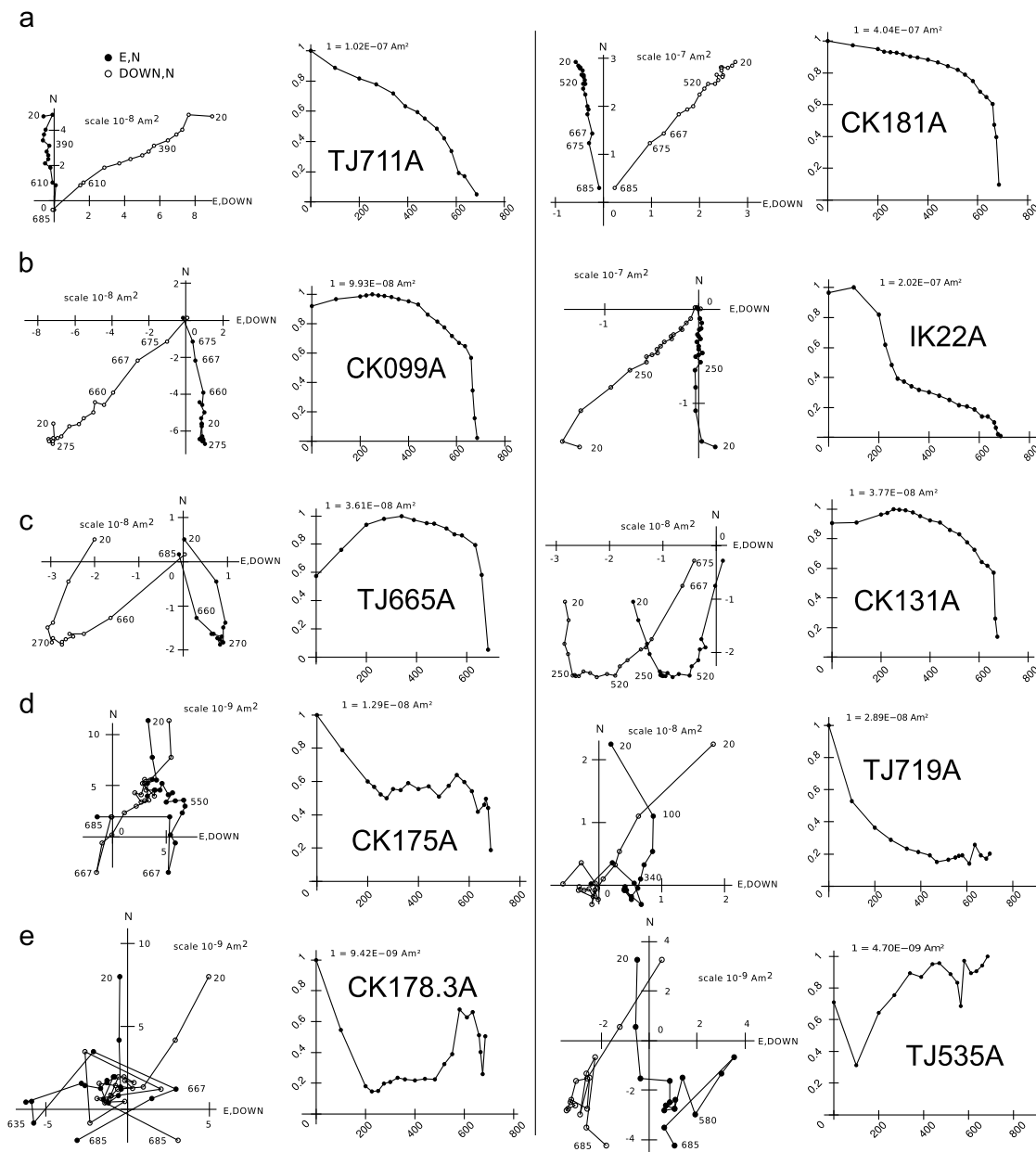
Figure 5.11.: Representative thermal demagnetization data of 10 samples. For each sample a Zijderveld plot in tilt corrected coordinates (left) and the decay of normalized magnetic moment with temperature (right) is shown. a) normal polarity magnetization; b) inverse polarity magnetization; c) inversed polarity magnetization with overprint; d) magnetization directions do not decay towards the origin and are unstable at high temperatures. Polarity can be identified by great circle fitting; e) data not interpretable.
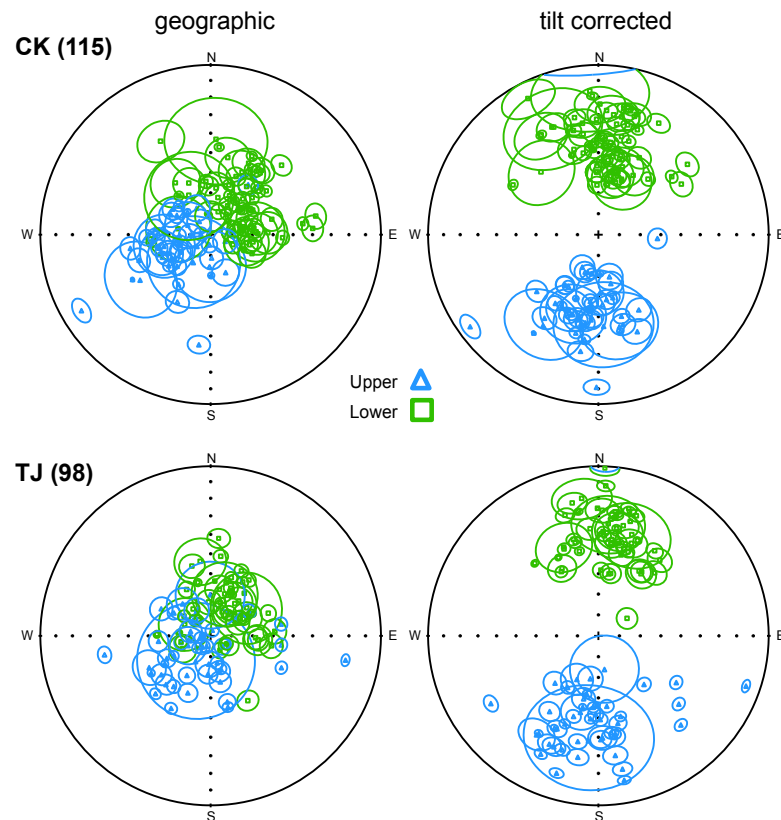
Figure 5.12.: High temperature characteristic magnetization directions for CK and TJ section in geographic (left) and tilt corrected (right) coordinates. Number of samples in brackets. Circles are a95 error constraints.

the lowest part of TJ section. The bipolar mean direction of TJ section (D = 6.1°, I = 42.9°, a95° = 3.6°) falls within the a95 uncertainty estimates obtained by *Thomas et al.* (1993) (D = 0°, I = 44°, a95=11°) from 5 sites in the Dzhety-Ogyuz formation.

To obtain a representative paleomagnetic direction for the whole study area, we neglect the sites IK3 and IK5 which show uncertainties of a95 above 15° and the largest deviations from the common mean. The bimodal mean TM of all other sites (D = 3.1°, I = 51.7°, a95 = 5.3°) is indistinguishable within 95% confidence limits from *Thomas et al.* (1993) mean direction for the entire Issyk-Kul basin (D = 2°, I = 49°, a95 = 6°).
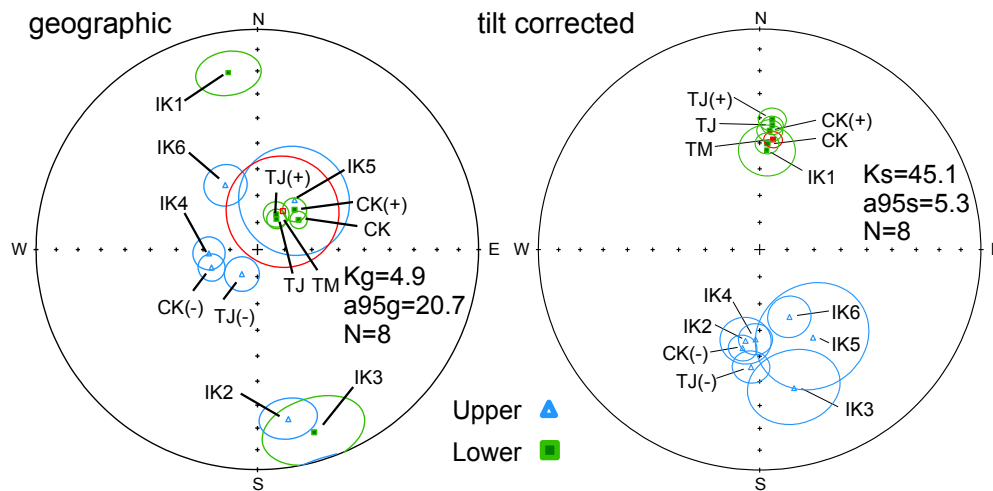
Figure 5.13.: Fisher means of all sites in geographic and tilt corrected coordinates. Data from CK and TJ section is split into normal (+) and inverse (-) polarities. Total mean (TM) includes all sites except IK3 and IK5 and is shown in red. Statistical values of TM inside figures. Circles are a95 error constraints.

Comparison with the paleomagnetic pole of Eurasia for 20 Ma (*Besse and Courtillot*, 2002) reveals a rotation of -5±6° and a difference in paleolatitude of 11±5° which requires an unrealistic translation of 1200±500 km towards the north. More likely, this is the effect of inclination shallowing, which is frequently observed in Central Asia (e.g., *Si and Voo*, 2001; *Gilder et al.*, 2001, 2003; *Tan et al.*, 2003; *Yan et al.*, 2005).

The two magnetostratigraphic sections are not suitable for a fold test since their beddings are very similar. Therefore we sampled six additional sites (IK1-IK6) at an anticlinal structure about 14 km north of Chon Kyzyl-Suu (figure 5.1). Means for all sites are shown in figure 5.13 and listed in table 5.3. The parametric simulation fold test (*Watson and Enkin*, 1993) on IK, CK and TJ directions yields an optimum degree of untilting of 120% and is negative. Assuming a reasonable (at least for the IK sites) circular standard deviation for bedding determination of 7° includes the 100% untilting level within the 95% confidence interval and renders the test positive. We conclude that the remanence was acquired before folding of the sediments. The same was found by *Thomas et al.* (1993) for 13 site means from Issyk-Kul basin.

Location	n	Dg	Ig	Ds	Is	ks	a95	Mean
IK1	5	350.7	19.7	4.1	52.7	60.7	9.9	Fisher
IK2	6	169.7	-22.8	188.8	-55.5	56.4	9.0	Fisher
IK3	4	162.8	14.2	166.1	-35.5	37.0	15.3	Fisher
IK4	6	265.5	-72.1	182.7	-56.5	125.6	6.0	Fisher
IK5	7	36.8	-67.1	148.9	-51.5	9.8	20.3	Fisher
IK6	7	333.7	-63.3	156.3	-62.7	60.8	7.8	Fisher
CK(+)	67	42.9	69.9	4.8	45.0	16.5	4.4	Fisher
CK(-)	48	248.5	-71.9	189.8	-52.6	17.9	5.0	Fisher
CK	115	54.1	71.3	6.9	48.4	17.9	3.2	Watson
TJ(+)	52	28.0	75.3	5.5	40.5	18.6	4.7	Fisher
TJ(-)	46	212.2	-79.3	184.2	-45.6	11.8	6.4	Fisher
TJ	98	32.5	76.6	6.1	42.9	16.9	3.6	Watson
TM	8	35.5	73.2	3.1	51.7	45.1	5.3	Watson

Table 5.3.: Fisher and bipolar Watson means of characteristic magnetic directions for CK, TJ and IK sites. For magnetostratigraphic sections CK and TJ mean directions for normal (+) and inverse (-) polarities are listed separately. TM is the bipolar Watson mean of IK1-2, IK4, IK6, CK(+,-) and TJ(+,-).

5.3.4. Magnetostratigraphy

We classified each interpretable sample into normal, inverse or intermediate polarity based on characteristic magnetization directions and great circle fitting. In total, we identified 40 polarity chrons based on 75 normal, 79 inverse, 12 intermediate (54 normal, 81 inverse, 23 intermediate) magnetization polarities in the CK (TJ) section. Figure 5.14 shows the ascertained polarities with stratigraphic level for both sections. A potential match between both polarity patterns suggests a large overlap and an offset towards younger strata for TJ by approximately 350 m. An overlap between the sections was expected from the observed rock fabric and strike directions. Our preferred correlation of polarity patterns of both sections does not agree with the sense of offset of the age boundaries marked in the geological map (figure 5.1) and neglects the correlation suggested by the characteristic rise of ARM acquisition in both sections. The latter could be a time-transgressive feature caused by lateral range propagation.

Our correlation with the paleomagnetic timescale (*Gradstein and Ogg*, 2004) is not conclusive but shows our preferred interpretation. Absolute sedimentation ages range from 25.5 to 16.3 Ma for CK and from 22 to 13.2 Ma for TJ. It implies slightly different but constant sedimentation rates of 9.8 cm per ka for CK and 10.6 cm per ka for TJ (figure 5.15) which are in good agreement with
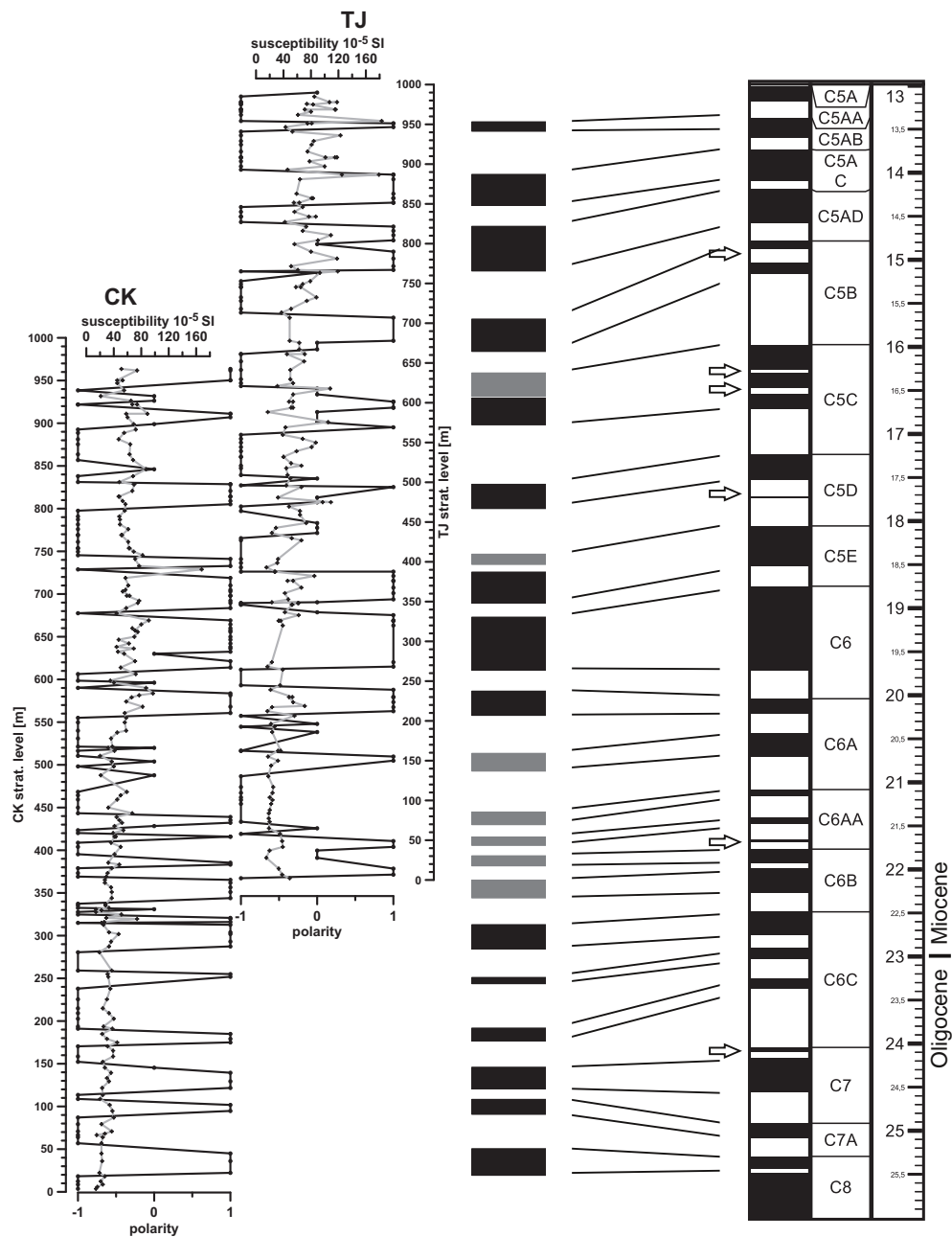
Figure 5.14.: Paleomagnetic polarities for CK and TJ section and a possible correlation with the geomagnetic polarity timescale from *Gradstein and Ogg* (2004). Polarities are based on principal component analysis and great circle fitting. Susceptibility is overlain to the stratigraphic polarities. Gray stripes indicate positive polarities that could not be identified in both sections. Arrows indicate missing crons in the stratigraphic record. Geomagnetic polarity time scale on the right is in Ma. Polarity and time scale are created with the Time-Scale Creator program (*Gradstein et al.*, 2008).

recent thermochronological estimates (Euan Macaulay, data in preparation) but at the lower end of rates published for the front of active mountain ranges (*Gilder et al.*, 2001; *Charreau et al.*, 2005, 2006, 2009b, 2011; *Sun et al.*, 2009). Similar sedimentation rates are reported from the Jingou River section (China) (*Charreau et al.*, 2009a).
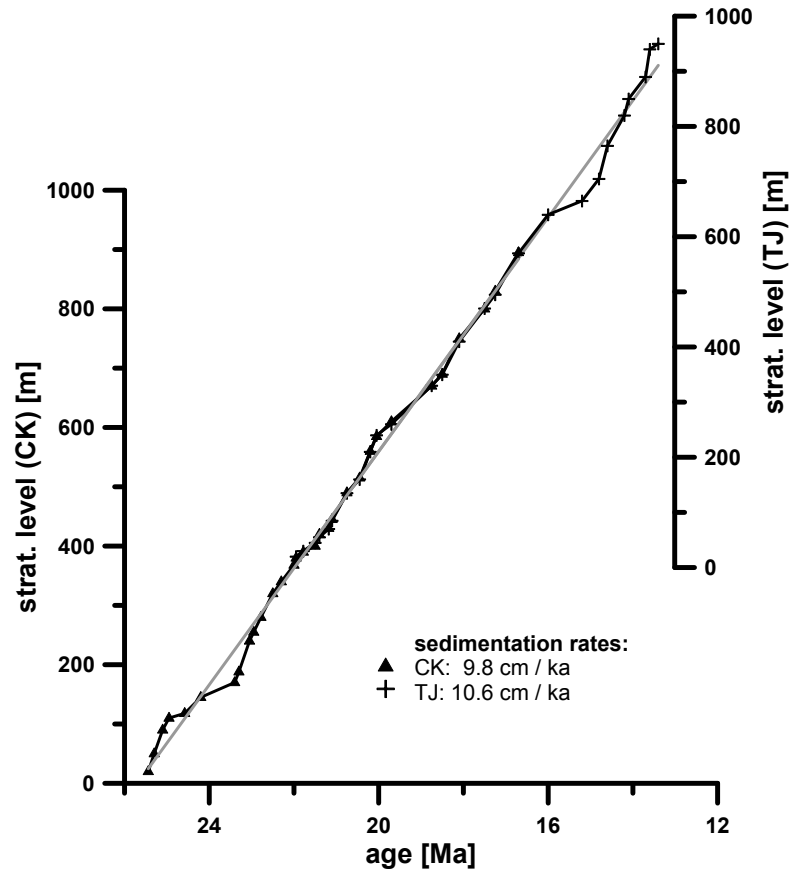
Figure 5.15.: Linear correlation of magnetization age versus stratigraphic level of two overlapping magnetostratigraphic sections CK and TJ implies constant sedimentation rates. Age model is based on matched magnetic polarity changes of the geomagnetic polarity time scale (*Gradstein et al.*, 2008).

5.4. **Conclusions**

We studied Cenozoic sediments from two magnetostratigraphic sections from Kyrgyzstan and six close-by sites. We found hematite and magnetite as the carriers of the magnetic signal. Magnetite and hematite content increases towards the top of both sections and so does the magnetite to hematite ratio (i.e. the magnetite fraction increases more than the hematite fraction). Hematite and magnetite fraction recorded the same paleofield. A positive fold test proves that the identified characteristic magnetization directions were acquired before folding. Directional results are compatible with an earlier study by *Thomas et al.* (1993).

The study mean direction (D = 3.1°, I = 51.7°, a95 = 5.3°) does not show a significant tectonic rotation but has a shallower inclination than expected from the apparent polar wander path, which is often observed in sediments in Central Asia, but is hard to explain in a tectonic context. Therefore we conclude that the inclination suffers from flaws in the recording process of the magnetic field direction, commonly known as 'inclination shallowing'.

To our knowledge, existing dating of the formation is based on low resolution biostratigraphy from remnants of a tortoise (*Sidorenko*, 1972) and lithostratigraphic correlation with another section which overlies Eocene basalts (*Krilov*, 1960). Based on our magnetostratigraphic correlation we propose sedimentation ages ranging from 25.5 to 13.2 Ma, which places the entire measured TJ section on top of the Paleogene-Neogene boundary in contrast to the existing mapping that places the top of the TJ section at that boundary. Associated sedimentation rates are ca. 10 cm per ka which is low compared to sedimentation rates found at other magnetostratigraphic sections in the Tianshan realm. Therefore, we infer that 13.2 Ma pre-dates the most active phase of uplift of the Kyrgyz Tianshan. This interpretation agrees with thermochronologic results obtained from the Tereskey range (*Macaulay et al.*, 2011), directly south of our study area. The timing of our section corresponds remarkably well with the onset and termination of rapid shortening on the southern flank of the Tianshan, ≈220 km to the SSW (*Heermance et al.*, 2008).

Anisotropy of anhysteretic remanence reveals a well defined, subhorizontal maximum axis perpendicular to the assumed N-S compression which is virtually identical for both sections and falls in between the average strike directions. It agrees well with the maximum direction of AMS found by *Thomas et al.* (1993). The magnetic fabric deduced from ARM measurements in this study is dominated by magnetite. The assumption of *Thomas et al.* (1993) that the AMS signal is carried by hematite implies that the magnetic fabrics of hematite and magnetite agree.

6. Conclusions and Future Prospects

This work presented the setup of an automated measurement system called 'SushiBar' especially designed to study the anisotropy of anhysteretic remanent magnetization acquisition on hundreds to thousands of inch-core sized specimens and its application to sedimentary samples from Central Asia.

One requirement due to the physical extent of the measurement system is the construction of a magnetically shielded room which is reasonably done by the use of passive shielding. Shielding can be achieved by enclosing the volume within a thin layer of appropriately magnetized sheets of high permeable material like transformer steel. Even better shielding, especially against time varying fields, can be obtained with optimized materials like mu-metal. Simplified 2D numerical models can be used to predict the shielding effect of different geometries. Arrangement of the openings in field direction avoid the need of shielded doors.

Furthermore customized software was needed to interface with the cryogenic magnetometer, since existing software cannot be adopted to an automated measurement setup. I therefore developed the open source computer program 'CryoMag' for manual magnetization measurements, which can be used by any lab for free. The usage is not restricted to a specific operating system. It can be customized to any sequence of specimen and sample holder orientations and can be used with three component SQUID, as well as two component spinner magnetometers, which are the most popular instruments for inch cores. Adaption to new instruments is possible since the source code is available.

Anisotropy of ARM is superior to the commonly used method based on susceptibility (AMS), since it is not prone to the problem of inverse fabrics and reflects the signal of the remanence carrying grains, which transport the paleomagnetic information.

An important advantage is the possibility to focus on subpopulations of grains through the chosen switching field range. For low switching field ranges (20-0 mT) the ARM method mimics the magnetic fabric obtained from AMS measurements of the samples from Central Asia studied in this work. Application of the ARM method in higher switching fields resulted in magnetic fabrics that were distinctly different from those defined by AMS and probably linked to the paleomagnetic remanence. The studied magnetostratigraphic sections in Kyrgyzstan show an intense tectonic fabric with well defined maximum axes that mimic the strike direction, perpendicular to the maximum strain axis.

Viscosity of ARM is an important factor to consider for experiments. Decays of 3% within 10 minutes observed for some sedimentary samples in this work can strongly affect sensitive measurements like that of anisotropy, when the timing of acquisition and measurements is not well controlled. Interpretation of magnetic viscosity is difficult, since it is not clear whether it stems from a small amount of highly viscous material or a large amount of low viscous material. ARMs imparted in different switching field windows, which address different grain size fractions, show systematical differences in magnetic viscosity. For the samples studied here, low switching field windows (20-0 mT) result in rapidly decaying magnetizations (high magnetic viscosity) whereas high switching field windows (90-70 mT) result in slower decaying magnetizations (low magnetic viscosity).

ARM spectra can be used to identify the grain size distribution of magnetite or, if switching fields allow, to study the contribution of minerals with higher coercivities. The sections from Kyrgyzstan and China show well defined and constant peak positions of the ARM spectra throughout each individual section. The Kyrgyz sections have magnetite grain sizes of 4 μm whereas the Chinese section has smaller grain sizes of 2-3 μm. Rock magnetic data suggest an increase of magnetite abundance, hematite abundance and magnetite to hematite ratio towards the top for all sections.

A significant overlap of the two parallel Kyrgyz sections was found by correlating the magnetostratigraphic polarity pattern to each other. Absolute magnetization ages from 25.5 to 13.2 Ma based on a correlation with the geomagnetic polarity

timescale are proposed but the relation is not unique due to the lack of absolutely dated points. A fold test proved that the age of magnetization predates folding. Furthermore previously published paleomagnetic directions were confirmed and refined. Sedimentation rates are low in comparison with other Neogene sections from the Tienshan realm, it seems the active phase of uplift occurred after 13.2 Ma.

The SushiBar in its current state reliably carries out different measurement protocols to obtain high quality data. The strict automatic execution of procedures avoids spurious data due to magnetic viscosity or human negligence, which are mostly hard to identify and to correct. The SushiBar is also well suited for ordinary stepwise AF or thermal (with separate oven) demagnetization as it is frequently used for paleomagnetic studies and therefore frees human resources. Due to the experiences from almost one year of measurements, slight modifications of the sample handler system and particularly the enhancement of the experimental possibilities are planned for the future. Redesign of the sample handler system will maximize the admissible length of specimens and will facilitate a better coupling of the cups with the sample handler. The reduction of mass and/or a magnetically cleaner material will reduce the magnetic moments of the cups, which limits the sensitivity of the system, especially for ARM experiments.

Adding a high field ($\approx$500 mT) IRM/AF/ARM coil will allow to affect high coercivity minerals like hematite or goethite and will make AF demagnetization useful for a much wider range of rocks and help to avoid the time consuming thermal treatment in some cases. Spectra and anisotropies of ARM at higher switching field windows will allow one to study smaller magnetite grains and minerals with higher coercivity. Integration of AMS measurement capabilities could allow the automatic detection of single domain fabrics. An integrated balance will allow automatic normalization of the magnetic moment to the mass. Such additional instruments can be easily integrated into the system by adding extra sample handlers. Small and not interfering instruments can be stacked to save space. The extension of the system will increase the amount of data obtained but not necessary the measurement time due to the parallel operation of all sample handlers and instruments. The systematic and automatic application of all such methods to synthetic samples could help interpret the results obtained from natural samples.

A. Bibliography

Abdrakhmatov, K., R. Weldon, S. C. Thompson, D. Burbank, C. Rubin, M. Miller, and P. Molnar, Onset, style and current rate of shortening in the central Tien Shan, Kyrgyz Republic, *Russ. Geol. Geophys*, *42*, 1585–1609, 2001.

Abdrakhmatov, K., et al., Relatively recent construction of the Tien Shan inferred from GPS measurements of present-day crustal deformation rates, *Nature*, *384*(5), 450–453, 1996.

Afremov, L. L., V. I. Belokon', and K. V. Nefedev, Magnetic aftereffect in systems of single-domain interacting particles and magnetic viscosity of rocks, *Izvestiya, Physics of the Solid Earth*, *45*(1), 57–62, doi: 10.1134/S106935130901008X, 2009.

Avouac, J.-P., and P. Tapponnier, Kinematic model of active deformation in central Asia, *Geophysical Research Letters*, *20*(10), 895–898, 1993.

Besse, J., and V. Courtillot, Apparent and true polar wander and the geometry of the geomagnetic field over the last 200 Myr, *Journal of Geophysical Research*, *107*(B11), 2300, doi: 10.1029/2000JB000050, 2002.

Biquand, D., On the stability of the viscous remanent magnetization in sedimentary rocks when submitted to AF demagnetization: New experimental results, *Physics of The Earth and Planetary Interiors*, *19*(3), 209–227, doi: 10.1016/0031-9201(79)90023-2, 1979.

Borradaile, G. J., and D. Tarling, The influence of deformation mechanisms on magnetic fabrics in weakly deformed rocks, *Tectonophysics*, *77*(1-2), 151–168, doi: 10.1016/0040-1951(81)90165-7, 1981.

Box, G., and J. Hunter, Multi-factor experimental designs for exploring response surfaces, *The Annals of Mathematical Statistics*, *28*(1), 195–241, 1957.

Bullen, M., D. Burbank, J. Garver, and K. Abdrakhmatov, Late Cenozoic tectonic evolution of the northwestern Tien Shan: New age estimates for the initiation of mountain building, *Geological Society of America Bulletin*, *113*(12), 1544–1559, doi: 10.1130/0016-7606(2001)113<1544:LCTEOT>2.0.CO;2, 2001.

Burbank, D., A. Meigs, and N. Brozovic, Interactions of growing folds and coeval depositional systems, *Basin Research*, *8*(3), 199–223, doi: 10.1046/j. 1365-2117.1996.00181.x, 1996.

Burtman, B. S., The Tien Shan Early Paleozoic tectonics and geodynamics, *Russian Journal of Earth Sciences*, *8*(ES3003), 1–23, doi: 10.2205/2006ES000202, 2006.

Buslov, M., J. Klerkx, K. Abdrakhmatov, D. Delvaux, V. Batalev, O. A. Kuchai, B. Dehanschutter, and A. Muralev, Recent strike-slip deformation of the northern Tien Shan, *Intraplate strikeslip deformation belts*, *210*(1), 53–64, doi: 10.1144/GSL.SP.2003.210.01.04, 2003.

Buslov, M., J. Degrave, E. Bataleva, and V. Batalev, Cenozoic tectonic and geodynamic evolution of the Kyrgyz Tien Shan Mountains: A review of geological, thermochronological and geophysical data, *Journal of Asian Earth Sciences*, *29*(2-3), 205–214, doi: 10.1016/j.jseaes.2006.07.001, 2007.

Butler, R. F., *Paleomagnetism: magnetic domains to geologic terranes*, 319 pp., Blackwell Scientific Publications, Boston, 1992.

Charreau, J., Y. Chen, S. Gilder, S. Dominguez, J.-P. Avouac, S. Sen, D. Sun, Y. Li, and W.-M. Wang, Magnetostratigraphy and rock magnetism of the Neogene Kuitun He section (northwest China): implications for Late Cenozoic uplift of the Tianshan mountains, *Earth and Planetary Science Letters*, *230*(1-2), 177–192, doi: 10.1016/j.epsl.2004.11.002, 2005.

Charreau, J., S. Gilder, Y. Chen, S. Dominguez, J.-P. Avouac, S. Sen, M. Jolivet, Y. Li, and W.-M. Wang, Magnetostratigraphy of the Yaha section, Tarim Basin (China): 11 Ma acceleration in erosion and uplift of the Tian Shan mountains, *Geology*, *34*(3), 181, doi: 10.1130/G22106.1, 2006.

Charreau, J., et al., Neogene uplift of the Tian Shan Mountains observed in the magnetic record of the Jingou River section (northwest China), *Tectonics*, *28*(2), doi: 10.1029/2007TC002137, 2009a.

Charreau, J., et al., The Neogene Xiyu Formation, a diachronous prograding gravel wedge at front of the Tianshan: Climatic and tectonic implications, *Earth and Planetary Science Letters*, *287*(3-4), 298–310, doi: 10.1016/j.epsl. 2009.07.035, 2009b.

Charreau, J., et al., Paleo-erosion rates in Central Asia since 9Ma: A transient increase at the onset of Quaternary glaciations?, *Earth and Planetary Science Letters*, *304*(1-2), 85–92, doi: 10.1016/j.epsl.2011.01.018, 2011.

Cobbold, P. R., P. Davy, D. Gapais, E. Rossello, E. Sadybakasov, J. Thomas, J. Tondji Biyo, and M. de Urreiztieta, Sedimentary basins and crustal thickening, *Sedimentary Geology*, *86*(1-2), 77–89, doi: 10.1016/0037-0738(93)90134-Q, 1993.

Cobbold, P. R., E. Sadybakasov, and J. Thomas, Cenozoic transpression and basin development, Kyrgyz Tien Shan, central Asia, in *Geodynamic Evolution of Sedimentary Basins*, edited by R. François, E. Nadine, S. V.S., and S. I.I., pp. 181–202, Technip, Paris, 1996.

Coe, R. S., Analysis of magnetic shape anisotropy using second-rank tensors, *Journal of Geophysical Research*, *71*(10), 2637–2644, 1966.

Cogné, J. P., PaleoMac: A Macintosh application for treating paleomagnetic data and making plate reconstructions, *Geochemistry Geophysics Geosystems*, *4*(1), 1–8, doi: 10.1029/2001GC000227, 2003.

Collinson, D. W., *Methods in rock magnetism and palaeomagnetism: techniques and instrumentation*, 503 pp., Chapman and Hall, London, 1983.

Constable, C., and L. Tauxe, The bootstrap for magnetic susceptibility tensors, *Journal of Geophysical Research*, *95*(B6), 8383–8395, 1990.

Copeland, R., *Essential SQLAlchemy*, 240 pp., O'Reilly Media, 2008.

Czichos, H. (Ed.), *Die Grundlagen der Ingenieurwissenschaften (Fundamentals of Engineering)*, 30st ed., 1570 pp., Springer-Verlag, Berlin, Germany, 1996.

Dankers, P., and J. Zijderveld, Alternating field demagnetization of rocks, and the problem of gyromagnetic remanence, *Earth and Planetary Science Letters*, *53*(1), 89–92, doi: 10.1016/0012-821X(81)90029-7, 1981.

Day, R., M. Fuller, and V. Schmidt, Hysteresis properties of titanomagnetites: grain-size and compositional dependence, *Physics of the Earth and Planetary Interiors*, *13*(4), 260–267, 1977.

De Grave, J., M. Buslov, and P. Van den haute, Distant effects of India–Eurasia convergence and Mesozoic intracontinental deformation in Central Asia: Constraints from apatite fission-track thermochronology, *Journal of Asian Earth Sciences*, *29*(2-3), 188–204, doi: 10.1016/j.jseaes.2006.03.001, 2007.

Dunlop, D., and K. Argyle, Thermoremanence, anhysteretic remanence and susceptibility of submicron magnetites: Nonlinear field dependence and variation with grain size, *J. geophys. Res*, *102*(20), 199–20, 1997.

Egli, R., and W. Lowrie, Anhysteretic remanent magnetization of fine magnetic particles, *Journal of Geophysical Research*, *107*(B10), 2209, doi: 10.1029/ 2001JB000671, 2002.

Fisher, R., Dispersion on a sphere, *Proceedings of the Royal Society of*, *305*, 295–305, doi: 10.1098/rspa.1953.0064, 1953.

Flinn, D., On Folding During Three-Dimensional Progressive Deformation, *Quarterly Journal of the Geological Society*, *118*(1-4), 385–428, doi: 10.1144/ gsjgs.118.1.0385, 1962.

Frederichs, T., C. Hilgenfeldt, and K. Fabian, A modified version of the 2G cryogenic magnetometer, *Terra Nostra*, *10*, 41–43, 2000.

Gaunt, P., Magnetic viscosity and thermal activation energy, *Journal of applied physics*, *59*, 4129–4132, doi: 10.1086/124989, 1986.

Giddings, J., C. Klootwijk, and J. Rees, Automated AF-demagnetization on the 2G-Enterprises through-bore, cryogenic magnetometer, *Geologie en Mijnbouw*, *76*(1), 35–44, 1997.

Gilder, S., Y. Chen, and S. Sen, Oligo-Miocene magnetostratigraphy and rock magnetism of the Xishuigou section, Subei (Gansu Province, western China) and implications for shallow inclinations in central Asia, *Journal of Geophysical*, *106*(B12), 30,505–30,521, 2001.

Gilder, S., Y. Chen, J. P. Cogné, X. Tan, V. Courtillot, D. Sun, and Y. Li, Paleomagnetism of Upper Jurassic to Lower Cretaceous volcanic and sedimentary rocks from the western Tarim Basin and implications for inclination shallowing and absolute dating of the M-0 (ISEA?) chron, *Earth and Planetary Science Letters*, *206*(3-4), 587–600, 2003.

Girdler, R. W., The Measurement and Computation of Anisotropy of Magnetic Susceptibility of Rocks, *Geophysical Journal International*, *5*(1), 34–44, doi: 10.1111/j.1365-246X.1961.tb02927.x, 1961.

Gong, Z., C. Langereis, and T. Mullender, The rotation of Iberia during the Aptian and the opening of the Bay of Biscay, *Earth and Planetary Science Letters*, *273*(1-2), 80–93, doi: 10.1016/j.epsl.2008.06.016, 2008.

Goree, W., and M. Fuller, Magnetometers using RF-driven squids and their applications in rock magnetism and paleomagnetism, *Reviews of Geophysics*, *14*(4), 591–608, 1976.

Gradstein, F., and J. Ogg, Geologic Time Scale 2004 - why, how, and where next!, *Lethaia*, *37*(2), 175–181, doi: 10.1080/00241160410006483, 2004.

Gradstein, F. M., J. G. Ogg, and M. van Kranendonk, On the Geologic Time Scale 2008, *Newsletters on Stratigraphy*, *43*(1), 5–13, doi: 10.1127/0078-0421/2008/0043-0005, 2008.

Graham, J., Significance of magnetic anisotropy in Appalachian sedimentary rocks, *The earth beneath the continents*, *10*, 627–648, 1966.

Harold, E., and W. Means, *XML in a Nutshell*, 480 pp., O'Reilly Media, Sebastopol, CA, 2001.

Heermance, R. V., J. Chen, D. W. Burbank, and J. Miao, Temporal constraints and pulsed Late Cenozoic deformation during the structural disruption of the active Kashi foreland, northwest China, *Tectonics*, *27*(6), doi: 10.1029/2007TC002226, 2008.

Hext, G., The estimation of second-order tensors, with related tests and designs, *Biometrika*, *50*(3-4), 353, 1963.

Hilgenfeld, B., E. Strähmel, H. Nowak, and J. Haueisen, Active magnetic shielding for biomagnetic measurement using spatial gradient fields, *Physiological Measurement*, *24*(3), 661–669, 2003.

Housen, B., C. Richter, and B. van Der Pluijm, Composite magnetic anisotropy fabrics: experiments, numerical models and implications for the quantification of rock fabrics, *Tectonophysics*, *220*(1-4), 1–12, 1993.

Hrouda, F., Magnetic anisotropy of rocks and its application in geology and geophysics, *Surveys in Geophysics*, *5*(1), 37–82, doi: 10.1007/BF01450244, 1982.

Hu, S., E. Appel, V. Hoffmann, W. W. Schmahl, and S. Wang, Gyromagnetic remanence acquired by greigite (Fe_3S_4) during static three-axis alternating field demagnetization, *Geophysical Journal International*, *134*, 831–842, 1998.

Hu, S., A. Stephenson, and E. Appel, A study of gyroremanent magnetisation (GRM) and rotational remanent magnetisation (RRM) carried by greigite from lake sediments, *Geophysical Journal International*, *151*(2), 469–474, 2002.

Huang, B., J. Piper, S. Peng, T. Liu, Z. Li, Q. Wang, and R. Zhu, Magnetostratigraphic study of the Kuche Depression, Tarim Basin, and Cenozoic uplift of the Tian Shan Range, Western China, *Earth and Planetary Science Letters*, *251*(3-4), 346–364, doi: 10.1016/j.epsl.2006.09.020, 2006.

Jackson, M., Anisotropy of magnetic remanence: a brief review of mineralogical sources, physical origins, and geological applications, and comparison with susceptibility anisotropy, *Pure and Applied Geophysics*, *136*(1), 1–28, 1991.

Jackson, M., W. Gruber, J. Marvin, and S. Banerjee, Partial anhysteretic remanence and its anisotropy: Applications and grainsize-dependence, *Geophysical Research Letters*, *15*(5), 440–443, 1988.

Jaep, W. F., Anhysteretic Magnetization of an Assembly of Single-Domain Particles, *Journal of Applied Physics*, *40*(3), 1297, doi: 10.1063/1.1657638, 1969.

Jelinek, V., Statistical processing of anisotropy of magnetic susceptibility measured on groups of specimens, *Studia Geophysica et Geodaetica*, *22*(1), 50–62, 1978.

Jelinek, V., Characterization of the magnetic fabric of rocks, *Tectonophysics*, *79*(3-4), T63–T67, 1981.

Jezek, J., and S. Gilder, Competition of magnetic and hydrodynamic forces on ellipsoidal particles under shear: Influence of the Earth's magnetic field on particle alignment in viscous media, *Journal of Geophysical Research*, *111*(B12), 1–18, doi: 10.1029/2006JB004541, 2006.

Jones, C. H., User-driven integrated software lives: 'paleomag' paleomagnetics analysis on the Macintosh, *Computers & Geosciences*, *28*(10), 1145–1151, 2002.

Kelso, P., and S. Banerjee, Elevated temperature viscous remanent magnetization of natural and synthetic multidomain magnetite, *Earth and planetary science letters*, *122*(1-2), 43–56, doi: 10.1016/0012-821X(94)90050-7, 1994.

Keshtkar, A., A. Maghoul, and A. Kalantarnia, Magnetic Shield Effectiveness in Low Frequency, *International Journal of Computer and Electrical Engineering*, *3*(4), 507–513, 2011.

King, J., S. Banerjee, J. Marvin, and O. Özdemir, A comparison of different magnetic methods for determining the relative grain size of magnetite in natural materials: some results from lake sediments, *Earth and Planetary Science Letters*, *59*(2), 404–419, 1982.

King, J., S. Banerjee, and J. Marvin, A new rock-magnetic approach to selecting sediments for geomagnetic paleointensity studies: application to paleointensity for the last 4000 years, *Journal of Geophysical Research*, *88*(B7), 5911–5921, 1983.

Kirschvink, J., The least-squares line and plane and the analysis of palaeomagnetic data, *Geophysical Journal of the Royal Astronomical Society*, *62*(3), 699–718, 1980.

Kirschvink, J., R. Kopp, T. Raub, C. Baumgartner, and J. Holt, Rapid, precise, and high-sensitivity acquisition of paleomagnetic and rock-magnetic data: Development of a low-noise automatic sample changing system for superconducting rock magnetometers, *Geochemistry Geophysics Geosystems*, *9*(5), Q05Y01, doi: 10.1029/2007GC001856, 2008.

Kobayashi, A., J. Kirschvink, and M. Nesson, Ferromagnetism and EMFs., *Nature*, *374*(6518), 123, doi: 10.1038/374123a0, 1995.

Kodama, K. P., and M. J. Dekkers, Magnetic anisotropy as an aid to identifying CRM and DRM in red sedimentary rocks, *Studia Geophysica et Geodaetica*, *48*(4), 747–766, 2004.

Koroglu, S., N. Umurkan, O. Kilic, and F. Attar, An approach to the calculation of multilayer magnetic shielding using artificial neural network, *Simulation Modelling Practice and Theory*, *17*(7), 1267–1275, doi: 10.1016/j.simpat.2009.05.001, 2009.

Krilov, A., Absolute age of the rocks of the central Tien Shan and application of Argon methods to metamorphic and sedimentary sediments, in *Determination of the Absolute Age of Pre-Quaternary Formations*, edited by I. Starik, pp. 222–224, Nedra, Moscow, 1960.

Leonhardt, R., Analyzing rock magnetic measurements: The RockMagAnalyzer 1.0 software, *Computers & Geosciences*, *32*(9), 1420–1431, doi: 10.1016/j.cageo.2006.01.006, 2006.

Levi, S., and R. Merrill, A comparison of ARM and TRM in magnetite, *Earth and Planetary Science Letters*, *32*(2), 171–184, 1976.

Li, C., Z. Guo, and G. Dupont-Nivet, Late Cenozoic tectonic deformation across the northern foreland of the Chinese Tian Shan, *Journal of Asian Earth Sciences*, *42*(5), 1066–1073, doi: 10.1016/j.jseaes.2010.08.009, 2011.

Macaulay, E., E. Sobel, A. Mikolaichuk, B. Kohn, and F. Stuart, Linking exhumation and deformation in the Eastern Teresky Range in the Kyrgyz Tien Shan, in *Eos, Transactions American Geophysical Union*, AGU, San Francisco, 2011.

Martin-Hernández, F., C. M. Luneburg, C. Aubourg, and M. Jackson, Magnetic fabric: methods and applications – an introduction, *Geological Society, London, Special Publications*, *238*(1), 1–7, doi: 10.1144/GSL.SP.2004.238.01.01, 2004.

McCabe, C., M. Jackson, and B. Ellwood, Magnetic anisotropy in the Trenton limestone: results of a new technique, anisotropy of anhysteretic susceptibility, *Geophysical Research Letters*, *12*(6), 333–336, 1985.

McElhinny, M. W., and P. McFadden, *Paleomagnetism: Continents and Oceans*, 386 pp., Academic Press, San Diego, CA, 2000.

Mikolaichuk, A. V., S. A. Kurenkov, K. E. Degtyarev, and V. I. Rubtsov, Norther Tien Shan: Main Stages of Geodynamic Evolution in the Late Precambrian-Early Paleozoic, *Geotektonika*, *6*, 1997.

Molnar, P., and P. Tapponnier, Cenozoic Tectonics of Asia: Effects of a Continental Collision: Features of recent continental tectonics in Asia can be interpreted as results of the India-Eurasia collision., *Science*, *189*(4201), 419–426, doi: 10.1126/science.189.4201.419, 1975.

Moon, T., and R. Merrill, A new mechanism for stable viscous remanent magnetization and overprinting, *Geophysical Research Letters*, *13*(8), 737, doi: 10.1029/GL013i008p00737, 1986.

Morris, E. R., W. Schillinger, R. S. Coe, C. J. Pluhar, and N. A. Jarboe, Automating the 2G superconducting rock magnetometer for single-solenoid alternating field demagnetization, *Geochemistry Geophysics Geosystems*, *10*(5), Q05Y05, doi: 10.1029/2008GC002289, 2009.

Moskowitz, B., Theoretical grain size limits for single-domain, pseudo-single-domain and multi-domain behavior in titanomagnetite (x= 0.6) as a function of low-temperature oxidation, *Earth and Planetary Science Letters*, *47*(2), 285–293, 1980.

Moskowitz, B., Magnetic viscosity, diffusion after-effect, and disaccommodation in natural and synthetic samples, *Geophysical Journal International*, *82*(2), 143–161, doi: 10.1111/j.1365-246X.1985.tb05133.x, 1985.

Muxworthy, A. R., and W. Williams, Observations of viscous magnetization in multidomain magnetite, *Journal of Geophysical Research*, *111*(B1), 1–13, doi: 10.1029/2005JB003902, 2006.

Nakamura, N., Strain, anisotropy of anhysteretic remanence, and anisotropy of magnetic susceptibility in a slaty tuff, *Physics of The Earth and Planetary Interiors*, *125*(1-4), 85–93, doi: 10.1016/S0031-9201(01)00214-X, 2001.

Néel, L., Some theoretical aspects of rock-magnetism, *Advances in Physics*, *4*(14), 191–243, doi: 10.1080/00018735500101204, 1955.

Nørgaard Madsen, K., Angular dependence of the switching field and implications for gyromagnetic remanent magnetization in three-axis alternating-field demagnetization, *Geophysical Journal International*, *157*(3), 1007–1016, doi: 10.1111/j.1365-246X.2004.02228.x, 2004.

Okazaki, Y., and K. Ueno, Magnetic shielding by soft magnetic materials in alternating magnetic field, *Journal of Magnetism and Magnetic Materials*, *112*(750), 192–194, 1992.

Owens, W. H., Statistical applications to second-rank tensors in magnetic fabric analysis, *Geophysical Journal International*, *142*(2), 527–538, doi: 10.1046/j.1365-246x.2000.00174.x, 2000.

Patriat, P., and J. Achache, India–Eurasia collision chronology has implications for crustal shortening and driving mechanism of plates, *Nature*, *311*(18), 615–621, doi: 10.1038/311615a0, 1984.

Patton, B. J., and J. L. Fitch, Anhysteretic remanent magnetization in small steady fields, *Journal of Geophysical Research*, *67*(1), 307–311, 1962.

Potter, D. K., and A. Stephenson, Single-domain particles in rocks and magnetic fabric analysis, *Geophysical Research Letters*, *15*(10), 1097–1100, 1988.

Reigber, C., et al., New space geodetic constraints on the distribution of deformation in Central Asia, *Earth and Planetary Science Letters*, *191*(1-2), 157–165, doi: 10.1016/S0012-821X(01)00414-9, 2001.

Rikitake, T., *Magnetic and electromagnetic shielding*, Terra Scientific Publ., Tokyo, 1987.

Sasada, I., and Y. Nakashima, A new method of magnetic shielding: Combination of flux repulsion and backing up magnetic pathways, *Journal of Applied Physics*, *103*(7), 07E932, doi: 10.1063/1.2839586, 2008.

Sasada, I., S. Kubo, R. OHandley, and K. Harada, Low-frequency characteristic of the enhanced incremental permeability by magnetic shaking, *Journal of Applied Physics*, *67*(9), 5583–5585, doi: 10.1063/1.345891, 1990.

Sasada, I., T. Yamamoto, T. Yamauchi, and I. Introduction, Large shielding factor obtained by a multiple-shell magnetic shield having separate magnetic shaking, *Journal of Applied Physics*, *79*(8), 5490–5492, 1996.

Sasada, I., E. Paperno, and H. Koide, Design of a large-scale vertical open-structure cylindrical shield employing magnetic shaking, *Journal of Applied Physics*, *87*(9), 5962, doi: 10.1063/1.372580, 2000.

Scott, G. R., and C. Frohlich, Large-volume magnetically shielded room A new design and material, in *Magnetite biomineralization and magnetorezeption in organisms.*, vol. m, edited by J. et al. Kirschvink, pp. 197–220, Plenum Press, New York, 1985.

Shaw, J., J. Share, and J. Rogers, An automated superconducting magnetometer and demagnetizing system, *Geophysical Journal of the Royal Astronomical Society*, *78*(1), 209–217, 1984.

Si, J., and R. Voo, Too-low magnetic inclinations in central Asia: an indication of a long-term Tertiary non-dipole field?, *Terra Nova*, *13*(6), 471–478, 2001.

Sidorenko, A. V. (Ed.), *Geology of the USSR*, 280pp pp., Nedra Publications, Moscow, 1972.

Smart, J., R. Roebling, V. Zeitlin, and R. Dunn, wxWidgets 2.8.11: a portable C++ and Python GUI toolkit, 2010.

Sobel, E., J. Chen, and R. Heermance, Late Oligocene–Early Miocene initiation of shortening in the Southwestern Chinese Tian Shan: Implications for Neogene shortening rate variations, *Earth and Planetary Science Letters*, *247*(1-2), 70–81, doi: 10.1016/j.epsl.2006.03.048, 2006a.

Sobel, E., M. Oskin, D. Burbank, and A. V. Mikolaichuk, Exhumation of basement-cored uplifts: Example of the Kyrgyz Range quantified with apatite fission track thermochronology, *Tectonics*, *25*(2), doi: 10.1029/2005TC001809, 2006b.

Stacey, F., The physical theory of rock magnetism, *Advances in Physics*, *12*(45), 45–133, 1963.

Stephenson, A., Gyromagnetism and the remanence acquired by a rotating rock in an alternating field, *Nature*, *284*, 48–49, doi: 10.1038/284048a0, 1980.

Stephenson, A., S. Sadikun, and D. K. Potter, A theoretical and experimental comparison of the anisotropies of magnetic-susceptibility and remanence in rocks and minerals, *Geophysical J. Royal Astronomical Soc.*, *84*(1), 185–200, 1986.

Street, R., and J. C. Woolley, A Study of Magnetic Viscosity, *Proceedings of the Physical Society. Section A*, *62*(9), 562–572, doi: 10.1088/0370-1298/62/9/303, 1949.

Sun, J., and Z. Zhang, Syntectonic growth strata and implications for late Cenozoic tectonic uplift in the northern Tian Shan, China, *Tectonophysics*, *463*(1-4), 60–68, doi: 10.1016/j.tecto.2008.09.008, 2009.

Sun, J., R. Zhu, and J. Bowler, Timing of the Tianshan Mountains uplift constrained by magnetostratigraphic analysis of molasse deposits, *Earth and Planetary Science Letters*, *219*(3-4), 239–253, doi: 10.1016/S0012-821X(04)00008-1, 2004.

Sun, J., Y. Li, Z. Zhang, and B. Fu, Magnetostratigraphic data on Neogene growth folding in the foreland basin of the southern Tianshan Mountains, *Geology*, *37*(11), 1051–1054, doi: 10.1130/G30278A.1, 2009.

Suppe, J., G. Chou, and S. Hook, Rates of folding and faulting determined from growth strata, in *Thrust tectonics*, edited by K. R. McClay, pp. 105–121, Chapman and Hall, London, 1992.

Sycheva, N. A., S. L. Yunga, L. Bogomolov, and V. I. Makarov, Seismotectonic deformations and recent tectonics of the Tien Shan, *Izvestiya Physics of the Solid Earth*, *44*(5), 351–363, doi: 10.1134/S1069351308050017, 2008.

Tan, X., K. P. Kodama, H. L. Chen, D. Fang, D. Sun, and Y. Li, Paleomagnetism and magnetic anisotropy of Cretaceous red beds from the Tarim basin, northwest China: Evidence for a rock magnetic cause of anomalously shallow paleomagnetic inclinations from central Asia, *J. Geophysical Research-solid Earth*, *108*(B2), 2107, 2003.

Tapponnier, P., and P. Molnar, Active faulting and Cenozoic tectonics of the Tien Shan, Mongolia, and Baykal regions, *Journal of Geophysical Research*, *84*(B7), 3425–3459, doi: 10.1029/JB084iB07p03425, 1979.

Tarling, D., and F. Hrouda, *The Magnetic Anisotropy of Rocks*, first ed., 217 pp., Chapman and Hall, London, 1993.

Thomas, J., H. Perroud, P. R. Cobbold, M. L. Bazhenov, V. S. Burtman, A. Chauvin, and E. Sadybakasov, A paleomagnetic study of Tertiary formations from the Kyrgyz Tien-Shan and its tectonic implications, *Journal of Geophysical Research*, *98*(B6), 9571–9589, doi: 10.1029/92JB02912, 1993.

Thompson, S., R. Weldon, C. Rubin, K. Abdrakhmatov, P. Molnar, and
    G. Berger, Late Quaternary slip rates across the central Tien Shan, Kyrgyzs-
    tan, central Asia, *J. Geophys.*, *107*(B9), doi: 10.1029/2001JB000596, 2002.

Urrutia-Fucugauchi, J., Some observations on short-term magnetic behaviour at
    room temperture, *Physics of the Earth and Planetary Interiors*, *26*, P1–P5,
    1981.

Van Houten, F. B., Origin of red beds. A review 1961-1972, *Annual Review
    Earth Planetary Science*, *1*, 39–61, 1973.

van Rossum, G., and F. Drake, *The Python Language Reference Manual*, 286
    pp., CreateSpace, Paramount, CA, 2009.

Wack, M., A new software for the measurement of magnetic moments using
    SQUID and spinner magnetometers, *Computers & Geosciences*, *36*(9), 1178–
    1184, doi: 10.1016/j.cageo.2010.05.002, 2010.

Wack, M. R., and S. A. Gilder, The SushiBar: An automated system for
    paleomagnetic investigations, *Geochem. Geophys. Geosyst.*, *in press*, doi:
    10.1029/2011GC003985, 2012.

Watson, G., and R. Enkin, The fold test in paleomagnetism as a parameter
    estimation problem, *Geophysical Research Letters*, *20*(19), 2135–2137, doi:
    10.1029/93GL01901, 1993.

Widenius, M., D. Axmark, and K. Arno, *MySQL Reference Manual*, 816 pp.,
    O'Reilly Media, 2002.

Winkler, A., and L. Sagnotti, Anisotropies of anhysteretic remanence and mag-
    netic susceptibility of marly clays from Central Italy, *Annals of Geophysics*,
    37(5), 1027–1035, 1994.

Winkler, A., L. Alfonsi, F. Florindo, L. Sagnotti, and F. Speranza, The magnetic
    anisotropy of rocks: principles, techniques and geodynamic applications in the
    Italian peninsula, *Annals of Geophysics*, *40*(3), 729–740, 1997.

Xuan, C., and J. Channell, UPmag: MATLAB software for viewing and pro-
    cessing u channel or other pass-through paleomagnetic data, *Geochemistry
    Geophysics Geosystems*, *10*(10), doi: 10.1029/2009GC002584, 2009.

Yan, M., R. Voo, and L. Tauxe, Shallow bias in Neogene palaeomagnetic direc-
    tions from the Guide Basin, NE Tibet, caused by inclination error, *Geophysi-
    cal Journal*, *163*(3), 944–948, 2005.

Yu, Y., and L. Tauxe, Acquisition of viscous remanent magnetization, *Physics of The Earth and Planetary Interiors*, *159*(1-2), 32–42, doi: 10.1016/j.pepi.2006.05.002, 2006.

Yu, Y., D. Dunlop, and O. Özdemir, Partial anhysteretic remanent magnetization in magnetite 1. Additivity, *Journal of Geophysical Research*, *107*(B10), doi: 10.1029/2001JB001249, 2002.

Zijderveld, J. D. A., A. C. demagnetization of rocks: Analysis of results, in *Methods in Palaeomagnetism*, edited by D. W. Collinson, K. M. Creer, and S. K. Runcorn, pp. 254–286, Elsevier, Amsterdam, 1967.

Zubovich, A. V., et al., GPS velocity field for the Tien Shan and surrounding regions, *Tectonics*, *29*(6), 1–23, doi: 10.1029/2010TC002772, 2010.

B. CryoMag Example Files

B.1. CryoMag Data File *.cmag.xml

Listing B.1: CryoMag data file

```
1  <?xml version="1.0" encoding="UTF-8" ?>
2  <?xml-stylesheet type="text/xsl" href="cryomag.xsl" ?>
3  <!DOCTYPE cryomagdata>
4  <cryomagdata version='1.5'><!-- This file was written by CryoMag 1.5 on 08-09-02 12
       :34:36. -->
5    <specimen bedaz='290.0' beddip='12.0' coreaz='132.0' coredip='45.0' name='1001A' vol=
         '1.100E+001' weight='4.300E+001'>
6      <step comment='' instr='CryoNL1' step='0' type='TH'>
7        <holder D='279.5' I='-11.1' M='2.821E-012' X='4.565E-013' Y='-2.731E-012' Z='
             -5.438E-013' a95='3.66' sM='1.233E-012' time='08-07-04 10:16:38' />
8        <measurements>
9          <magmoment D='224.5' I='-25.0' M='1.961E-010' X='-1.267E-010' Y='-1.247E-010' Z
               ='-8.291E-011' a95='0.04' no_readings="3" sM='1.024E-012' time='08-07-04
               10:34:47' type='baseline' />
10         <magmoment D='353.1' I='76.8' M='2.824E-009' X='6.402E-010' Y='-7.748E-011' Z='
               2.750E-009' a95='0.01' no_readings="3" sM='4.913E-013' time='08-07-04 10
               :34:54' type='Pos 1 (0, 0, 0)' />
11         <magmoment D='343.8' I='73.6' M='2.823E-009' X='7.654E-010' Y='-2.219E-010' Z='
               2.708E-009' a95='0.00' no_readings="3" sM='5.765E-013' time='08-07-04 10
               :35:18' type='Pos 2 (0, 180, 90)' />
12         <magmoment D='224.6' I='-24.9' M='1.962E-010' X='-1.267E-010' Y='-1.249E-010' Z
               ='-8.270E-011' a95='0.11' no_readings="3" sM='1.336E-012' time='08-07-04
               10:35:27' type='baseline' />
13       </measurements>
14       <results D='348.0' I='75.2' M='2.822E-009' X='7.028E-010' Y='-1.497E-010' Z='
             2.729E-009' a95='0.46' sM='1.057E-012' time='08-07-04 10:35:29' />
15     </step>
16      ...
17
18    </specimen>
19  </cryomagdata>
```

C. Program Listings

C.1. Calculation of anisotropy tensors

Listing C.1: Python script for calculation of anisotropy tensors

```python
import numpy
from math import sin, cos, radians, degrees, atan2, asin, exp, log, sqrt, atan

# create design matrix for anisotropy measurements
# input
# mdirs: measurement directions e.g. [[D1,I1],[D2,I2],[D3,I3],[D4,I4]]
# xyz: True --> individual components measured (AARM); False: one component measured (
    AMS) or ARM without GRM

def makeDesignMatrix( mdirs, xyz):
    # directions in cartesian coordinates
    XYZ = []
    for i in range( len( mdirs)):
        XYZ.append([cos( radians( mdirs[i][0]))*cos( radians( mdirs[i][1])), sin(
            radians( mdirs[i][0]))*cos( radians( mdirs[i][1])), sin( radians( mdirs[i
            ][1]))])


    # make design matrix for single components (x,y,z)
    B = numpy.zeros((len( XYZ) * 3,6),'f')

    for i in range( len( XYZ)):
        B[i*3+0][0] = XYZ[i][0]
        B[i*3+0][3] = XYZ[i][1]
        B[i*3+0][5] = XYZ[i][2]

        B[i*3+1][3] = XYZ[i][0]
        B[i*3+1][1] = XYZ[i][1]
        B[i*3+1][4] = XYZ[i][2]

        B[i*3+2][5] = XYZ[i][0]
        B[i*3+2][4] = XYZ[i][1]
        B[i*3+2][2] = XYZ[i][2]

    if xyz == True:
        A = B

    else:
```

```
37         # make design matrix for directional measurement (same direction as applied
               field)
38         A=numpy.zeros((len( mdirs),6),'f')
39
40
41         for i in range( len( XYZ)):
42             A[i] = XYZ[i][0]*B[i*3+0] + XYZ[i][1]*B[i*3+1] + XYZ[i][2]*B[i*3+2]
43
44     return A
45
46
47 # calculate pseude inverse of matrix A
48 def CalcPseudoInverse( A):
49     AT=numpy.transpose(A)
50     ATA=numpy.dot(AT,A)
51     ATAI=numpy.linalg.inv(ATA)
52     B=numpy.dot(ATAI,AT)
53
54     return B
55
56
57 # calculate eigenvalues and eigenvectors from tensor T, sorted by eigenvalues
58 def CalcEigenValVec( T):
59     #get eigenvalues and eigenvectors
60     eigvals, eigvec = numpy.linalg.eig( T)
61
62     # sort by eigenvalues
63     # put eigenvalues and and eigenvectors together in one list and sort this one
64     valvec = []
65     for i in range( len( eigvals)):
66         valvec.append( [ eigvals[i], numpy.transpose( eigvec)[i].tolist()])
67
68     # sort eigenvalues and eigenvectors by eigenvalues
69     valvec.sort( lambda x, y: -cmp( x[0], y[0])) # sort from large to small
70
71     for i in range( len(valvec)):
72         eigvals[i] = valvec[i][0]
73         eigvec[i] = valvec[i][1]
74
75     return eigvals, eigvec
76
77
78 def CalcAnisoTensor( A, K):
79     ''' calculate anisotropy tensor
80         input: A: design matrix
81                K: measured values
82         return: dictionary
83                R: anisotropy tensor
84                eigvals: eigenvalues as array
85                n_eigvals: normalized eigenvalues as array
86                n_eval1, n_eval2, n_eval3: normalized eigenvalues
87                eigvecs: eigenvectors (sorted by eigenvalues)
88                I1, I2, I3, D1, D2, D3: inclinations and declinations of eigenvectors
89                M: mean magnetization
90                L: lineation
91                F: foliation
92                P: degree of anisotropy
93                P1: corrected degree of anisotropy
94                T:
95                U:
96                Q:
97                E:
```

```
 98                     S0: sum of error^2
 99                     stddev: standard deviation
100                     E12: 12 axis of confidence ellipse
101                     E23: 23 axis of confidence ellipse
102                     E13: 13 axis of confidence ellipes
103                     F0: test for anisotropy (Hext 63)
104                     F12: test for anisotropy
105                     F23: test for anisotropy
106                     QF: quality factor
107                     '''
108
109         aniso_dict = {}
110         aniso_dict['msg'] = '' # put in here any message you want to pass out of this
                routine
111
112         # calculate pseudo inverse of A
113         B = CalcPseudoInverse( A)
114         # calculate elements of anisotropy tensor
115         s = numpy.dot( B, K)
116         # construct symmetric anisotropy tensor R (3x3)
117         R = numpy.array([[s[0],s[3],s[5]],[s[3],s[1],s[4]],[s[5],s[4],s[2]]])
118         aniso_dict['R'] = R
119         # calculate eigenvalues and eigenvectors = principal axes
120         eigvals, eigvecs = CalcEigenValVec( R)
121         aniso_dict['eigvals'] = eigvals
122         aniso_dict['eigvecs'] = eigvecs
123
124         # calc inclination and declination of eigenvectors
125         (D1, I1, L) = XYZ2DIL( eigvecs[0])
126         (D2, I2, L) = XYZ2DIL( eigvecs[1])
127         (D3, I3, L) = XYZ2DIL( eigvecs[2])
128
129         # to get consistent plotting, make all inclinations negative
130         aniso_dict['D1'], aniso_dict['I1'] = MirrorDirectionToNegativeInclination( D1, I1)
131         aniso_dict['D2'], aniso_dict['I2'] = MirrorDirectionToNegativeInclination( D2, I2)
132         aniso_dict['D3'], aniso_dict['I3'] = MirrorDirectionToNegativeInclination( D3, I3)
133
134
135         #calc mean magnetization
136         M = (eigvals[0]+eigvals[1]+eigvals[2])/3
137         aniso_dict['M'] = M
138
139         #calc normalized eigenvalues k
140         k = eigvals / (eigvals[0]+eigvals[1]+eigvals[2])*3
141         aniso_dict['n_eigvals'] = k
142         aniso_dict['n_eval1'] = k[0]
143         aniso_dict['n_eval2'] = k[1]
144         aniso_dict['n_eval3'] = k[2]
145
146         #calc some parameters
147         L = k[0] / k[1]
148         F = k[1] / k[2]
149         P = k[0] / k[2]
150
151         aniso_dict['L'] = L
152         aniso_dict['F'] = F
153         aniso_dict['P'] = P
154
155         n = []
156         neg_eigenvalue = False # check for negative eigenvalues, log will fail
157         for kn in k:
158             if kn <=0:
```

```python
159                  neg_eigenvalue = True
160                  aniso_dict['msg'] = 'Warning: negative eigenvalue!'
161                  n.append( None)
162              else:
163                  n.append( log( kn))
164
165      if not neg_eigenvalue:
166          navg = (n[0]+n[1]+n[2]) / 3
167
168          P1 = exp( sqrt( 2 * ((n[0]-navg)**2+(n[1]-navg)**2+(n[2]-navg)**2)))
169          aniso_dict['P1'] = P1
170
171          T = (2 * n[1] - n[0] - n[2]) / (n[0] - n[2])
172          aniso_dict['T'] = T
173
174      else:
175          aniso_dict['P1'] = 0 # not possible to calc -> set to 0
176          aniso_dict['T'] = 0
177
178      U = (2 * k[1] - k[0] - k[2]) / (k[0] - k[2])
179      aniso_dict['U'] = U
180
181      Q = (k[0]-k[1]) / ((k[0]+k[1])/2-k[2])
182      aniso_dict['Q'] = Q
183
184      E = k[1]**2 / (k[0] * k[2])
185      aniso_dict['E'] = E
186
187
188      #calculate best fit values of K
189      Kf = numpy.dot( A, s)
190
191      #calculate K - Kf --> errors
192      d = K - Kf
193
194      #calculate sum of errors^2
195      S0 = numpy.dot( d, d)
196      aniso_dict['S0'] = S0
197
198      #calculate variance
199      var = S0 / (len(d)/3)
200      # len(d) == 18 for 6 directions (12 measured)
201      # calc standard deviation
202      stddev = sqrt( var)
203      aniso_dict['stddev'] = stddev
204
205      # calculate quality factor
206      QF = (P-1) / (stddev / M)
207      aniso_dict['QF'] = QF
208
209      # calculate confidence ellipses
210      #F = 3.89 --> looked up from tauxe lecture 2005; F-table
211      f = sqrt( 2 * 3.89)
212      E12 = abs( degrees( atan( f * stddev / (2 * (eigvals[1]-eigvals[0])))))
213      E23 = abs( degrees( atan( f * stddev / (2 * (eigvals[1]-eigvals[2])))))
214      E13 = abs( degrees( atan( f * stddev / (2 * (eigvals[2]-eigvals[0])))))
215
216      aniso_dict['E12'] = E12
217      aniso_dict['E23'] = E23
218      aniso_dict['E13'] = E13
219
220      #Tests for anisotropy (Hext 63)
```

```
221     F0 = 0.4 * ( eigvals[0]**2+eigvals[1]**2+eigvals[2]**2 - 3 * ((s[0]+s[1]+s[2])/3)
            **2 ) / var
222     F12 = 0.5 * ((eigvals[0] - eigvals[1]) / stddev)**2
223     F23 = 0.5 * ((eigvals[1] - eigvals[2]) / stddev)**2
224
225     aniso_dict['F0'] = F0
226     aniso_dict['F12'] = F12
227     aniso_dict['F23'] = F23
228
229
230     return aniso_dict # return the whole bunch of values
```